SOLAR THERMIONIC FLIGHT

EXPERIMENT STUDY

FINAL REPORT

Volume IV - APPENDICES

PREPARED UNDER

CONTRACT NO. 950552

FOR

JET PROPULSION LABORATORY
CALIFORNIA INSTITUTE OF TECHNOLOGY
4800 OAK GROVE DRIVE
PASADENA, CALIFORNIA 91103

GENERAL ⊛ ELECTRIC

SPACECRAFT DEPARTMENT

1/ii

131

APPENDICES

TABLE OF CONTENTS

APPENDICES

TABLE OF CONTENTS (Cont'd)

RE-ORDER NO.

APPENDICES

TABLE OF CONTENTS (Cont'd)

Appendix Page

P. EVALUATION OF GENERATOR MISALIGNMENT AND ORIENTATION ERROR SENSING METHODS FOR SOLAR THERMIONIC SYSTEMS . . P-1
1. Introduction P-1
2. Nomenclature P-3
3. Summary and Results P-5
4. Solar Concentrator Performance P-9
5. Orientation Sensor Performance P-17
6. References P-42

LIST OF ILLUSTRATIONS

LIST OF ILLUSTRATIONS (Cont'd)

APPENDIX A

CALCULATION OF HEAT TRANSFER
AND VOLTAGE DROP IN
THERMIONIC CONVERTER SLEEVE

APPENDIX A

CALCULATION OF HEAT TRANSFER AND VOLTAGE DROP IN THERMIONIC CONVERTER SLEEVE

1. INTRODUCTION

This appendix outlines the procedure used for calculating the heat transfer and voltage drop in the thermionic converter sleeve. The calculation used as a sample is for the JPL series VIII converter with a 0.0025 inch tantalum sleeve.

2. NOMENCLATURE

The nomenclature employed in the analysis is outlined below.

A	Area presented to the heat transfer in various elements
dq_1, dq_2	Differential quantities of heat lost by radiation to the collector and to the outer environment, respectively
dx	Differential element of sleeve
D	Inside diameter of sleeve
q_1	Heat from the emitter structure into sleeve
q_n	Heat transferred by conduction from the (n-1)th sleeve element into the nth element
q_L	Heat transferred by the sleeve into the seal assembly
q_x	Heat transfer in the sleeve at distance x from the emitter structure
R, R_A, R_B $R_{ceramic}$	Thermal resistances of corresponding element in the seal assembly

t	Thickness of sleeve wall
$T_1, T_1',$ T_1''	Temperature, first and second derivatives with respect to x for the first sleeve element in finite differential calculations of sleeve temperature distribution
T_A, T_B	The temperatures of seal flanges at the points of attachment to the insulating ceramic
T_F	Temperature at point of attachment of the seal assembly to the collector structure
T_L	Temperature of the sleeve at point of attachment to the seal assembly
$T_n, T_n',$ T_n''	Temperature, first and second derivatives with respect to x for the first sleeve element
T_x	Sleeve temperature at distance x from the emitter structure
δ	Radial thickness of the collector between the emitter and the emitter support
σ	Stefan-Boltzmann constant -- 0.1714×10^{-8} Btu/hr-ft^2-$^\circ$R^4.

3. ANALYSIS

Figure A-1 shows the basic geometry of the lead. A molybdenum shield at 900°K on both sides of the sleeve is assumed.

Figure A-2 shows the heat transfer conditions for an element of the tantalum sleeve. For this geometry

$$dq_1 = (\pi D\, dx)\, \sigma\, (T_x^4 - 900^4) \left[\frac{1}{\epsilon_{Ta}} + \frac{1}{\epsilon_{Mo}} - 1 \right]^{-1} \tag{1}$$

$$dq_2 = \pi (D + 2t)\, dx\, \sigma\, (T_x^4 - 900^4) \left[\frac{1}{\epsilon_{Ta}} + \frac{1}{\epsilon_{Mo}} - 1 \right]^{-1} \tag{2}$$

A-2

$$\dot{q}_x \quad -k_{Ta} \, \pi \, (D + t) \, t \left(\frac{dT}{dx}\right)_x \tag{3}$$

and

$$\dot{q}_{x+1} \quad -k_{Ta} \, \pi \, (D + t) \, t \left[\left(\frac{dT}{dx}\right)_x + \left(\frac{d^2T}{dx^2}\right) dx\right] . \tag{4}$$

Equations 1, 2, 3 and 4 may be combined by subtracting Equation 4 from 3:

$$k_{Ta} \, \pi \, (D + t) \, t \left(\frac{d^2T}{dx^2}\right) = \pi \, \sigma \, (T_x^4 - 900^4) \left[\frac{1}{\epsilon_{Ta}} + \frac{1}{\epsilon_{Mo}} - 1\right]^{-1} (D \cdot D \cdot 2t).$$

Which simplifies to:

$$\frac{d^2T}{dx^2} = \frac{2 \, \sigma \, (T_x^4 - 900^4)}{K_{Ta} t} \left[\frac{1}{\epsilon_{Ta}} + \frac{1}{\epsilon_{Mo}} - 1\right]^{-1} . \tag{5}$$

Calculation Procedure:

1. Divide sleeve in elements of length δ and assume a value of $\dot{q}_1$ which (from Equation 3) corresponds to a value of $\dot{T}_1'$.

2. Calculate T_1: $T_1 = T_0 + \frac{\delta}{2} T_1'$

3. Use Equation 5 to calculate T_1'' .

4. Calculate T_2': $T_2' = T_1' + \delta \, T_1''$

5. Repeat for successive elements until $x = L$ and values of q_L and T_L have been found.

6. Check whether boundary condition at $x = L$ is satisfied.

Boundary Condition at x = L:

Figure A-3 shows the remainder of the diode structure that connects the point at $x = L$ to the collector at point F where the temperature is T_F.

A-3

Figure A-1.   Basic Lead Geometry

Figure A-2.   Element of Tantalum Sleeve

Figure A-3.   Thermal Resistance Path

A-4

The value of T_F is determined by the collector temperature and the temperature drop in the collector structure. In this particular analysis, a typical value of $847^O K$ was used for all the lead heat transfer calculations.

Now let R be the thermal resistance of the path from L to F shown in Figure A-3, the heat transfer q_L and temperature T_L are related by the expression:

$$\frac{T_L - T_F}{q_L} = R = R_1 + R_{ceramic} + R_2. \tag{6}$$

Generally $\quad R = \dfrac{L}{kA}$

$$R_1 = \frac{0.080 \times 2.54}{0.536\left[\pi \times 0.740 \times 0.015\right] \times 2.54 \times 2.54} = 1.68^O\ C/watt$$

$$R_2 = \frac{0.80}{0.536\left[\pi \times 0.730 \times 0.015\right] \times 2.54} = 3.78^O\ C/watt$$

$$R_{ceramic} = \frac{L}{kA_{effective}} = \frac{3L}{kA_{actual}} = \frac{0.180}{0.092\left[\pi \times 0.960 \times 0.140\right] \times 2.54}$$

$$= 1.82^O\ C/watt.$$

The 0.536 watt/cm - ^{O}C thermal conductivity value used for tantalum was obtained from the Handbook of Thermophysical Properties of Solid Materials, page 58-2, for a temperature of 600^OC. The thermal conductivity of the ceramic (0.092 watt/cm - ^{O}C) was obtained from High Temperature Technology, by Campbell.

The effective area of the ceramic is assumed equal to 1/3 of the actual area because of the two-dimensional character of the heat transfer distribution in the ceramic plane shown in Figure A-3. Equation 6 gives the relationship

$$T_L = 7.28\ q_L + 847^O K \tag{7}$$

which is the boundary condition that must be satisfied by the solution of Equation 5.

$$\delta = 0.100 \text{ cm}$$

$$k_{T_a} = 0.76 \text{ watts/cm-}^\circ\text{C} \quad \text{(value at } 1230^\circ\text{C)}$$

$$\epsilon_{Ta} = 0.200 \quad \text{(value at } 1400^\circ\text{C)}$$

$$\epsilon_{Mo} = 0.144 \quad \text{(value at } 1400^\circ\text{C)}$$

The k_{Ta} value was obtained from the Handbook of Thermophysical Properties of Solid Materials and the ϵ_{Ta} and ϵ_{Mo} emissivity values from Materials and Techniques For Electron Tubes, by W. Kohl.

Substituting these numerical values Equations 3 and 5 take the form:

$$q_n = -2.38 (D + t) t T_n' \quad \begin{cases} = -0.0601 \, T_n' \quad @ \, t = 0.01525 \\ = -0.0249 \, T_n' \quad @ \, t = 0.00635 \end{cases} \tag{8}$$

$$T_n'' = \frac{1.365}{t} \left[\left(\frac{T_n}{1000} \right)^4 - 0.658 \right] \tag{9}$$

In order to handle the change in wall thickness of the sleeve, an interface, I, must be used for calculations. The table for run No. 1 is self-explanatory.

$$\text{For: } t = 0.01525 \text{ cm} \qquad T_n'' = 89.5 \left[(0.001 \, T_n)^4 - 0.658 \right]$$

$$t = 0.00635 \text{ cm} \qquad T_n'' = 215.0 \left[(0.001 \, T_n)^4 - 0.658 \right]$$

The solution of the equation is then:

$$q_1 = 49 + \frac{-\Delta_3}{-\Delta_2 + \Delta_3} \times (50-49) = 49.34 \text{ watts}$$

$$q_L = 18.4 + \frac{\Delta_3}{\Delta_3 - \Delta_2} (19.9 - 18.4) = 18.91 \text{ watts}$$

$$T_L = 7.28 \times 18.91 + 847 = 985^\circ\text{K} \quad (= 712^\circ\text{C})$$

In the seal: (See Figure A-3)

$$T_1 = 985 - R_1 \times 18.91$$
$$= 985 - 1.68 \times 18.91 = 953^{\circ}K \ (= 680^{\circ}C)$$
$$(\Delta T_1 = -32^{\circ}C)$$

$$T_2 = 953 - R_{ceramic} \times 18.91$$
$$= 953 - 1.82 \times 18.91 = 918.6^{\circ}K \ (= 645.6^{\circ}C)$$
$$(\Delta T_{ceramic} = -34.4^{\circ}C)$$
$$(\Delta T_2 = -71.5^{\circ}C).$$

The heat that appears at the diode radiator is

$$q_{spacer\ to\ radiator} = 1891 + \frac{D}{D \pm (D+2t)} \left[49.34 - 18.91 \right]$$

where the second term corresponds to the heat transfer by radiation from the spacer to the collector (See Equation 1)

$$q_{spacer\ to\ radiator} = 18.91 + 15.18 = 34.09\ watts,$$

Voltage drop:

The resistance of the sleeve is calculated as follows:

$$R_L = R_{sleeve} + R_{Niobium\ flange}$$

$$R_{sleeve} = \frac{\rho_1 \ell_1}{s_1} + \frac{\rho_2 \ell_2}{s_2}$$

ρ_1 = Resistivity at $1900^{\circ}K = 75.8 \times 10^{-6}$ ohm-cm

ρ_2 = Resistivity at $1400^{\circ}K = 59 \times 10^{-6}$ ohm-cm

ℓ_1 = 0.200 cm $s_1 = 0.0785\ cm^2$

ℓ_2 = 0.900 cm $s_2 = 0.0327\ cm^2$

R_{sleeve} = (191 + 1.625) x 10-6 ohms

$\qquad\qquad$ = 1.816 x 10^{-3} ohms

$R_{Niobium\ flange}$ = $\rho\ \dfrac{\ell}{S}$

ρ $\qquad$ = Resistivity at $1000^{\circ}K$ = 44.2 x 10^{-6} ohm-cm

ℓ $\qquad$ = 0.220 in. = 0.560 cm

s $\qquad$ = $\left[\pi \times 0.740 \times 0.015\right]$ x 2.54 x 2.54 = 0.225 cm^2

$\qquad\qquad R_{Niobium\ flange}$ = 110 x 10^{-6} ohms

R_L $\quad$ = 1.93 x 10^{-3} ohms

ΔV_L = 1.93 millivolts/amp.

The resistivity values were obtained from page 340 of Materials and Techniques For Electron Tubes, by W. Kohl.

A-8

RUN NO. 1

Assumed Value of $q_1 = 60$ Watts

$$T_1' = \frac{-60}{2.38\,(1.640 + 0.015)\,(0.01525)} = -998^{\circ}\,C/cm$$

n	T_n' $^{\circ}C/cm$		T_n $^{\circ}K$	$\left(\dfrac{T_n}{1000}\right)^4$	$\left(\dfrac{T_n}{1000}\right)^4 - 0.658$	T_n'' $^{\circ}C/cm^2$
0	---		1981	---	---	---
1	-998	$\left(\dfrac{\delta}{2}\right)$	1931.1	13.95	13.29	1190
2	-879		1843.2	11.56	10.90	976
I	-781.4	$\left(\dfrac{\delta}{2}\right)$	1804.1	---	---	---
3	$\dfrac{t_2}{t_3}$ -1875	$\left(\dfrac{\delta}{2}\right)$	1710.1	8.58	7.92	1703
4	-1704.7		1539.9	5.62	4.96	1068
5	-1597.9		1380.1	3.64	2.98	641
6	-1533.8		1226.7	2.26	1.60	344
7	-1499.4		1076.8	1.34	0.68	146
8	-1484.8		928.3	0.741	0.083	18
9	-1483.0		780.0			
10						
11						
L		$\left(\dfrac{\delta}{2}\right)$				

89.5

215.0

Since T_9 is less than T_F, the value of q_1 assumed is too large.

RUN NO. 2

Assumed value of $q_1 = 50$ Watts

$$T_1' = \frac{-50}{0.0601} = -833^{\circ}\,C/cm$$

n	T_n' $^{\circ}C/cm$	T_n $^{\circ}K$	$\left(\dfrac{T_n}{1000}\right)^4$	$\left(\dfrac{T_n}{1000}\right)^4 - 0.658$	T_n'' $^{\circ}C/cm^2$
0	---	1981	---	---	---
1	-833.0	$\left(\frac{\delta}{2}\right)$ 1939.4	4.16	13.50	1209
2	-712.1	1868.2	12.19	11.53	1032
I	-608.9	$\left(\frac{\delta}{2}\right)$ 1837.8	---	---	---
3	-1464	$\left(\frac{\delta}{2}\right)$ 1764.6	9.69	9.03	1941
4	-1269.9	1637.6	7.19	6.53	1404
5	-1129.5	1524.7	5.40	4.74	1020
6	-1009.5	1423.7	4.12	3.46	745
7	-935.0	1330.2	3.14	2.48	533
8	-881.7	1242.0	2.38	1.72	370
9	-844.7	1157.5	1.80	1.14	245
10	-820.2	1075.5	1.34	0.68	146
11	-805.6	994.9	0.98	0.32	69
L	-798.7	$\left(\frac{\delta}{2}\right)$ 955.0			

Note: the $\left(\frac{t_2}{t_3}\right)$ bracket spans rows I through 3 in the T_n' column.

$$q_L = 798.7 \times 0.0269 = 19.9 \text{ watts}$$

Check boundary condition:
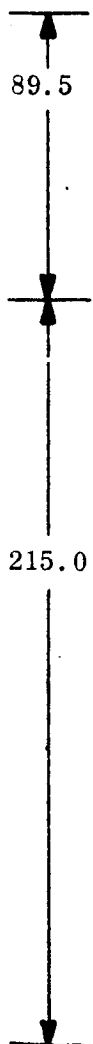
$$T_L = 7.28 \times 19.9 + 847 = 145 + 847 = 992^{\circ}K$$

$955^{\circ}K$ is too low, it indicates that the value of q_1 assumed was too large (compare with Run No. 1).

89.5

215.0

RUN NO. 3

Assumed Value of q_1: 49 Watts

$$T_1{}' = \frac{-49}{0.0601} = -816 \quad {}^{\circ}C/cm$$

n	T'_n $^{\circ}C/cm$		$T_n{}'$ $^{\circ}K$	$\left(\dfrac{T_n}{1000}\right)^4$	$\left(\dfrac{T_n}{1000}\right)^4 - 0.658$	T''_n $^{\circ}C/cm^2$
0	---		1981	- - -	- - -	- - -
1	-816.0	$(\frac{\delta}{2})$	1940.2	14.19	13.53	1211
2	-694.9		1870.7	12.22	11.56	1034
I	-591.5	$(\frac{\delta}{2})$	1841.1	.. - -	- - -	- - -
3	$(\frac{t_2}{t_3})$ -1422.0	$(\frac{\delta}{2})$	1770.0	9.81	9.15	1969
4	-1225.1		1647.5	7.38	6.72	1445
5	-1080.6		1539.4	5.61	4.95	1064
6	-974.2		1442.0	4.32	3.66	788
7	-895.4		1352.5	3.35	2.69	579
8	-837.5		1268.7	2.59	1.93	414
9	-796.1		1189.1	2.00	1.34	288
10	-767.3		1112.4	1.53	0.87	187
11	-748.6		1037.5	1.16	0.50	107
L	-737.9	$(\frac{\delta}{2})$	1000.6			

89.5

215.0

$q_1 = 737.9 \times 0.0249 = 18.4$ Watts

Check boundary conditions:

$$T_L = 7.28 \times 18.4 + 847 = 134 + 847 = 981 \,^{\circ}K$$

$1000.6\,^{\circ}K$ is too high. Therefore, solution lies between Runs No. 2 and No. 3. $\Delta_2 = -37\,^{\circ}K$ $\Delta_3 = +19\,^{\circ}K$
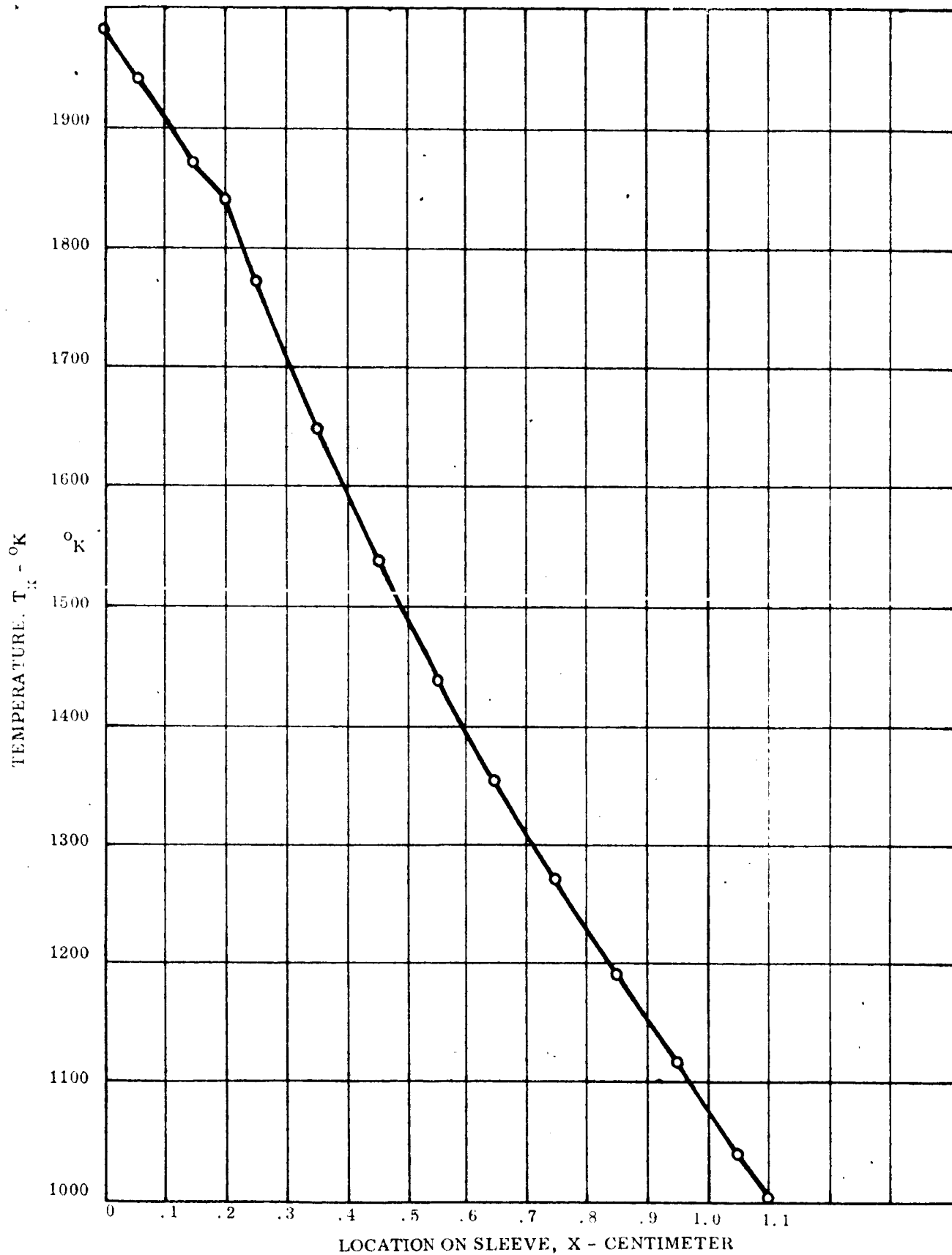
Figure A-4. Typical Temperature Distribution in Sleeve Run No. 3

APPENDIX B

CALCULATION OF CAVITY
ENERGY DISTRIBUTION

APPENDIX B

CALCULATION OF CAVITY ENERGY DISTRIBUTION

1. INTRODUCTION

This appendix summarizes the cavity energy distribution computations. The tabular results contained in this appendix are discussed and presented graphically in Section 8.4.1 (Volume III).

2. NOMENCLATURE

The symbols employed in this appendix are defined below:

E = Energy entering generator cavity, watts

D = Internal diameter of generator cavity, cm

D_a = Aperture diameter of generator cavity, cm

L = Length of generator cavity, cm

F_{ij} = Radiation view factor from surface i to surface j

S_i = Solar energy arriving at surface i, watts

α_i = Solar absorptivity of surface i

H_i = Thermal energy arriving at surface i, watts

ϵ_i = Thermal emissivity of surface i

T_i = Temperature of surface i, ^{o}K

Q_i = Net energy transferred to area element i, watts

σ = Stefan-Boltzmann constant, watts/cm^2-^{o}K^4.

3. CALCULATIONS

3.1 CALCULATION OF CAVITY SURFACE AREAS

Refer to Figure 8-7, Section 8.4.1 (Volume III).

$$A_1 = \pi \, DL + \frac{\pi \, D^2}{4}$$

$$D = 2.34 \text{ cm}$$

$$A_2 = \frac{\pi \, D_a^2}{4}$$

$$D_a = 1.8 \text{ cm}$$

$$A_3 = \frac{\pi \, D^2}{4} - \frac{\pi \, D_a^2}{4}$$

$$L = 2.16 \text{ cm}$$

3.2 CALCULATION OF VIEW FACTORS

$$F_{21} = 1.0$$

$$F_{31} = 1.0$$

$$F_{12} = F_{21} \times A_2/A_1 = 0.1261$$

$$F_{13} = F_{31} \times A_3/A_1 = 0.087$$

$$F_{11} = 1 - F_{13} - F_{12} = 1 - 0.2131 = 0.7869$$

The other view factors equal either 0 or 1.0.

3.3 HEAT BALANCE EQUATIONS

3.3.1 Solar Energy

The solar energy arriving at surfaces A_1, A_2 and A_3 is defined by the following expressions:

$$S_1 = E + (1-\alpha_3) \, S_3 + (1-\alpha_1) \, S_1 \, F_{11}$$

$$S_2 = (1-\alpha_1) \, S_1 \, F_{12}$$

$$S_3 = (1-\alpha_1) \, S_1 \, F_{13}$$

Solving these equations simultaneously gives

$$S_1 = \frac{E}{1 - (1 - \alpha_1) \left[(1 - \alpha_3) F_{13} + F_{11} \right]}$$

$$S_2 = \frac{(1 - \alpha_1) F_{12} E}{1 - (1 - \alpha_1) \left[(1 - \alpha_3) F_{13} + F_{11} \right]}$$

$$S_3 = \frac{(1 - \alpha_1) F_{13} E}{1 - (1 - \alpha_1) \left[(1 - \alpha_3) F_{13} + F_{11} \right]} .$$

3.3.2 Thermal Energy

The thermal energy arriving at surfaces A_1, A_2 and A_3 is defined by the following expressions:

$$H_1 = (1 - \epsilon_3) H_3 + \epsilon_3 A_3 \sigma T_3^4 + (1 - \epsilon_1) H_1 F_{11}$$
$$+ \epsilon_1 A_1 \sigma T_1^4 F_{11}$$

$$H_2 = (1 - \epsilon_1) H_1 F_{12} + \epsilon_1 A_1 \sigma T_1^4 F_{12}$$

$$H_3 = (1 - \epsilon_1) H_1 F_{13} + \epsilon_1 A_1 \sigma T_1^4 F_{13} .$$

Solving these three equations simultaneously gives

$$H_1 = \frac{\epsilon_1 A_1 \sigma T_1^4 \left[F_{11} + F_{13} (1 - \epsilon_3) \right] + \epsilon_3 A_3 \sigma T_3^4}{1 - (1 - \epsilon_1) \left[F_{11} + F_{13} (1 - \epsilon_3) \right]} ,$$

3.4 NUMERICAL VALUES

Assume $\alpha_1 = 0.8$. To achieve this value when the basic material has an α value of approximately 0.45, the surfaces of the converters which receive the energy must be grooved. The minimum groove angle is defined by

$$\alpha_a = \frac{1}{1 + \left(\frac{1}{\alpha} - 1\right) \sin \frac{\theta}{2}}$$

$$\sin \frac{\theta}{2} = \frac{1/\alpha_a - 1}{1/\alpha - 1} = \frac{1/0.8 - 1}{1/0.45 - 1} = 0.204$$

$$\theta = 23^{\circ}.$$

Since this result is valid for diffuse surfaces and in this case the surfaces will be somewhat specular, which will result in a higher α_a, a value of $\theta = 30$ degrees was chosen. Therefore

$$\epsilon_a = \frac{1}{1 + \left(\frac{1}{\epsilon} - 1\right) \sin 15^{\circ}}$$

for $\epsilon = 0.25$

$$\epsilon_a = \frac{1}{1 \times 3 \times 0.259} = 0.56 .$$

Substituting $\epsilon_1 = 0.56$ and $\epsilon_3 = 0.25$ the equation for H_1 becomes

$$H_1 = \frac{0.56 \times 20.19 \, \sigma T_1^{4} \left[0.787 + 0.087 \times 0.75\right] + 0.25 \times 1.755 \, \sigma T_3^{4}}{1 - (1-0.56) \left[0.787 + 0.087 \times 0.75\right]}$$

$$H_2 = 0.44 \times 0.126 \, H_1 + 0.56 \times 20.19 \times 0.126 \times 0.126 \, \sigma T_1^{4}$$

$$H_3 = 0.44 \times 0.087 \, H_1 + 0.56 \times 20.19 \times 0.087 \, \sigma T_1^{4} .$$

B-4

Assuming $T_3 = 1200^\circ K$ then

$$\sigma T_3^{\ 4} = 11.78 \text{ watts/cm}^2$$

3.5 NET ENERGY BALANCE

The energy absorbed by the converters and the interstitial spaces is defined by

$$Q_1 = \alpha_1 S_1 + \epsilon_1 (H_1 - A_1 \sigma T_1^{\ 4}).$$

The energy reradiated by the cavity is

$$Q_2 = S_2 + H_2.$$

The energy absorbed by the aperture piece is

$$Q_3 = \alpha_3 S_3 + \epsilon_3 (H_3 - A_3 \sigma T_3^{\ 4}).$$

Numerical Values:

$$\alpha_1 = 0.8, \quad \alpha_3 = 0.5, \quad \epsilon_1 = 0.56, \quad \epsilon_3 = 0.25$$

$$A_1 = 20.19 \text{ cm}^2$$

$$A_3 \sigma T_3^{\ 4} = 1.755 \times 11.78 = 20.67 \text{ watts}$$

$$Q_1 = 0.9593E - 0.56 (4.79 \sigma T_1^{\ 4} - 8.29)$$

$$Q_2 = 0.0302E + 2.277 \sigma T_1^{\ 4} + 0.46$$

$$Q_3 = 0.0104E + 0.25 (1.574 \sigma T_1^{\ 4} - 20.36)$$

which reduce to

$$Q_1 = 0.9593E - 2.6824 \, \sigma \, T_1^{\,4} + 4.64$$

$$Q_2 = 0.0302E + 2.277 \, \sigma \, T_1^{\,4} + 0.46$$

$$Q_3 = 0.0104E + 0.393 \, \sigma \, T_1^{\,4} - 5.09.$$

Table B-1 presents the results of numerical calculations for various values of E and T_1. The value of cavity reradiation Q_2 is compared with black-body radiation, Q_B, expressed by

$$Q_B = A_2 \, \sigma \, T_1^{\,4} = 2.545 \, \sigma \, T_1^{\,4}.$$

In Table B-1 the ratio $\epsilon_a = \dfrac{Q_2}{Q_B}$ is used to make this comparison.

Table B-1. Numerical Results of Cavity Flux Analysis (Watts)

		Case I	E = 1412 watts			
T_E	$2000^O K$	$2100^O K$	$2200^O K$	$2300^O K$	$2400^O K$	$2500^O K$
Q_1	1115.4	1062.5	1002.1	932.6	853.5	764.2
Q_2	249.9	294.9	346.2	405.1	472.3	548.7
Q_e	44.9	53.1	61.8	72.1	83.7	96.7
Q_B	231.2	281.5	338.7	404.7	479.7	564.5
ϵ_a	1.081	1.048	1.022	1.001	0.985	0.972

Case II   E = 1271 watts

T_E	$1900^O K$	$2000^O K$
Q_1	1025.4	980.2
Q_2	207.3	345.7
Q_3	37.2	43.8
Q_B	188.4	231.2
ϵ_a	1.100	1.063

Case III T_E = $2000^O K$

E	700	900	1100	1300
Q_1	432.4	624.3	816.1	1007.9
Q_2	228.5	234.5	240.5	246.6
Q_3	37.8	39.9	42.05	44.13
Q_B	231.2	231.2	231.2	231.2
ϵ_a	0.988	1.014	1.040	1.067

APPENDIX C

CALCULATION OF GENERATOR
HEAT LOSS

APPENDIX C

CALCULATION OF GENERATOR HEAT LOSSES

1. INTRODUCTION

The generator structural heat losses are calculated in this appendix. These losses are discussed in Section 8.4.1 (Volume III).

2. NOMENCLATURE

The nomenclature used in this appendix is defined below:

R = Radius of generator cavity, cm

A_1 = Interstitial area defined by Figure 8-10 in Section 8 of Volume III, cm^2

A_2 = Interstitial area defined by Figure 8-10 in Section 8 of Volume III, cm^2

A_s = Radiation shielding area, cm^2

A_E = Emitter area per converter, cm^2

A_F = Area of the thermionic converter cavity piece, cm^2

Q_I = Interstitial radiation heat losses, watts

Q_s = Shielding radiation heat losses, watts

T_E = Emitter-generator cavity temperature, $^{\circ}$K

σ = Stefan-Boltzmann constant, watts/cm^2 - $^{\circ}$K^4

δ = Width of interstitial area A_1, cm.

3. CALCULATIONS

Expressions for the interstitial and shielding radiation losses are developed below.

3.1 INTERSTITIAL RADIATION LOSS

There are two areas, A_1 and A_2, that would contribute to the interstitial radiation loss. The loss through A_2 was assumed to be negligible because most of the energy passing through A_2 would be collected by the lateral area of the emitters.

A_1 was assumed to have an effective absorptivity of 0.5. Therefore

$$Q_I = 0.5 \, A_1 \, \sigma \, T_E^{\,4} .$$

From Figure 8-10 in Section 8 (Volume III) the numerical value of A_1 is

$$A_1 = 2 \, \pi R \, \delta = 2 \, \pi \times 1.16 \times 0.1 = 0.73 \text{ cm}^2 .$$

Therefore

$$Q_I = 0.5 \times 0.73 \, \sigma \, T_E^{\,4} = 0.36 \, \sigma \, T_E^{\,4} .$$

3.2 SHIELDING LOSS

The shielding loss was assumed to be five percent of the black-body loss that would occur if there were no shielding. The shielding area is given by

$$A_s = 4 \times (A_F - A_E) + A_F .$$

Now

$$A_E = 2 \text{ cm}^2$$
$$A_F = 2.48 \times 2.48 = 6.16 \text{ cm}^2$$
$$A_s = 5 \times 6.16 - 4 \times 2 = 22.8 \text{ cm}^2$$

therefore

$$Q_S = 0.005 \ A_s \ \sigma \ T_E^4 = 1.14 \ \sigma \ T_E^4$$

The sum of the interstitial and shielding losses then is

$$Q_I + Q_S = 1.5 \ \sigma \ T_E^4$$

APPENDIX D

CALCULATION OF CONVERTER
HEAT TRANSFER

APPENDIX D

CALCULATION OF CONVERTER HEAT TRANSFER

1. INTRODUCTION

The converter heat transfer calculations are summarized in this appendix. The results of these calculations are discussed and presented graphically in Section 8.4.2 (Volume III).

2. NOMENCLATURE

The symbols employed in this appendix are defined below:

Q_{ec} = Electron heat transfer to collector of one converter, watts

Q_r = Interelectrode radiation heat transfer of one converter, watts

Q_{cs} = Cesium conduction heat transfer of one converter, watts

Q_s = Conduction heat transfer to emitter support of one converter, watts

Q_{eE} = Electron heat transfer from emitter of one converter, watts

Q_E = Heat input for one converter, watts

T_E = Emitter-generator cavity temperature, $^\circ K$

T_C = Collector face temperature, $^\circ K$

I_o = Converter output current, amperes

p = Cesium pressure, mm-Hg

$\phi*$ = Effective emitter potential, volts

σ = Stefan-Boltzmann constant, watts/cm^2-$^\circ K^4$

3. CALCULATIONS

The governing equations are outlined below.

3.1 HEAT REQUIRED BY EMITTER**

Interelectrode radiation (for two square centimeter emitter area):

$$Q_r = \frac{2\sigma(T_E^4 - T_C^4)}{\frac{1}{0.25} + \frac{1}{0.4} - 1} = \frac{\sigma(T_E^4 - T_C^4)}{2.75} \quad .$$

Cesium conduction:

$$Q_{cs} = \frac{2 \times 0.0244\,\Delta T}{2 + 13.5/p} = \frac{0.0244(T_E - T_C)}{1 + 6.75/p} \quad .$$

Conduction to emitter support:

$$Q_s = 49.3\left[\frac{T_E - T_C}{1000}\right] \quad .$$

Electron heat transfer from emitter:

$$Q_{eE} = \phi^* \times I_o \quad .$$

Calculated values for these quantities are presented in Table D-1.

3.2 HEAT RECEIVED BY COLLECTOR-RADIATOR STRUCTURE

Interelectrode radiation:

$$Q_r = \frac{(T_E^4 - T_C^4)}{2.75} \quad .$$

**The numerical assumptions made in this appendix are presented and discussed in Section 4.2.2 of Volume II.

Cesium conduction:

$$Q_{cs} = \frac{0.0244\,(T_E - T_C)}{1 + 6.75/p}$$

Conduction to emitter support (only 1/3 of the emitter heat loss is assumed to reach the collector-radiator structure)

$$Q_s = 1/3 \times 49.3 \left[\frac{T_E - T_C}{1000}\right] = 16.4 \left[\frac{T_E - T_C}{1000}\right]$$

Electron heat transfer to collector:

$$Q_{ec} = 1.6 \times I_o$$

Calculated values for these quantities are presented in Table D-2.

Table D-1. Calculation of Heat Required By One Converter (Watts)

		Emitter Temperature (^{O}K)							
		1800	1900	2000	2100	2200	2300	2400	2500
	Q_r	19.6	24.8	31.0	38.1	46.3	55.7	66.5	78.6
	Q_{cs}	9.3	10.5	11.6	12.8	14.0	15.1	16.3	17.5
	Q_s	39.4	44.4	49.3	54.2	59.2	64.1	69.0	73.9
Q_{eE}	@ 10A	31.7	31.7	31.7	31.7	31.7	31.7	31.7	31.7
	@ 30A	89.7	89.7	89.7	89.7	89.7	89.7	89.7	89.7
	@ 50A	145.0	145.0	145.0	145.0	145.0	145.0	145.0	145.0
Q_E	@ 0A	68.4	79.7	91.9	105.1	119.4	134.9	151.8	170.0
	@ 10A	100.1	111.4	123.6	136.8	151.1	166.6	183.5	201.7
	@ 30A	158.1	169.4	181.6	194.8	209.1	224.6	241.5	259.7
	@ 50A	213.1	224.7	236.9	250.1	264.4	279.9	296.5	315.0

D-3

Table D-2. Calculation of Heat Transferred to Collector-Radiator Structure (Watts)

		Emitter Temperature ($^{\circ}$K)							
		1800	1900	2000	2100	2200	2300	2400	2500
	Q_r	19.6	24.8	31.0	38.1	46.3	55.7	66.5	78.6
	Q_{cs}	9.3	10.5	11.6	12.8	14.0	15.1	16.3	17.5
	Q_s	13.1	14.8	16.4	18.0	19.7	21.3	23.0	24.6
Q_{eC}	@ 10A	16.0	16.0	16.0	16.0	16.0	16.0	16.0	16.0
	@ 30A	48.0	48.0	48.0	48.0	48.0	48.0	48.0	48.0
	@ 50A	80.0	80.0	80.0	80.0	80.0	80.0	80.0	80.0
Q_{CR}	@ 0A	42.0	50.1	59.0	68.9	80.0	92.2	105.7	120.1
	@ 10A	58.1	66.1	75.0	84.9	95.9	108.2	121.7	136.7
	@ 30A	90.1	98.1	107.0	116.9	128.0	140.2	153.7	168.7
	@ 50A	122.1	130.1	139.0	148.9	160.0	172.2	185.7	200.7

D-4

APPENDIX E

RADIATOR DESIGN CALCULATIONS

APPENDIX E

RADIATOR DESIGN CALCULATIONS

1. INTRODUCTION

This appendix contains the radiator design calculations. The tabular results contained in this appendix are discussed and presented graphically in Section 8.4.3 (Volume III).

2. NOMENCLATURE

The symbols used in this analysis are defined below:

T_B = Temperature at base of collector, °K

T_C = Collector face temperature, °K

T_x = Temperature at distance x, °K

T_i = Temperature at surface i, °K

Q_o = Initial value of heat to be dissipated, watts

Q_x = Heat flow at distance x, watts

A_F = Cross sectional area of four radiator fins, cm^2

A_i = Area of element i, cm^2

k = Thermal conductivity, watts/cm- °C

ℓ = Length of element i, cm

ρ = Density, gm/cm^3

M = Mass, grams

h = Thickness of radiator fin, cm

c = Length of radiator fin, cm

a = Radial dimension of radiator fin at collector interface, cm

b = Radial dimension of radiator fin at the maximum span point, cm

R_T = Thermal resistance of collector structure, °C/watt

3. CALCULATIONS

3.1 VALUE OF COLLECTOR BASE TEMPERATURE, T_B

The optimum value of the collector face temperature, T_C, is

$$T_C \text{ (optimum)} = 971°K \text{ at 0.9 volts}$$
$$= 1024°K \text{ at 0.8 volts.}$$

Therefore, at the design point voltage of 0.85 the optimum T_C would be 998 °K.

Collector heat transfer at the design point is

Electron heating	67.9 watts
Interstitial radiation	31.0
Cesium conduction	12.8
Total	111.7

Referring to Figure 8-13 in Section 8.4.3 (Volume III) the collector thermal resistance is

A_1 = 2.01 - 0.125 = 1.885 cm^2 $\ell_1/A_1 = 0.106$

A_2 = 1.697 - 0.125 = 1.572 $\ell_2/A_2 = 0.382$

A_3 = 2.086 - 0.125 = 1.961 $\ell_3/A_3 = 0.560$

$$A_4 = 3.563 - 0.125 = 3.438 \qquad \ell_4/A_4 = 0.111$$

$$A_5 = 12.946 - 0.125 = 12.821 \qquad \ell_5/A_5 = 0.119*$$

$$\Sigma \ell_i/A_i = 1.27 \qquad cm^{-1}$$

The thermal conductivity of molybdenum is 1.15 watts - cm/$^\circ$C.

The collector temperature drop then is

$$\Delta T_4 = 111.7 \times \frac{1.278}{1.15} = 124^\circ C.$$

Adding a 30°C temperature drop to carry the heat to the fin yields a total $\Delta T_C = 154^\circ$C. The effective thermal resistance then is

$$R_T = \frac{\Delta T}{q} = \frac{154}{111.7} = 1.38^\circ C/watt, \quad \text{and the temperature at the base of the}$$

collector is

$$T_B = 998 - 154 = 844^\circ K.$$

3.2 RADIATOR GEOMETRY

Refer to Figure 8-14 in Section 8.4.3 (Volume III).

$$\psi = \tan^{-1} \frac{b-a}{c}$$

$$\psi = 42^\circ 50'$$

$b = 5.2$ cm

$a = 2.03$ cm

$c = 3.42$ cm

$$\frac{b-a}{c} = 0.926$$

---

* The value of ℓ_5 assumed is three times the actual value to allow for the sudden changes in cross section on the top side of this element.

$$A_B = 2b^2 = 27.0 \text{ cm}^2$$

$$A_L = 2c \left[(2a + c (\tan 42° 50')) \right] \sqrt{2 + \tan^2 42° 50'}$$

$$= 6.84 (4.06 + 3.42 \times 0.926) \sqrt{2 + (0.926)^2}$$

$$= 83.6 \text{ cm}^2$$

$$A_B / A_L = 0.323$$

$$(A_R)_x = 1.323 (A_L)_x$$

$$(A_L)_x = 2x \left[2a + x (\tan 42° 50') \right] \sqrt{2 + \tan^2 42° 50'}$$

$$\Delta(A_L)_x = 4 \times 1.323 (a + 0.926 x) 1.69 \Delta x$$

$$\Delta(A_R)_x = (18.02 + 0.83 x) \Delta x \tag{1}$$

3.3 COLLECTOR HEAT TRANSFER AT DESIGN POINT

The design point current is 42.4 amperes. Figure 8-12 in Section 8.4.2 (Volume III) gives Q_{CR} = 126 watts for a current of 42.4 amperes. Q_{CR} = 128.1 watts has been used in these calculations.

3.4 HEAT TRANSFER CROSS-SECTION

Referring again to Figure 8-14 in Section 8.4.3 (Volume III).

$$A_F = 4 (a - e + x \tan 42^\circ 50') t$$

$$a = 2.03 \text{ cm}$$
$$e = 0.32 \text{ cm}$$
$$\tan 42^\circ 50' = 0.926$$

$$A_F = 4 (2.03 - 0.32 + 0.926 \, x) \, t \qquad\qquad (2)$$
$$= (6.84 + 3.704 \, x) \, t$$

3.5 RADIATOR MASS

The density of copper is, $\rho = 8.95 \text{ gm/cm}^3$.

The mass of the radiator can be expressed as

$$M = \rho V = 8.95 \int_0^c A_F \, dx$$

$$= 8.95 \left(6.84c + 3.704 \frac{c^2}{2}\right) h$$

$$= (61.2 \, c + 16.6 \, c^2) \, h \qquad\qquad (3)$$

Equations 1, 2 and 3 were used to compute the results presented in Table E-1.

Table E-1. Calculation of Radiator Heat Transfer and Temperature Distribution

Run No. 1

$T_B = 800°K$ $\qquad$ $Q_o = 128.1$ $\qquad$ $h = 0.08$ cm

x	Q_x	T_x	A_F	T_x'	ΔT_x	ΔA_R	ΔQ_x
0	128.10	800.00	0.5472	65.029	19.51	5.40	11.34
0.3	116.76	780.49	0.6361	51.01	15.30	5.475	10.46
0.6	106.30	765.19	0.7249	40.74	12.22	5.549	9.849
0.9	96.45	752.97	0.8139	32.92	9.876	5.624	9.279
1.2	87.17	743.09	0.9028	26.82	8.046	5.698	8.976
1.5	78.19	735.04	0.9917	21.91	6.573	5.774	8.661
1.8	69.53	728.47	1.0806	17.87	5.361	5.848	8.479
2.1	61.05	723.11	1.1695	14.50	4.350	5.923	8.351
2.4	52.69	718.76	1.258	11.634	3.490	5.998	8.247
2.7	44.44	715.27	1.347	9.1647	2.7494	6.0723	8.1976
3.0	36.24	712.62	1.436	7.0110	2.1033	6.1470	8.1448
3.3	28.095	710.42	1.525	5.1174	1.5352	6.2217	8.0882
3.6	20.007	708.88	1.6139	3.4435	1.0331	6.296	8.1848
3.9	11.822	707.85	1.7028	1.9285	0.5786	6.3711	8.1869
4.2	3.6351	707.27	1.792	0.5635	0.1691	6.4458	8.2829
4.5	- 4.6478	707.01	1.8806	-0.6865			

c = 4.335 cm

M = 46.18 gms

Run No. 2

$T_B = 800°K$ $\qquad$ $Q_o = 128.1$ $\qquad$ $h = 0.14$ cm

x	Q_x	T_x	A_F	T_x'	ΔT_x	ΔA_R	ΔQ_x
0	128.10	800.00	0.9576	37.16	11.15	5.40	11.34
0.3	116.76	788.85	1.113	29.14	8.742	5.475	10.81
0.6	105.95	780.11	1.269	23.19	6.957	5.549	10.60
0.9	95.35	773.15	1.424	18.59	5.577	5.624	10.29
1.2	85.06	767.57	1.579	14.96	4.488	5.699	10.20
1.5	74.86	763.08	1.735	11.98	3.594	5.774	10.10
1.8	64.76	759.49	1.891	9.512	2.854	5.848	10.00
2.1	54.76	756.64	2.047	7.433	2.229	5.923	9.921
2.4	44.84	754.41	2.202	5.656	1.6968	5.998	10.05
2.7	34.79	752.71	2.358	4.0987	1.2296	6.072	10.02
3.0	24.77	751.48	2.513	2.738	0.8214	6.147	10.11
3.3	14.66	750.66	2.669	1.526	0.4578	6.222	10.17
3.6	4.49	750.20	2.824	0.4415	0.1325	6.296	10.29
3.9	-5.80	750.07	2.979	-0.5405			

c = 3.735 cm

M = 64.4 gms

Table E-1. Calculation of Radiator Heat Transfer and
Temperature Distribution (Cont)

Run No. 3							
$T_B = 800^\circ K$			$Q_o = 128.1$		$h = 0.08$ cm		
x	Q_x	T_x	A_F	T_x'	ΔT_x	ΔA_R	ΔQ_x
0	128.10	800.00	1.368	26.01	7.803	5.40	11.34
0.3	116.76	792.20	1.590	20.39	6.117	5.475	11.09
0.6	105.67	786.08	1.813	16.19	4.857	5.549	10.90
0.9	94.77	781.22	2.035	12.94	3.882	5.624	10.77
1.2	84.00	777.33	2.257	10.34	3.102	5.699	10.69
1.5	73.31	774.23	2.479	8.215	2.465	5.774	10.68
1.8	62.63	771.77	2.701	6.440	1.932	5.848	10.67
2.1	51.96	769.84	2.924	4.934	1.480	5.923	10.66
2.4	41.30	768.36	3.146	3.647	1.094	5.997	10.73
2.7	30.57	767.26	3.368	2.521	0.7563	6.072	10.78
3.0	19.79	766.50	3.590	1.531	0.4593	6.147	10.91
3.3	8.88	766.04	3.813	0.6467	0.1940	6.222	11.04
3.6	-2.16	765.85	4.035	-0.1486			

c = 3.0 cm
M = 66.6 gms

Run No. 4							
$T_B = 800^\circ K$			$Q_o = 128.10$		$h = 0.14$ cm		
x	Q_x	T_x	A_F	T_x'	ΔT_x	ΔA_R	ΔQ_x
0	128.10	800.00	1.778	20.01	6.003	5.40	11.34
0.3	116.76	793.99	2.067	15.69	4.707	5.475	11.09
0.6	105.67	789.28	2.356	12.46	3.738	5.549	10.68
0.9	94.99	785.54	2.645	9.976	2.993	5.624	10.96
1.2	84.03	782.55	2.934	7.956	2.387	5.698	10.96
1.5	73.07	780.16	3.223	6.298	1.889	5.774	11.03
1.8	62.04	778.27	3.512	4.907	1.4722	5.848	11.11
2.1	50.93	776.79	3.801	3.723	1.117	5.923	11.11
2.4	39.82	775.67	4.089	2.705	0.8115	5.998	11.16
2.7	28.66	774.86	4.379	1.819	0.546	6.072	11.23
3.0	17.43	774.31	4.668	1.038	0.3114	6.147	11.37
3.3	6.06	773.99	4.956	0.3396	0.1019	6.222	11.51
3.6	-5.45	773.89	5.245	-0.2886			

c = 3.48 cm
M = 107.64 gms

Table E-1. Calculation of Radiator Heat Transfer and Temperature Distribution (Cont)

Run No. 5

$T_B = 800^{\circ}K$ $\quad\quad Q_o = 128.1$ $\quad\quad h = 0.32$ cm

x	Q_x	T_x	A_F	T_x'	ΔT_x	ΔA_R	ΔQ_x
0	128.10	800.00	2.189	16.26	4.878	5.40	11.34
0.3	116.76	795.12	2.448	13.25	3.975	5.475	11.22
0.6	105.54	791.15	2.899	10.11	3.033	5.549	11.18
0.9	94.36	788.12	3.256	8.05	2.415	5.624	11.11
1.2	83.25	785.71	3.611	6.41	1.923	5.699	11.11
1.5	72.14	783.79	3.967	5.052	1.516	5.774	11.17
1.8	60.97	782.27	4.322	3.918	1.175	5.848	11.26
2.1	49.71	781.09	4.678	2.952	0.8856	5.923	11.34
2.4	38.37	780.20	5.033	2.118	0.6354	5.998	11.39
2.7	26.98	779.56	5.389	1.3907	0.4172	6.0723	11.54
3.0	15.44	779.14	5.745	0.7466	0.2239	6.147	11.08
3.3	3.76	778.92	6.100	0.1712	0.0514	6.222	11.82
3.6	-8.06	778.78	6.456	-0.368	-0.1104		

c = 3.39 cm
M = 127.71 gms

Run No. 6

$T_B = 800^{\circ}K$ $\quad\quad Q_o = 128.1$ $\quad\quad h = 0.38$ cm

x	Q_x	T_x	A_F	T_x'	ΔT_x	ΔA_R	ΔQ_x
0	128.10	800.00	2.599	13.69	4.107	5.40	11.34
0.3	116.76	795.89	3.0215	10.73	3.219	5.475	11.22
0.6	105.54	792.67	3.444	8.518	2.555	5.549	11.24
0.9	94.30	790.12	3.866	6.774	2.032	5.624	11.25
1.2	83.05	788.09	4.288	5.379	1.614	5.699	11.26
1.5	71.79	786.48	4.710	4.233	1.269	5.774	11.32
1.8	60.47	785.21	5.133	3.272	0.9816	5.848	11.40
2.1	49.07	784.23	5.555	2.455	0.7364	5.923	11.49
2.4	37.58	783.49	5.977	1.746	0.5239	5.998	11.58
2.7	26.00	782.97	6.399	1.128	0.3384	6.072	11.69
3.0	14.31	782.63	6.822	0.5826	0.1748	6.147	11.83
3.3	2.48	782.46	7.244	0.0950	0.8835	6.222	11.98
3.6	-9.50	781.58	7.666	-0.3443			

c = 3.36 cm
M = 149.68 gms

Table E-1. Calculation of Radiator Heat Transfer and Temperature Distribution (Cont)

Run No. 7

$T_B = 900\ ^{\circ}K \qquad Q_o = 128.1 \qquad h = 0.20\ cm$

x	Q_x	T_x	A_F	T'_x	ΔT_x	ΔA_R	ΔQ_x
0	128.10	900.00	1.3680	26.010	7.803	5.400	18.09
0.3	110.01	892.19	1.5902	19.217	5.765	5.4747	17.765
0.6	92.245	886.43	1.8125	14.138	4.2414	5.5494	17.481
0.9	74.764	882.19	2.0347	10.207	3.0621	5.6241	17.435
1.2	57.329	879.128	2.2569	7.056	2.1168	5.699	18.008
1.5	39.321	877.01	2.4792	4.4056	1.3217	5.7736	17.465
1.8	22.00	875.69	2.7014	2.2622	0.6787	5.8482	17.545
2.1	4.455	875.01	2.9237	0.4232	0.1269	5.9229	17.768
2.4	-13.314	874.87	3.1459	-1.1756			

$c = 2.18\ cm$

$M = 42.46\ gms$

Run No. 8

$c = 3.0\ cm \qquad h = 0.20\ cm$

$T_B = 400\ ^{\circ}K$

x	T_x	ΔA_R	ΔQ_x	Q_x	A_F	T'_x	ΔT_x
3.0	400.00	6.072	0.8744	0.8744	3.368	0.0721	0.0216
2.7	400.02	5.997	0.8636	1.7380	3.146	0.1534	0.0460
2.4	400.07	5.923	0.8529	2.5909	2.924	0.2460	0.0738
2.1	400.14	5.848	0.8479	3.4389	2.701	0.3536	0.1061
1.8	400.25	5.774	0.8372	4.2761	2.479	0.4791	0.1437
1.5	400.39	5.699	0.8264	5.1025	2.257	0.6279	0.1884
1.2	400.58	5.624	0.8155	5.9179	2.035	0.8078	0.2423
0.9	400.82	5.549	0.8102	6.7281	1.813	1.0308	0.3092
0.6	401.13	5.475	0.7994	7.5275	1.590	1.3150	0.3945
0.3	401.5	5.400	0.7884	8.3159	1.368	1.6885	0.5066
0	402.06						

$T_B = 402.0\ ^{\circ}K \qquad Q_o = 8.31$

Table E-1. Calculation of Radiator Heat Transfer and Temperature Distribution (Cont)

Run No. 9

c = 3.0 cm   h = 0.20 cm
$T_B = 500^{\circ}K$

x	T_x	ΔA_R	ΔQ_x	Q_x	A_F	T_x'	ΔT_x
3.0	500.00	6.072	1.943	1.943	3.368	0.1602	0.0481
2.7	500.05	5.997	1.9190	3.8620	3.146	0.3410	0.1023
2.4	500.15	5.923	1.8954	5.7574	2.924	0.5467	0.1640
2.1	500.31	5.848	1.8714	7.6288	2.701	0.7844	0.2353
1.8	500.55	5.774	1.8766	9.5054	2.479	1.0651	0.3195
1.5	500.87	5.699	1.8522	11.3576	2.257	1.3978	0.4193
1.2	501.29	5.624	1.8278	13.1854	2.035	1.7998	0.5399
0.9	501.83	5.549	1.8034	14.989	1.813	2.2964	0.6889
0.6	502.52	5.475	1.7794	16.768	1.590	2.9294	0.8788
0.3	503.39	5.400	1.7550	18.523	1.368	3.7610	1.1283
0	504.52						

$T_B = 18.52^{\circ}K \quad Q_o = 504.5$

Run No. 10

c - 3.0 cm   h = 0.20 cm
$T_B = 600^{\circ}K$

x	T_x	ΔA_R	ΔQ_x	Q_x	A_F	T_x'	ΔT_x
3.0	600.00	6.072	3.734	3.7343	3.368	0.3079	0.0924
2.7	600.09	5.997	3.6882	7.4225	3.146	0.6554	0.1966
2.4	600.29	5.923	3.6426	11.065	2.924	1.0508	0.3152
2.1	600.61	5.848	3.5965	14.662	2.701	1.5076	0.4523
1.8	601.06	5.774	3.6088	18.271	2.479	2.0473	0.6142
1.5	601.67	5.699	3.5619	21.833	2.257	2.6871	0.8061
1.2	602.48	5.624	3.515	25.348	2.035	3.4600	1.038
0.9	603.52	5.549	3.4681	28.816	1.813	4.4149	1.3245
0.6	604.84	5.475	3.4493	32.265	1.590	5.6368	1.6910
0.3	606.53	5.400	3.4830	35.748	1.368	7.2584	2.1775
0	608.71						

$T_B = 608.7^{\circ}K \quad Q_o = 35.75$

Table E-1. Calculation of Radiator Heat Transfer and Temperature Distribution (Cont)

Run No. 11							

$c = 3.0$ cm $h = 0.20$ cm
$T_B = 700^\circ$K

x	T_x	ΔA_R	ΔQ_x	Q_x	A_F	T_x'	ΔT_x
3.0	700.00	6.072	7.4686	7.4686	3.368	0.6159	0.1848
2.7	700.18	5.997	7.3763	14.845	3.146	1.3108	0.3932
2.4	700.57	5.923	7.2853	22.130	2.924	2.1016	0.6305
2.1	701.20	5.848	7.2515	29.382	2.701	3.0212	0.9064
1.8	702.11	5.774	7.2175	36.599	2.479	4.1011	1.2303
1.5	703.34	5.699	7.1238	43.714	2.257	5.3801	1.6140
1.2	704.95	5.624	7.0862	50.800	2.035	6.9342	2.0803
0.9	707.03	5.549	7.1305	57.930	1.813	8.8755	2.6627
0.6	709.69	5.475	7.1449	65.075	1.590	11.3687	3.4106
0.3	713.10	5.400	9.4669	74.542	1.368	15.135	4.5405
0	717.64						

$$T_B = 717.6^\circ K \qquad Q_o = 74.5$$

Run No. 12							

$c = 3.0$ cm $h = 0.20$ cm
$T_B = 800^\circ$K

x	T_x	ΔA_R	ΔQ_x	Q_x	A_F	T_x'	ΔT_x
3.0	800.00	6.072	12.751	12.751	3.368	1.0516	0.3155
2.7	800.32	5.997	12.594	25.345	3.146	2.2379	0.6714
2.4	800.99	5.923	12.498	37.842	2.924	3.5937	1.0781
2.1	802.07	5.848	12.369	50.211	2.701	5.1630	1.5489
1.8	803.62	5.774	12.27	62.481	2.479	7.001	2.1004
1.5	805.72	5.699	12.24	74.705	2.257	9.1945	2.7584
1.2	808.48	5.624	12.23	86.937	2.035	11.8669	3.5601
0.9	812.04	5.549	12.347	99.284	1.813	15.211	4.5634
0.6	816.60	5.475	12.401	111.685	1.590	19.512	5.8535
0.3	822.45	5.400	12.56	124.24	1.368	25.226	7.5679
0	830.02						

$$T_B = 830.0^\circ K \qquad Q_o = 124.2$$

APPENDIX F

CESIUM RESERVOIR DESIGN CALCULATIONS

APPENDIX F

CESIUM RESERVOIR DESIGN CALCULATIONS

1. INTRODUCTION

The cesium reservoir design calculations are presented in this appendix. The results tabulated in this appendix are discussed and presented graphically in Section 8.4.4 (Volume III).

2. NOMENCLATURE

The nomenclature employed in this appendix is defined below:

F_{ij} = Radiation view factor from surface i to surface j

A_i = Area of element i, cm^2

H_i = Thermal energy arriving at surface i, watts

Q_i = Net energy transfer to area element i, watts

Q_R = Energy transferred to the reservoir, watts

ϵ_i = Thermal emissivity of surface i

T_i = Temperature of area element i, ^oK

T_R = Cesium reservoir temperature, ^oK

c = Length of radiator fin, cm

h = Thickness of radiator fin, cm

e = Radiator radial fin clearance for cesium tube, cm

d = Diameter of cesium tube, cm

3. CALCULATIONS

3.1 VIEW FACTORS

Refer to Figures 8-18 and 8-19 in Section 8.4.4 (Volume III)

$$c = 2.7 \text{ cm} \qquad\qquad e = 0.32 \text{ cm}$$

$$h = 0.2 \text{ cm} \qquad\qquad d = 0.48 \text{ cm}$$

$$F_{13} = 1 - \frac{4\gamma}{360} \qquad\qquad \gamma = 2 \tan^{-1} \frac{0.1}{0.32} = 2 \tan^{-1} 0.312$$

$$F_{13} = 1 - \frac{136}{360} = 0.622 \qquad\qquad = 34^{\circ}$$

$$F_{12} = 0.378$$

$$F_{21} = \frac{A_1}{A_2} F_{12} = \frac{\pi \times 0.48}{4 \times 0.2} F_{12}$$

$$= 1.89 \times 0.378 = 0.712$$

3.2 HEAT TRANSFER FOR ELEMENT ϕ_X

Refer to Figure 8-19 in Section 8.4.4 (Volume III).

$$Q_1 = (1 - \epsilon_2) Q_2 F_{21} + \epsilon_2 \sigma T_2^4 F_{21} A_2$$

$$Q_2 = (1 - \epsilon_1) Q_1 F_{12} + \epsilon_1 \sigma T_1^4 F_{12} A_1$$

solving

$$Q_1 = (1 - \epsilon_2) F_{21} \left[(1 - \epsilon_1) Q_1 F_{12} + \epsilon_1 \sigma T_1^4 F_{12} A_1 \right]$$
$$+ \epsilon_2 \sigma T_2^4 F_{21} A_2$$

$$Q_1 \left[1 - (1 - \epsilon_2)^2 F_{21} F_{12} \right] = (1 - \epsilon_2) F_{21} F_{12} \epsilon_1 \sigma T_1^4 A_1$$
$$+ \epsilon_2 \sigma T_2^4 F_{21} A_2$$

The net energy absorbed by surface (1) is

$$q = \epsilon_1 Q_1 - \epsilon_1 \sigma T_1^4 A_1$$

$$q = \epsilon_1 \left\{ \frac{F_{21} \left[F_{12} \epsilon_1 (1 - \epsilon_2) \sigma T_1^4 A_1 + \epsilon_2 \sigma T_2^4 A_2 \right]}{1 - (1 - \epsilon_2)^2 F_{21} F_{12}} - \sigma T_1^4 A_1 \right\}$$

$$q = \epsilon_1 \left\{ \frac{\left[F_{21} \left[F_{12} \epsilon_1 (1 - \epsilon_2) - 1 + (1 - \epsilon_2)^2 F_{21} F_{12} \right] \sigma T_1^4 A_1 + F_{21} \epsilon_2 \sigma T_2^4 A_2 \right]}{1 - (1 - \epsilon_2)^2 F_{21} F_{12}} \right\}$$

The reported emissivity values for nickel and copper are

$\epsilon_1 = 0.10$ (nickel at 300°C)

$\epsilon_2 = 0.07$ (copper at 500°C).

Allowing for surface roughness and normal chemical conditions the values used in this analysis were

$\epsilon_1 = 0.18$

$\epsilon_2 = 0.13$.

therefore

$$F_{21} F_{12} \epsilon_1 (1 - \epsilon_2) - 1 + (1 - \epsilon_2)^2 F_{21} F_{12} = (1 - \epsilon_2) F_{21} F_{12} \left[\epsilon_1 + 1 - \epsilon_2 \right] - 1$$

$$= 0.37 \times 0.712 \times 0.378\ (0.18 + 1 - 0.13) - 1$$

$$= -0.754$$

$$1 - (1 - \epsilon_2)^2\ F_{21}\ F_{12} = 1 - (0.87)^2 \times 0.712 \times 0.378$$

$$= 0.796$$

$$F_{21}\ \epsilon_2 = 0.712 \times 0.13 = 0.0925$$

$$\cfrac{\epsilon_1}{\left[1 - (1 - \epsilon_2)^2\ F_{21}\ F_{12}\right]} = \frac{0.18}{0.796} = 0.226$$

$$q = 0.226\ (-0.754\ \sigma\ T_1^4 A_1 + 0.0925\ \sigma T_2^4 A_2)$$

$$= 0.021\ \sigma\ T_2^4 A_2 - 0.17\ \sigma T_1^4 A_1.$$

For a length dx

$$A_1 = \pi D\ dx = 1.51\ dx$$

$$A_2 = 4 \times 0.2\ dx = 0.8\ dx$$

Finally

$$dq = (0.017\ \sigma\ T_2^4 - 0.256\ \sigma\ T_1^4)\ dx.$$

3.3   FINITE DIFFERENCE HEAT TRANSFER EQUATION

For $0 < x < 3.0$ centimeters

$$\Delta Q_x = (-0.017\ \sigma\ T_R^4 + 0.256\ \sigma\ T_x^4)\ \Delta x$$

$$Q_x = ksT_x \qquad\qquad T_x = \frac{\Delta T_x}{\Delta x}$$

A value of $T_R = 830^\circ K$ is assumed at the design point.

For x > 3.0 centimeters

$$Q_x = \epsilon_1 \sigma T_x^4 A_1$$

$$= 0.18 \times 1.51 \sigma T_x^4 \Delta X$$

$$= 0.272 \sigma T_x^4 \Delta X$$

Value of ks

$$k = 0.65 \text{ watts/cm} - {}^oC \text{ at } 450{}^oK$$

$$S = \frac{3}{16} \text{ OD} \times 0.015 \text{ watt} = \frac{\pi}{4} \text{ (OD-ID) (OD+ID)}$$

OD	= 0.1875	OD-ID	= 0.03
ID	= 0.1575	OD-ID	= 0.345

$$s = \frac{\pi}{4} \times 0.01035 = 0.00814 \text{ in}^2 = 0.0525 \text{ cm}^2$$

$$ks = 0.0341 \text{ watts} - \text{cm}/{}^oC.$$

3.4 VALUE OF Q_R

Lateral area of reservoir

$$\ell_{Cu} = 2.1 \text{ cm} \qquad d_{Cu} = 0.48 \text{ cm}$$

$$A_{L_{Cu}} = \pi d\ell = 1.51 \times 2.1 = 3.17 \text{ cm}^2$$

$$\ell_{Ni} = 0.5 \text{ cm} + 50\% = 0.75 \text{ cm}$$

$$d_{Ni} = 1.28 \text{ cm}$$

$$A_{L_{Ni}} = \pi d\ell = 4.02 \times 0.75 = 3.0 \text{ cm}^2.$$

Reservoir temperature at optimum:

Optimum at 0.8 = 641°K

Optimum at 0.9 = 637°K

At 0.85 volts,

T_R optimum = 639°K

σT^4 at 639°K = 0.946 watt/cm^2

Emissivity values for reservoir:

ϵ_{Ni} = 0.10

ϵ_{Cu} = 0.07

$$Q_R = (3.17 \times 0.07 + 3.0 \times 0.1) \sigma T_R^4$$

$$= (0.222 + 0.3) \sigma T_R^4$$

$$= 0.522 \sigma T_R^4 .$$

At 639°K:

$$Q_R = 0.494 \text{ watts.}$$

The expressions developed in the preceding sections were used to perform the cesium reservoir design calculations summarized in Tables F-1 and F-2.

Table F-1. Calculation of Cesium Tube Heat Transfer

			Run No. 1		
		$T_B = 844^{O}K$		$Q_o = 3.0$ watts	
X	Q_x	T_x'	ΔT	T_x	ΔQ_x
0	3.0	87.976	13.196	830.80	0.1934
0.3	2.8066	82.305	24.691	806.11	0.1704
0.6	2.6362	77.308	23.192	782.92	0.1494
0.9	2.4868	72.926	21.878	761.04	0.1322
1.2	2.3546	69.0498	20.7149	740.33	0.1168
1.5	2.2378	65.6246	19.6874	720.64	0.1035
1.8	2.1343	62.5894	18.7768	701.86	0.0911
2.1	2.0432	59.9178	17.9753	683.885	0.0807
2.4	1.9625	57.551	17.265	666.62	0.0715
2.7	1.8910	55.455	16.637	649.98	0.0638
3.0	1.8272	53.584	16.075	633.91	
			Run No. 2		
		$T_B = 844^{O}K$		$Q_o = 2.2$ watts	
0	2.2	64.516	9.677	834.3	0.1975
0.3	2.0025	58.724	17.617	816.68	0.1797
0.6	1.8228	53.455	16.037	800.64	0.1649
0.9	1.6579	48.619	14.586	786.05	0.1521
1.2	1.5058	44.158	13.247	772.80	0.1410
1.5	1.3648	40.023	12.007	760.8	0.1322
1.8	1.2326	36.147	10.844	749.9	0.1245
2.1	1.1081	32.496	9.7487	740.15	0.1168
2.4	0.9913	29.070	8.7211	731.43	0.1107
2.7	0.8806	25.824	7.7472	723.68	0.1053
3.0	0.7753	22.74	6.8208	716.86	0.1216
3.3	0.6537	19.170	5.7510	711.11	0.1182
3.6	0.5355	15.704	4.711	706.39	0.1142
3.9	0.4213	12.355	3.7064	702.68	0.1118
4.2	0.3095	9.0702	2.7229	699.96	0.1109
4.5	0.1986	5.8240	1.747	698.21	0.1093
4.8	0.0893	2.6187	0.7856	697.42	0.1085

Table F-1. Calculation of Cesium Tube Heat Transfer

Run No. 3

$$T_B = 844^\circ K \qquad Q_o = 2.5 \text{ watts}$$

X	Q_x	T_x'	ΔT	T_x	ΔQ_x
0	2.5	73.314	10.997	833.00	0.1967
0.3	2.303	67.545	20.264	812.74	0.1759
0.6	2.127	62.378	18.71	794.03	0.1598
0.9	1.9672	57.689	17.307	776.72	0.1445
1.2	1.8227	53.452	16.035	760.69	0.1321
1.5	1.6906	49.578	14.873	745.82	0.1207
1.8	1.5699	46.038	13.811	732.01	0.1114
2.1	1.4585	42.771	12.831	719.18	0.1029
2.4	1.3556	39.754	11.926	707.25	0.0945
2.7	1.2611	36.982	11.095	696.16	0.0876
3.0	1.1735	34.41	10.32	685.84	0.1012
3.3	1.0723	31.45	9.435	676.41	0.0963
3.6	0.9760	28.622	8.5865	667.82	0.0906
3.9	0.8854	25.965	7.7894	660.04	0.0873
4.2	0.7981	23.405	7.0214	653.02	0.0832
4.5	0.7149	20.965	6.2895	646.731	0.0799
4.8	0.6350	18.622	5.5867	641.44	0.0783
5.1	0.5567	16.326	4.897	636.25	

Table F-2. Reservoir Temperature Versus T_B

			Run No. 1	$T_R = 400^{\circ}K$	
x	T_x	ΔQ_x	Q_x	T_x'	ΔT_x
4.8	400.00	–	0.0759	2.2258	0.33387
4.5	400.33	0.0119	0.0878	2.5735	0.7721
4.2	401.10	0.0119	0.0997	2.9225	0.8768
3.9	401.97	0.0121	0.1118	3.2779	0.9834
3.6	402.95	0.0122	0.1239	3.6351	1.0905
3.3	404.04	0.0122	0.1361	3.9899	1.1969
3.0	405.24	0.0122	0.1483	4.3501	1.3503
2.7	406.55	0.0117	0.1599	4.6913	1.4074
2.4	407.96	0.0119	0.1718	5.0382	1.5115
2.1	409.47	0.0122	0.1840	5.3962	1.6189
1.8	411.09	0.0123	0.1963	5.7562	1.7269
1.5	412.82	0.0125	0.2088	6.1237	1.8371
1.2	414.66	0.0128	0.2216	6.4992	1.9498
0.9	416.61	0.0131	0.2347	6.8814	2.0644
0.6	418.67	0.0133	0.2479	7.2723	2.1817
0.3	420.85	0.0136	0.2615	7.6676	2.3003
0	423.15	0.0141	0.2756	8.0807	1.2121

$$T_B = 424.36$$

			Run No. 2	$T_R = 500^{\circ}K$	
4.8	500.00	–	0.1840	5.3958	0.8094
4.5	500.81	0.0290	0.2130	6.2477	1.8743
4.2	502.68	0.0294	0.2424	7.1078	2.1323
3.9	504.81	0.0299	0.2723	7.9843	2.3953
3.6	507.21	0.0305	0.3028	8.8803	2.6641
3.3	509.87	0.0311	0.3339	9.7914	2.9374
3.0	512.81	0.0321	0.3659	10.7322	3.2197
2.7	516.03	0.0307	0.3966	11.631	3.4893
2.4	519.52	0.0315	0.4281	12.554	3.7662
2.1	523.29	0.0326	0.4607	13.5091	4.0527
1.8	527.34	0.0338	0.4945	14.501	4.3504
1.5	531.69	0.0352	0.5297	15.533	4.6599
1.2	536.35	0.0361	0.5658	16.592	4.9777
0.9	541.33	0.0372	0.6030	17.685	5.3054
0.6	546.64	0.0384	0.6414	18.809	5.6428
0.3	552.28	0.0403	0.6817	19.992	5.9975
0	558.28	0.0419	0.7236	21.218	3.1828

$$T_B = 561.5^{\circ}K$$

Table F-2.   Reservoir Temperature Versus T_B

Run No. 3 $T_R = 600^{\circ}K$

x	T_x	ΔQ_x	Q_x	T'_x	ΔT_x
4.8	600.00	-	0.384	11.26	1.689
4.5	601.69	0.0601	0.4441	13.02	3.9067
4.2	605.59	0.0620	0.5061	14.842	4.4526
3.9	610.04	0.0639	0.5701	16.718	5.0153
3.6	615.06	0.0661	0.6362	18.657	5.5970
3.3	620.66	0.0685	0.7047	20.66	5.5970
3.0	626.86	0.718	0.7765	22.77	6.8314
2.7	633.69	0.0703	0.8468	24.83	7.4496
2.4	641.14	0.0737	0.9205	26.99	8.0985
2.1	649.24	0.0776	0.9981	29.27	8.7806
1.8	658.02	0.0791	1.0772	31.59	9.4768
1.5	667.49	0.0814	1.1586	33.98	10.1930
1.2	677.68	0.0900	1.2492	36.63	10.990
0.9	688.67	0.0968	1.3459	39.47	11.841
0.6	700.51	0.1044	1.4503	42.532	12.759
0.3	713.269	0.1121	1.5624	45.819	13.746
0	727.01	0.1221	1.6845	49.399	7.409

$T_B = 734.4^{\circ}K$

Run No. 4 $T_R = 639^{\circ}K$

x	T_x	ΔQ_x	Q_x	T'_x	ΔT_x
4.8	639.00	-	0.4960	14.55	2.1818
4.5	641.18	0.0783	0.5743	16.843	5.0529
4.2	646.23	0.0799	0.6543	19.1867	5.7560
3.9	651.99	0.0832	0.7375	21.6285	6.4886
3.6	658.48	0.0865	0.8239	24.164	7.2492
3.3	665.73	0.0898	0.9137	26.794	8.0381
3.0	673.768	0.0947	1.0084	29.571	8.8712
2.7	682.639	0.0937	1.1021	32.3195	9.6959
2.4	692.335	0.0991	1.2012	35.225	10.5675
2.1	702.902	0.1052	1.3064	38.3113	11.4934
1.8	714.395	0.1129	1.4193	41.6215	12.4865
1.5	726.881	0.1213	1.5406	45.1801	13.554
1.2	740.435	0.1306	1.6711	49.008	14.702
0.9	755.40	0.1413	1.8124	53.149	15.945
0.6	771.34	0.1536	1.9660	57.654	17.296
0.3	788.636	0.1674	2.1330	62.564	18.769
0	807.41	0.1859	2.3190	68.006	10.201

$T_B = 817.6^{\circ}K$

APPENDIX G

CALCULATION OF THERMAL CHARACTERISTICS
OF COLLECTOR-RADIATOR STRUCTURE

APPENDIX G

CALCULATION OF THERMAL CHARACTERISTICS OF
COLLECTOR-RADIATOR STRUCTURE

1. INTRODUCTION

This appendix contains the specific heat calculations for the collector-radiator structure and the cesium reservoir subassembly. Also presented are warm up computations for the collector-radiator structure as a function of heat input. The tabular results of the warm up calculations contained in this appendix are discussed and presented graphically in Section 8.4.5 (Volume III).

2. NOMENCLATURE

The symbols employed in this appendix are defined below:

$$C \quad = \text{Radiative power, watts/}^\circ\text{K}$$

$$Q \quad = \text{Generator at transfer, watts}$$

$$Q_{CR} \quad = \text{Heat transferred to collector-radiator structure, watts}$$

$$T \quad = \text{General temperature, }^\circ\text{K}$$

$$T_S \quad = \text{Steady state value of temperature, }^\circ\text{K}$$

$$t \quad = \text{Time, seconds}$$

$$m \quad = \text{Mass, gm-sec}^2\text{/cm}$$

$$c_p \quad = \text{Specific heat, cal/gm-}^\circ\text{C}$$

$$u \quad = T/T_S$$

$$v \quad = \text{Tan}^{-1}u$$

$$x \quad = (1 + u)/(1 - u)$$

$$y \quad = 1/2\, \ell n\, x$$

$$\tau \quad = m\, c_p\, T_S/Q, \text{ seconds.}$$

3. CALCULATIONS

The thermal response of the collector-radiator structure at constant heat input is given by:

$$m c_p \frac{dT}{dt} = Q - CT^4 \tag{1}$$

$$m c_p \left[\frac{dT}{2\sqrt{QC}\left(\sqrt{\frac{Q}{C}} + T^2\right)} + \frac{dT}{2\sqrt{QC}\left(\sqrt{\frac{Q}{C}} - T^2\right)} \right] = dt$$

$$\int dt = \frac{m c_p}{2 QC} \sqrt[4]{\frac{C}{Q}} \left[\tan^{-1} T \sqrt[4]{\frac{C}{Q}} + \frac{1}{2} \ln \left(\frac{\sqrt[4]{\frac{Q}{C}} + T}{\sqrt[4]{\frac{Q}{C}} - T} \right) \right] \tag{2}$$

At steady state $Q = CT_S^4$. Therefore

$$\frac{Q}{C} = T_S^4 . \tag{3}$$

Substituting this value of Q/C into Equation 2 and simplifying yields

$$\int dt = \frac{m c_p T_S}{2 Q} \left[\tan^{-1} \frac{T}{T_S} + \frac{1}{2} \ln \left(\frac{T_S + T}{T_S - T} \right) \right] . \tag{4}$$

The heat capacity of the converter parts and subassemblies are summarized in Table G-1. Equation 4 was used to compute the thermal response of the collector-radiator structure and the results are presented in Table G-2.

G-2

Table G-1. Heat Capacity of Converter Parts and Subassemblies

Part No.	Description	Material	Specific Heat (cal/gm°C)	Weight (gm)	Heat Capacity (cal/°C)	Heat Capacity (joules/°C)
1	Cavity Piece	Ta	0.036	38.901	1.4004	5.8621
2	Emitter	Re	0.035	1.1634	0.04072	1.7037
3	Collector	Mo	0.065	110.647	7.1921	30.1061
4	Emitter Support	Ta	0.036	1.3844	0.06368	0.2666
5	Intermediate Support	Nb	0.065	0.7837	0.0509	0.21307
6	Outer Seal Flange	Nb	0.065	25.943	1.6863	7.0589
7	Seal	Al_2O_3	0.18	2.8016	0.50429	2.1106
8	Inner Seal Flange	Nb	0.065	0.9238	0.06005	0.25158
9	Cesium Tube	Ni	0.12	3.8070	0.45684	1.9122
10	Cesium Reservoir	Cu	0.096	4.4378	0.42603	1.7832
11	Radiator Fins	Cu	0.096	66.6	6.3936	26.7636
12	Cesium Reservoir Ring	Ni	0.12	1.9865	0.23838	0.9979
13	Cesium Reservoir Heater	Ni(Ass.)	0.12	0.72	0.0864	0.3625
14	Terminal Post	Nb	0.065	3.2847	0.2135	0.8937
15	Lead Clamp	Nb	0.065	7.5992	0.4939	2.0724
16	Lead Connector	Cu	0.096	4.4190	0.4242	1.7757
17	Stranded Lead	Cu	0.096	23.664	2.2717	9.5093
18	Emitter Terminal Screw	Ti	0.1125	0.8190	0.0921	0.3855
19	Emitter Terminal Nut	SS	0.12	1.1804	0.14165	0.5927
20	Collector Terminal	SS	0.12	4.0471	0.48565	2.0327
21	Collector Terminal Screw	SS	0.12	0.8749	0.10499	0.4391
22	Collector Terminal Nut	SS	0.12	1.1804	0.14165	0.5927
Emitter Subassembly (Parts 1, 2, 4)		-	-	-	1.5048	6.2991
Collector Radiator Subassembly (Parts 3, 5-9, 11, 14-22)		-	-	-	20.713	86.71
Cesium Reservoir Subassembly		-	-	-	0.7508	3.143

Table G-2. Thermal Response of Collector-Radiator Structure (mc_p = 86.71 joules/$^\circ$C)

T	u	v	x	y	v_{300}	y_{300}	t
Run No. 1	Q_{CR} = 50 Watts		$T_S = 660^\circ$K		τ = 572.3 Seconds		
400	0.6060	0.54095	4.0761	0.70182	0.4267	0.48916	187.08
500	0.7575	0.6457	7.2474	0.98981	0.4267	0.48916	411.85
600	0.9090	0.7329	20.978	1.51987	0.4267	0.48916	765.10
700	1.0606	0.8027	3.4003	1.76318	0.4267	0.48916	–
800	1.2121	0.8725	10.429	1.15139	0.4267	0.48916	–
Run No. 2	Q_{CR} = 70 Watts		$T_S = 710^\circ$K		τ = 439.7 Seconds		
00	0.5634	0.5061	1.2754	0.6377	0.3997	0.42711	139.39
500	0.7042	0.6108	1.7509	0.8755	0.3997	0.42711	290.00
600	0.8451	0.6980	2.4765	1.2382	0.3997	0.42711	487.84
700	0.9859	0.7678	4.9473	2.4736	0.3997	0.42711	1061.79
Run No. 3	Q_{CR} = 90 Watts		$T_S = 755^\circ$K		τ = 363.7 Seconds		
400	0.5298	0.4872	–	0.5893	0.37816	0.42035	101.1
500	0.6623	0.5849	–	0.7966	0.37816	0.42035	212.03
600	0.7947	0.6714	–	1.0839	0.37816	0.42035	347.98
00	0.9272	0.7479	–	1.6366	0.37816	0.42035	576.8
Run No. 4	Q_{CR} = 110 Watts		$T_S = 800^\circ$K		τ = 315.3 Seconds		
400	0.500	0.4637	–	0.54930	0.35897	0.39423	81.92
500	0.6250	0.5588	–	0.73278	0.35897	0.39423	169.76
600	0.7500	0.6434	–	0.97295	0.35897	0.39423	272.16
700	0.875	0.71907	–	1.35402	0.35897	0.39423	416.17
Run No. 5	Q_{CR} = 130 Watts		$T_S = 845^\circ$K		τ = 281.8 Seconds		
400	0.4734	0.4422	–	0.51302	0.3412	0.37097	68.49
500	0.5917	0.5344	–	0.67820	0.3412	0.37097	141.03
00	0.7101	0.6176	–	0.88663	0.3412	0.37097	223.21
00	0.8284	0.6917	–	1.18277	0.3412	0.37097	327.55
800	0.9467	0.7581	–	1.79728	0.3412	0.37097	519.44

APPENDIX H

THERMAL RESPONSE OF CESIUM
RESERVOIR

APPENDIX H

THERMAL RESPONSE OF CESIUM RESERVOIR

1. INTRODUCTION

This appendix contains the cesium reservoir thermal response calculations. The results tabulated in this appendix are discussed and presented graphically in Section 8.4.6 (Volume III).

2. NOMENCLATURE

The symbols used in this appendix are defined below.

Q_R = Heat transferred to cesium reservoir, watts

T = General temperature, $^{\circ}K$

T_S = Steady state value of temperature, $^{\circ}K$

c_p = Specific heat, cal/gm- $^{\circ}C$

m = gm-sec^2/cm

t = Time, seconds

u = T/T_S

v = $\tan^{-1} u$

x = $(1 + u)/(1-u)$

y = $1/2 \, \ln$

τ = $m \, c_p \, T_S/Q$, seconds

CALCULATIONS

The thermal response calculations for the cesium reservoir are summarized in Table H-1. The calculations were performed in the same manner as those outlined in Appendix G, using the basic thermal response equation developed in that appendix.

Table H-1. Thermal Response of Cesium Reservoir

$(mc_p = 4.100 \text{ joules}/^\circ C)$

T	u	v	x	y	v_{300}	y_{300}	t
Run No. 1 $Q_R = 0.5$ w $\quad T_S = 620^\circ K \quad \tau = 2541$ seconds							
350	0.5645	0.5140	3.5924	0.63907	0.4506	0.52715	445.55
400	0.6451	0.5731	4.635	0.76628	0.4506	0.52715	919.03
500	0.8333	0.6946	10.998	1.19438	0.4506	0.52715	2315.8
600	0.9677	0.7691	60.92	2.05461	0.4506	0.52715	4691.3
620	1.000	0.7854	-	-	-	-	-
Run No. 2 $Q_R = 1.0$ w $\quad T_S = 762^\circ K \quad \tau = 1561$ seconds							
350	0.4593	0.4305	2.6989	0.49477	0.3749	0.41645	209.14
400	0.5243	0.4829	3.2043	0.58157	0.3749	0.41645	426.54
500	0.6562	0.5806	4.8173	0.78638	0.3749	0.41645	898.97
600	0.7874	0.6670	8.4073	1.06471	0.3749	0.41645	1468.58
620	0.8136	0.6830	9.7296	1.13765	0.3749	0.41645	1607.48
Run No. 3 $Q_R = 2.0$ w $\quad T_S = 906^\circ K \quad \tau = 928.4$ seconds							
400	0.4415	0.4157	2.581	0.47389	0.3197	0.34403	209.69
500	0.5519	0.5041	3.4633	0.62063	0.3197	0.34403	428.00
600	0.6623	0.5849	4.9224	0.79665	0.3197	0.34403	666.44
620	0.6843	0.6001	5.335	0.83761	0.3197	0.34403	718.58
Run No. 4 $Q_R = 4.0$ w $\quad T_S = 1078^\circ K \quad \tau = 552.3$ seconds							
400	0.3711	0.35547	2.1802	0.38966	0.2714	0.28549	103.97
500	0.4638	0.4343	2.7299	0.50215	0.2714	0.28549	209.65
600	0.5566	0.5079	3.5106	0.62781	0.2714	0.28549	319.71
620	0.5751	0.5219	3.7069	0.65551	0.2714	0.28549	342.74
Run No. 5 $Q_R = 8.0$ w $\quad T_S = 1282^\circ K \quad \tau = 328.4$ seconds							
400	0.3120	0.3025	1.9069	0.32355	0.22980	0.23812	51.93
500	0.3900	0.3721	2.2787	0.41209	0.22980	0.23812	103.87
600	0.4680	0.43778	2.7594	0.50761	0.22980	0.23812	156.82
620	0.4836	0.45029	2.8729	0.52715	0.22980	0.23812	167.34
Run No. 6 $Q_R = 16.0$ w $\quad T_S = 1524^\circ K \quad \tau = 195.2$ seconds							
400	0.2625	0.25686	1.7119	0.26824	0.1943	0.19939	25.65
500	0.3281	0.31707	1.9766	0.34155	0.1943	0.19939	51.72
600	0.3937	0.37496	2.2987	0.41427	0.1943	0.19939	77.21
620	0.4068	0.3863	2.3715	0.43144	0.1943	0.19939	82.78

APPENDIX I

CONVERTER WARM-UP CALCULATIONS

APPENDIX I
CONVERTER WARM-UP CALCULATIONS

1. INTRODUCTION

This appendix contains the thermionic converter warm up calculations. The results of these calculations are discussed and presented graphically in Section 8.4.7 (Volume III).

2. NOMENCLATURE

The symbols used in this appendix are defined below:

E = Energy entering the generator cavity, watts

t = Time, seconds

I_o = Converter output current, amperes

Q_{CR} = Heat transferred to the collector-radiator structure, watts

T_B = Temperature at base of collector, $^{\circ}K$

T_R = Cesium reservoir temperature, $^{\circ}K$

Q_R = Heat transferred to cesium reservoir, watts.

3. CALCULATIONS

The converter warm up calculations are summarized in Table I-1 and I-2.

Table I-3 presents the experimental data taken on Converter VIII-S-2. These measurements were made to determine thermionic converter output current as a function of cesium reservoir temperature for a constant output voltage of 0.85. This data was used in performing the converter warm-up calculations.

Table I-1. Calculation of Converter Warm Up

Case I. Full Power Input (E = 1412 watts)

a. No Reservoir Heating

t	I_o	Q_{CR}	T_B	T_R
100	0	95	405	384
200	0	95	505	460
300	0	95	585	516
400	0.2	95	650	556
500	2.5	96.5	710	588
600	12.7	103	742	604
700	22.5	110	783	624
800	35.5	121	816	638
900	42.3	126	835	646
1000	40.8	125	835	646

b. With Reservoir Heating $Q_R = 4.0$ watts

t	I_o	Q_{CR}	T_B	T_R
50	0	95	355	348
100	0	95	405	396
150	0	95	455	444
200	0	95	505	490
250	0	95	545	538
300	1.0	96	585	582
350	9.5	101	630	604
400	35.5	119	720	594
500	16.0	105	730	595
600	16.8	106	750	620
700	33.0	118.5	830	644
800	41.5	125	835	644
900	41.5	125	835	644
1000	41.5	125	835	644

Table I-1. Calculation of Converter Warm Up (Cont)

Case I. Full Power Input (E = 1412 watts)

c. With Reservoir Heating Q_R = 2.0 watts

t	I_0	Q_{CR}	T_B	T_R
50	0	95	355	324
100	0	95	405	348
150	0	95	455	372
200	0	95	500	395
250	0	95	545	418
300	0	95	585	442
350	0	95	620	464
400	0	95	650	486
450	0	95	675	525
500	0.5	95.6	695	532
550	0.75	95.6	715	553
600	2.2	96.5	725	574
650	6.0	98.8	745	594
700	16.0	105	765	635
800	42.0	126	830	644
900	41.5	126	835	646
1000	41.0	125	835	646

Table I-2. Calculation Of Converter Warm Up

Case II. Flux Controlled to Maintain $T_E = 2000\,^{\circ}K$

a.   No Reservoir Heating

t	I_o	Q_{RC}	T_B	T_R
100	0	59	365	352
200	0	59	425	400
300	0	59	482	444
400	0	59	530	478
500	0	59	565	502
600	0	59	595	522
700	0.4	59.8	620	534
800	0.9	60	640	550
900	2.0	62	660	562
1000	2.5	63	675	570

b.   With Reservoir Heating $Q_R = 2.0$ watts

t	I_o	Q_{RC}	T_B	T_R
50	0	95	355	324
100	0	95	405	348
150	0	95	455	372
200	0	95	505	395
250	0	95	545	418
300	0	95	585	442
350	0	95	615	464
400	0	95	650	487
450	0	95	675	510
500	0	95	695	532
550	0.8	95.6	715	553
600	2.2	96.5	725	574
650	6.0	98.8	745	594
700	16.0	105	767	613
800	28.0	114	805	634
900	41.5	125	835	646
1000	40.8	125	835	646

Table I-3. (Sheet 1 of 2)

THERMO ELECTRON
ENGINEERING CORPORATION

CONVERTER NO. VIII-S-2   RUN NO. 2 (.85 VOLT DATA)   DATE 1-20-65

	1	2	3	4	5	6	7	8	9	10
TIME STARTED 12:45	0.3	0.6	0.75	0.85	0.95	1.1	1.2	1.3	1.4	1.5
T_o (PYROMETER) °C	1452	1440	1698	1700	1698	1698	1700	1700	1704	1702
T_{ES} (EMITTER) °K										
V_o (OUTPUT VOLTS)	~.8	.85	.85	.85	.85	.85	.85	.85	.85	.85
I_o (OUTPUT AMPS.)	0	.1	.1	.2	.4	.5	1.0	1.7	2.9	4.0
P_o (OUTPUT WATTS)										
T_R mV	5.34	7.90	8.56	8.98	9.33	9.54	10.16	10.65	11.04	11.32
(RESERVOIR TEMP.) °C	130	194	211	221	230	235	250	262	271	278
T_C mV	12.45	14.53	17.23	17.8	18.12	18.2	18.47	18.79	19.25	19.62
(COLLECTOR TEMP.) °C	305	357	421	435	440	443	449	457	467	476
T_F mV										
(RADIATOR FIN TEMP.) °C										
T_S mV	—	—	19.9	20.2	20.4	20.44	20.63	20.85	21.3	21.5
(SEAL TEMP.) °C										
E_b (BOMB. VOLTS)	1010	1010	993	993	993	992	991	990	989	988
I_b (BOMB. mA)	104	104	187	187	188	189	193	195	201	204
P_b (BOMB. WATTS)										
E_F (FIL. VOLTS)	4.6	4.6	4.8	4.8	4.8	4.8	4.8	4.8	4.8	4.8
I_F (FIL. AMPS.)	28.5	28.5	29	29.5	29.2	29.3	29.3	29.5	29.6	29.8
E_C (COL. HEATER VOLTS)	0	0	0	0	0	0	0	0	0	0
I_C (COL. HEATER AMPS.)	0	0	0	0	0	0	0	0	0	0
E_R (RES. HEATER VOLTS)	0	0	0	0	0	0	—	—	—	—
I_R (RES. HEATER AMPS.)	0	0	0	0	0	0	~.1	~.2	~.3	~.3
VACUUM 10^{-6} mm Hg	32	10	6	8	7	4	4	4	3.8	3.6
F. Marino										
OBSERVER P. Bros										

NOTES: VOLTAGE TAPS ON SEAL FLANGE ON TAB OPPOSITE EMITTER LEAD, AND ON RADIATOR

Table I-3.   (Sheet 2 of 2)

THERMO ELECTRON
ENGINEERING CORPORATION

SHEET __4__

CONVERTER NO. VIII - S - 2   RUN NO. 2 (CONT.)   DATE 1-20-65

	1	2	3	4	5	6	7	8	9	10
TIME	1.6	1.7	1.8	1.9	2.0	2.1	2.2	2.3	2.4	2.7
T_o (PYROMETER) °C	1700	1700	1702	1698	1700	1700	1701	1700	1703	1703
T_{ES} (EMITTER) °K										
V_o (OUTPUT VOLTS)	.85	.85	.85	.85	.85	.85	.85	.85	.85	.85
I_o (OUTPUT AMPS.)	4.8	6.2	8.7	11.2	17.8	23.2	26.4	26.8	24.0	21.2
P_o (OUTPUT WATTS)										
T_R mV	11.45	11.74	12.04	12.33	12.93	13.35	13.70	14.13	14.36	14.42
(RESERVOIR TEMP.) °C	282	288	295	302	317	327	336	346	352	353
T_C mV	19.87	20.32	20.85	21.35	22.67	23.83	24.70	25.05	24.85	28.9
(COLLECTOR TEMP.) °C	482	492	505	517	547	574	595	603	598	694
T_F mV										
(RADIATOR FIN TEMP.) °C										
T_S mV	21.67	22.0	22.33	22.63	23.45	24.18	24.75	25.0	24.9	27.55
(SEAL TEMP.) °C										
E_b (BOMB. VOLTS)	988	987	986	984	982	980	978	978	978	979
I_b (BOMB. mA)	205	211	221	226	251	267	279	282	277	268
P_b (BOMB. WATTS)										
E_F (FIL. VOLTS)	4.8	4.9	4.9	4.9	5.0	5.1	5.1	5.1	5.1	5.0
I_F (FIL. AMPS.)	29.8	29.9	30.0	30.0	30.5	30.7	30.9	30.9	30.9	30.6
E_C (COL. HEATER VOLTS)	0	0	0	0	0	0	0	0	0	15
I_C (COL. HEATER AMPS.)	0	0	0	0	0	0	0	0	0	8
E_R (RES. HEATER VOLTS)	—	—	—	—	—	—	—	—	—	—
I_R (RES. HEATER AMPS.)	~.3	~.3	~.4	~.5	~.5	~.5	~.5	~.6	~.6	~.3
VACUUM 10^{-6} mm Hg	3.4	3.7	3.3	3.3	3.4	3.5	3.5	3.8	3.3	5.3
										(1)
F. Marino										
OBSERVER P. Brown										

NOTES: (1) MICRO OPTICAL PYROMETER READING COMPARED TO L & N PYROMETER

T_{MO} = 1701 °C   1704°C 1705°
$T_{L&N}$ = 1687   1686°C
F.M.   P.B.

APPENDIX J

CALCULATION OF ENERGY
CHANGES DUE TO MISORIENTATION

APPENDIX J

CALCULATION OF ENERGY CHANGES DUE TO MISORIENTATION

1. INTRODUCTION

This appendix contains the results of calculations performed in determining the changes in energy available in the cavity as a result of misorientations greater than the 0.1 degree value for which the system was designed. The results summarized in this appendix are discussed in Section 8.9.2 (Volume III).

2. NOMENCLATURE

The symbols employed in this appendix are defined below:

E = Energy entering generator cavity, watts

q = Solar energy density at focal plane, watts/cm^2

r = Radial position in focal plane, cm^2

A_n = Area of ring element, n, at focal plane, cm^2

B_n^I = Angular dimension of element n in Quadrant I, degrees

E_n^I = Energy received by ring element n in Quadrant I, watts.

3. CALCULATIONS

Figure J-1 presents the nominal energy entering the generator cavity as a function of aperture radius. This curve was obtained from the results presented in Section 4.4.2 (Volume II).

Figure J-2 represents the nominal energy distribution in the focal plane as a function of aperture radius.

Figure 8-33 (Section 8.9.2 - Volume III) shows graphically the procedure which was used to determine the changes in input solar energy resulting from misorientations of 10 and 20 minutes. The focal spot produced by the concentrator was divided into four quadrants corresponding to the heated faces of the thermionic converters. The amount of area in any one focal spot ring contained within any given quadrant was determined graphically and the corresponding amount of energy falling within that quadrant computed.

The results of these calculations are summarized in Table J-I.

Table J-1.   Calculation of Solar Energy Entering Misoriented Cavity

Case I - X = .36 cm (10°)

n	(ro)n	(ri)n	A_n	β_n^I	β_n^{II}	β_n^{III}	A_n^I	A_n^{II}	A_n^{III}	q_n	E_n^I	E_n^{II}	E_n^{III}
1	0.1	0.0	0.0314	0	0	360.0	0.	0.	0.0314	1210	0	0	37.99
2	0.2	0.1	0.0942	10.8	65.0	238.0	0.0028	0.0178	0.0623	1200	3.36	74.7	74.7
3	0.3	0.2	0.1571	54.7	90.0	144.0	0.0151	0.0393	0.0628	1150	17.4	45.2	72.2
4	0.4	0.3	0.2199	51.5	90.0	126.0	0.0314	0.0547	0.0752	1050	32.9	57.4	82.1
5	0.5	0.4	0.2827	59.6	90.0	118.4	0.0468	0.0696	0.0929	730	34.2	50.8	67.8
6	0.6	0.5	0.3456	65.0	89.5	112.3	0.0624	0.0846	0.1078	460	28.7	38.9	49.6
7	0.7	0.6	0.4084	69.0	89.4	110.0	0.0742	0.1014	0.1248	310	24.2	31.4	38.7
8	0.8	0.7	0.4712	71.7	89.4	107.0	0.0935	0.1169	0.1400	190	17.8	22.2	26.6
9	0.9	0.8	0.5341	74.2	89.0	105.7	0.1101	0.1326	0.1565	100	11.0	13.3	15.7
10	1.0	0.9	0.5969	76.0	89.6	104.0	0.1260	0.1482	0.1724	50	6.3	7.4	8.62
										ΣE_n	175.86	341.3	474.01

$E_I + 2E_{II} + E_{III} = 1332.4$ watts

% decrease: $\dfrac{1510 - 1332.4}{1510} = 11.8$

Case II - X = .35 cm (20°)

n	(ro)n	(ri)n	A_n	β_n^I	β_n^{II}	β_n^{III}	A_n^I	A_n^{II}	A_n^{III}	q_n	E_n^I	E_n^{II}	E_n^{III}
1	0.1	0	0.0314	0	0	360.0	0	0	0.0311	1210	0	0	37.9
2	0.2	0.1	0.0942	0	0	360.0	0	0	0.0912	1200	0	0	113.0
3	0.3	0.2	0.1571	0	43	254.0	0	0.0195	0.1196	1150	0	21.6	137.5
4	0.4	0.3	0.2199	12.5	86	174.0	0.0076	0.0519	0.1063	1050	7.9	54.5	111.6
5	0.5	0.4	0.2827	25.0	88.2	152.0	0.0219	0.0693	0.1194	730	15.9	50.6	87.2
6	0.6	0.5	0.3456	41.0	89.0	140.0	0.0393	0.0854	0.1344	460	18.4	39.3	61.8
7	0.7	0.6	0.4084	49.4	89.0	133.0	0.0560	0.1009	0.1497	310	17.4	31.3	46.4
8	0.8	0.7	0.4712	57.0	89.0	127.0	0.0719	0.1165	0.1662	190	13.7	32.1	31.6
9	0.9	0.8	0.5341	59.0	89.0	122.0	0.0875	0.1320	0.1809	100	8.8	13.2	18.1
10	1.0	0.9	0.5969	63.0	89.0	117.5	0.1045	0.1476	0.1945	50	5.2	7.4	9.7
										ΣE_n	87.3	240.0	654.5

$E_I + 2E_{II} + E_{III} = 1222.1$ watts

% decrease: $\dfrac{1510 - 1222.1}{1510} = 19.1$

APPENDIX K

GENERATOR WEIGHT CALCULATIONS

APPENDIX K

GENERATOR WEIGHT CALCULATION

1. <u>INTRODUCTION</u>

This appendix contains the thermionic generator weight calculations for the generator design presented in Section 8.3.2 (Volume III).

2. <u>CALCULATIONS</u>

The detailed generator weight calculations are summarized in Table K-1. The total generator weight is 5.67 pounds including the generator support ring.

Table K-1. Generator Weight Prediction

Part No.	Description		Material	Density (gm/cm³)	Assumed Configuration	OD or Length (cm)	ID or Width (cm)	Height or Thickness (cm)	Volume (cm³)	Quantity and Sign	Weight (gm)
1	*Cavity Piece	a	Ta	16.6	C	3.34	0	0.224	1.963	+1	32.596
		b	Ta	16.6	C	1.74	0	0.160	0.3804	-1	6.315
	Total										36.901
2	Emitter		Re	21.0	C	1.65	0	0.025	0.0554	+1	1.1634
3	Collector	a	Mo	10.2	C	1.52	0	0.92	1.4879	+1	15.177
		b	Mo	10.2	C	1.62	0	1.10	2.2672	+1	23.125
		c	Mo	10.2	C	2.14	0	0.36	1.3668	+1	13.941
		d	Mo	10.2	C	4.08	0	0.49	6.2756	+1	64.010
		e	Mo	10.2	C	0.50	0	2.8	0.5496	-1	5.606
	Total										110.647
4	Emitter Support		Ta	16.6	C	1.65	1.64	0.80	0.0834	+1	1.3844
5	Intermediate Support		Nb	8.66	C	1.82	1.75	0.90	0.0905	+1	0.7837
6	Outer Seal Flange	a	Nb	8.66	C	1.92	1.88	0.92	0.0978	+1	0.8469
		b	Nb	8.66	C	2.44	1.88	0.15	0.2470	+1	2.1390
		c	Nb	8.86	C	2.44	2.36	0.96	0.2895	+1	2.5071
		d	Nb	8.66	C	3.44	2.36	0.24	1.1807	+1	10.225
	Total										25.643
7	Seal		Al₂O₃	3.97	C	2.36	1.78	0.36	0.7057	+1	2.8016
8	Inner Seal Flange		Nb	8.66	C	1.78	1.70	0.90	0.2327	+1	0.9234
9	Cesium Tube		Ni	8.90	C	0.50	0.42	7.40	0.4278	+1	3.8070
10	Cesium Reservoir		Cu	8.94	C	0.50	0.63	2.8	0.4964	-1	4.4378
11	Radiator Fins		Cu		see radiator analysis (b = .2, c = 4.0)						66.6
12	Cesium Reservoir Ring		Ni	8.90	C	1.26	0.90	0.30	0.2232	+1	1.9865
13	Cesium Reservoir Heater		-	.114*	-	5.0				+1	0.72
14	Terminal Post		Nb	8.66	C	0.56	0	1.54	0.3793	+1	3.2847
15	Lead Clamp		Nb	8.66	R	0.75	0.75	1.56	0.8775	+1	7.5992
16	Lead Connector		Cu	8.94	C	1.03	0.72	1.16	0.4943	+1	4.4190
17	Stranded Lead		Cu	8.94	C	0.53	0	12.0	2.647	+1	23.664
18	Emitter Terminal Screw		Ti	4.51	C	0.34	0	2.0	0.1816	+1	0.8190
19	Emitter Terminal Nut		SS	8.03	R	0.7	0.7	0.3	0.1470	+1	1.1804
20	Collector Terminal		SS	8.03	R	1.4	0.9	0.4	0.5640	+1	4.0471
21	Collector Terminal Screw		SS	8.03	C	0.34	0	1.3	0.10895	+1	0.8749
22	Collector Terminal Nut		SS	8.03	R	0.7	0.7	0.3	0.1470	+1	1.1804
23	Ceramic Standoff		Al₂O₃	3.97	C	0.36	0.25	0.40	0.0739	+1	1.1736
24			Al₂O₃		C	0.36	0.26	0.44	0.0813	+4	1.2912
25	Washer		SS	8.03	C	0.50	0.28	0.12	0.0102	+4	0.5236
26	Mounting Screw		SS	8.03	C	0.27	0	2.0	0.1145	+4	3.6776
27	Emitter Shield #1		Ta	16.6	R	5.50	0.64	0.0025	0.0085	+5	0.7307
28	Emitter Shield #2		Ta	16.6	R	6.50	0.50	0.0025	0.0130	+20	4.3360
29	Emitter Shield #3		Ta	16.6	R	8.40	0.60	0.0025	0.0126	+20	4.1832
30	Cavity Support Piece		Ta	16.6	R	19.40	1.20	0.60	0.6240	+1	10.358
31	Insulating Washer #1		ThO₂	9.69	C	0.56	0.30	0.050	0.0063	+16	0.9768
32	Insulating Washer #2		ThO₂	9.69	C	0.48	0.14	0.09	0.0149	+32	4.6262
33	Cavity Screw		Ta-W**	16.9	C	0.14	0	0.8	0.0123	+16	3.3259
34	Cavity Nut		Ta-W	16.9	R	0.34	0.34	0.12	0.0139	+16	3.7596
51	Rear Cavity Piece		Ta	16.6	R	4.0	4.0	0.050	0.8000	+1	13.280
52	Rear Cavity Shield		Ta	16.6	R	2.6	2.6	0.0025	0.0169	+20	5.6168
53	Generator Block	a	Nb	8.66	R	6.68	6.68	1.32	192.77	+1	1669.33
		b	Nb	8.66	C	6.02	0	3.32	120.96	1	1361.84
		c	Nb	8.66	C	2.54	0	0.45	2.280	-2	39.489
		d	Nb	8.66	R	2.54	2.44	0.15	2.759	4	96.6109
	Total										464.45
54	Aperture Cone	a	W	19.3	C	7.20	2.50	0.26 x .566 × 7.7803		1	150.17
	Total										
55	Shield Cone	a	Ta	16.6	C	19.6	6.00	0.050 x .566 = 11.9401		+1	129.55
	Total										129.55
56	Generator Support Ring	a	SS	8.03	C	19.1	18.4	1.28	11.43	1	91.75
		b	SS	8.03	C	19.2	15.8	0.150	12.229	+1	98.199
	Total										189.95
57	Generator Block Support		SS	8.03	C	1.27	0.98	6.2	3.0769	+4	102.00
58	Cone Screws		Ta-W	16.9	C	0.27	0	0.8	0.0458	+8	6.1922
59	Shield Screw Washer		SS	8.03	C	0.64	0.24	0.08	0.0221	+8	1.4197
60	Shield Screw		SS	8.03	C	0.27	0	0.5	0.0155	+8	2.942
61	Shield Nut		SS	8.03	R	0.34	0.34	0.16	0.0309	+8	1.9850
62	Block Cover		Nb	8.66	R	6.68	6.68	0.13	5.8009	+1	50.238
63	Block Screws		SS	8.03	C	0.27	0	1.0	0.0572	+4	1.8373
	Converter Weight (Parts 1 to 14, 27 to 30)										342.97 (15 to 22)
	Converter Lead (15 to 22)										47.784
	Converter Attachment Hardware (23 to 26, 31 to 34)										19.335
	Total										346.19
	Weight of Four Complete Converters										1384.4
	Weight of Generator Structure (51 to 63)										1190.69
	Total Generator Weight (Grams)										2575.09
	Total Generator Weight (Pounds)										5.67

Notes:

C = Cylindrical   R = Rectangular
* grams/centimeter for .052" OD sheathed heater wire
** Ta-W = Tantalloy 10% W

APPENDIX L

CONCENTRATOR BLOCKAGE AREA
CALCULATIONS

APPENDIX L

CONCENTRATOR BLOCKAGE AREA CALCULATIONS

1. INTRODUCTION

The solar concentrator blockage area is calculated in this appendix for the thermionic system configuration defined in Section 8 (Volume III). In performing the thermionic system performance calculations in Section 4 of Volume II the solar concentrator blockage area was assumed to be five percent and the calculation presented here was made in order to check the validity of this assumption.

2. CALCULATIONS

The solar concentrator blockage area is defined as

$$\text{Blockage Factor (Percent)} = \frac{\text{Blockage Area x 100}}{\text{Projected Area of Concentrator}}$$

The blockage factor is made up of the shadow area resulting from three components:
(1) the thermionic generator, (2) the generator support structure, and (3) the reflectometer head. Each of these is computed below.

The generator mounting ring, which is 7.5 inches in diameter, represents the maximum diameter of the generator structure. Therefore:

$$\text{Generator Blockage Area} = \frac{\pi \times 7.5^2}{4} = 44.2 \text{ in.}^2$$

The generator support tubes are 0.75 inch in diameter so that support structure blockage area is

$$\text{Support Structure Blockage Area} = \frac{(50-7.5)}{2} \times 3 \times 0.75 = 47.8 \text{ in.}^2$$

L-1

The reflectometer head would be approximately one inch in diameter and extend two inches beyond the generator support ring radius. The resulting blockage area then is

$$\text{Reflectometer Head Blockage Area} = 1 \times 2 = 2 \text{ in.}^2$$

The total projected area of the solar concentrator is

$$\text{Projected Area of Solar Concentrator} = \frac{\pi \times 50^2}{4} = 1960 \text{ in.}^2$$

Using the preceding numerical values the solar concentrator blockage factor can now be computed.

$$\text{Blockage Factor} = \frac{(44.2 + 47.8 + 2)\,100}{1960} = 4.8\%$$

Obviously the initial assumption was a valid one.

L-2

APPENDIX M

STADAN COMMAND
SYSTEM

APPENDIX M

STADAN COMMAND SYSTEM

1. INTRODUCTION

It is often necessary to communicate from the ground to a space vehicle to activate certain functions within the payload. For this purpose a satellite command receiver, directed by a properly coded signal from the ground, is used. A typical function would be to command the playback of a magnetic recorder as the satellite passes over an appropriate receiving station.

It has not been possible for NASA to obtain an internationally clear exclusive RF channel allocation for transmitting commands to satellites. There are frequency assignments to other services in other countries throughout the world, using both AM and FM, which fall in the same channels or in channels immediately adjacent to those used for satellite command. Thus any satellite command system must be designed to provide immunity to false command by the transmissions of these other services.

Furthermore, the RF spectrum in the 100 to 500 megacycle band is so very congested that it is not possible to obtain more than a few U.S. channel assignments for satellite command transmission in that band. Consequently, many satellites must be commanded on the same RF carrier - possibly two or three almost simultaneously from the same ground station. This necessitates that each satellite have a unique command address so that it will be immune to commands intended for other satellites.

The extent to which a satellite project should provide protection against false commands will depend upon the weight and power available for the command system, the complexity of the command functions, and the damage which could be produced by a false command. Any satellite which can be irreparably damaged by a false command should certainly have a secure command system.

In general there are two types of satellite commands. The first is a simple on-off command, causing a relay to close, a switch to be thrown, a stepping relay to advance, etc. Most satellite commands are of this simple on-off type.

The second type of command imparts actual data to the satellite, containing instructions such as desired pointing position, time schedule for future performance of requested tasks, mode of operation, etc. Complex satellites such as Nimbus, OAO, and OGO have command systems of this second type.

Both types of command systems are discussed in more detail in the following sections.

2. OPERATIONAL DESCRIPTION OF STADAN COMMAND SYSTEMS

2.1 ON-OFF COMMAND SYSTEMS

2.1.1 Simple Tone Systems

The early NASA satellites employed elementary tone-actuated command systems. The Vanguard satellite required a single tone modulation of the command carrier and later satellite command systems utilized as many as seven tones. All of the satellites using these simple tone systems have been commanded repeatedly by interfering transmissions originating in all parts of the world. The immunity of these simple tone command systems to false command by extraneous signals is very poor.

Furthermore, the simple tone system requires unique tones in order to prevent accidental command by a transmission intended for another satellite. Because of the limited RF spectrum available for command transmissions, it is not possible to assign unique tones to each satellite and thereby provide protection against accidental command.

Because of the susceptibility of interfering signals and accidental command, simple tone command systems are no longer recommended for any satellite.

M-2

2.1.2 Tone-Digital System

In order to provide high rejection of unwanted signals, a larger number of commands, a greater number of unique addresses for different satellites, and reliable reception of the correct command, a tone-digital command system for on-off commands has been developed by GSFC.

Basically this system utilizes a four-state signal (sync, 1, 0, blank), pulse-duration modulated (PDM), with constant bit-ratio coding and repetitive word formating. A series of five words (each consisting of eight bits), together with one synchronization signal and one blank period, is sent for each command. The series generally consists of a unique address word sent twice followed by an execute word sent three times. The receipt of one correct address word and one valid execute word in the same series of five words is sufficient to effect a command. This redundancy increases the probability of receiving the correct command when the signal is weak or when interference is present.

The technique used for error detection and rejection of interfering signals consists of making the code words from a known number of zeros and ones. The address command word consists of a combination of two one's and six zeros, or of six ones and two zeros. The execute command word always contains a combination of four ones and four zeros. This fixed four-out-of-eight bit coding provides a means of detecting all odd bit errors and 43 percent of all two-bit errors. To further decrease the possibility of spurious commanding, no address or execute word may be decoded unless a sync pulse has been detected, and once the address has been detected, a valid execute word must be read within the time duration of the five-word series or it will not be detected.

In a typical tone-digital command message, the coded PDM command amplitude-modulates an audio subcarrier (tone). The coding system described above provides 56 unique address command words, thus permitting 56 satellites to use the same tone:

$$2C_2^8 = 2 \, \frac{8}{2! \, 6!} = 56 \tag{1}$$

Thirty tones are available for use in this system, lying in the band from 1,025 to 11,024 cycles per second. Therefore, the total number of satellites which can be handled with this system is 56 X 30 = 1680.

The 4 X 4 execute command word format provides 70 different commands:

$$C_4^8 = \frac{8!}{4! \, (8-4)!} = 70 \, . \tag{2}$$

Since most satellites do not require so many commands, a provision has been made in the ground station design to use six-bit words instead of the eight-bit words described above. With the six-bit words, the address command word has two ones and four zeros or four ones and two zeros, providing

$$2C_2^6 = 2 \, \frac{6!}{2! \, (6-2)!} = 30 \tag{3}$$

satellites to use the same tone. The six-bit execute command has three ones and three zeros. This format provides 20 commands:

$$C_3^6 = \frac{6!}{3! \, (6-3)!} = 20 \, . \tag{4}$$

The digital decoder is capable of operating at a post-detection signal-to-noise ratio of zero db. This, in itself, is a great advantage over the tone system which requires a 20 to 30-db signal-to-noise ratio.

The NASA-Goddard tone-digital command system provides unique command messages for a very large number of satellites. Tests on this system have demonstrated that it has much greater immunity against interfering signals than the simple tone systems do. NASA recommends that all satellites requiring simple on-off type commands use the Goddard tone-digital command system. The command consoles at the STADAN sites are designed to generate the tone-digital command message.

2.1.3 Address-Execute Tone System

Although the simple tone system discussed in Section 2.1.1 has the disadvantage of being very susceptible to false command, it has the advantage of being a simple system for satellites requiring seven commands or less. There are some satellites which are extremely limited in weight and size and which require only a few commands. If such a satellite cannot be harmed by false commands, then consideration of a tone command system may be reasonable.

Operationally, however, it is not desirable to allow the satellite to be repeatedly commanded by many non-NASA transmitters, because it greatly increases the probability of failure in the command switching system and creates operations control problems. Some measure of security must be provided to prevent frequent false commanding, including accidental commands by a transmission intended for another satellite.

The Address-Execute Tone System provides protection against accidental command by a NASA station and some immunity against extraneous false commands. The 15 satellite address tones allocated provide a capacity for handling 15 satellites. Seven execute tones have been allocated. Considering these factors, this system is better than the simple tone system, but is still inferior to the tone-digital system.

All spacecraft command decoders utilize common execute tones; however, different address tones are required to avoid interference. Sequential transmission is employed with the address tone sent first to "arm" the decoder. The execute tones follow to accomplish the particular command function and may consist of up to three tones in sequence. The three sequential tones will provide 35 commands:

$$C_3^7 = \frac{7!}{3!\,(7-3)!} = 35 \,. \tag{5}$$

M-5

● The command decoder in the satellite requires the tones to be present for a minimum length of time (0.5 seconds or more) before it registers the command, and it rejects the tones which are shorter in duration.

2.2 INSTRUCTION COMMAND SYSTEMS

Many of the complex satellites such as Nimbus, OAO, and OGO require a command system which can send instructions to the satellite for real-time or future programs of operations.

● PCM is recommended by NASA for the instruction class of command systems. Since the type of data in an instruction command is very similar to that in a telemetry message, the Goddard PCM telemetry standards are applicable to instruction command systems.

Commands for future programs are stored in the satellite memory, and there is no immediate action on the satellite which can be detected at the command station to tell that
● the correct command was received. Thus it is necessary to use a command verification system and error detection coding in order to provide a reliable instruction command system. Error correcting codes may be used where command verification is not feasible.

It is recommended that any future satellite with instruction command requirements utilize the same type system as that used for either OGO or OAO.

The OGO satellite uses a 21-bit command word sent at a rate of 128 bits per second with FSK modulation. Both word sync and bit sync are inherent in the data word. The first
● bit is used for word sync; the next two bits give the address of the function system; the next eight bits are the function desired (out of a possible $2^8 = 256$); the last ten bits are the complement of the previous ten, and when inverted bit-for-bit perform the command validation.

The OAO commands are composed of two 32-bit words, and each word is accompanied by
● a transmission of its complement. The bit rate is 1000 bits per second, using FSK modulation.

M-6

Validation occurs by on-board checking of a word against its complement, and this is verified on the ground by echoing the validated word to the ground. In all but the sync commands, the first word gives information to the satellite about what to do with the second word. The first two bits are used for word sync. The third bit determines whether this is a real-time or stored command. In stored commands, bits 4 to 13 give the execution time and bits 14 to 20 give the memory location for storing both words. For both real-time and stored commands, bits 21 to 24 indicate the type of command.

2.3 NASA-GODDARD SPACE FLIGHT CENTER RECOMMENDED POLICY FOR SATELLITE COMMAND SYSTEMS

The following recommendations are made in Reference M-1:

a. All satellites requiring simple on-off type commands shall use the Goddard tone-digital command system if possible.

b. If weight problems preclude the use of the tone-digital system, and a satellite requires seven or less simple on-off type commands, then the address-execute tone system may be used.

c. The simple tone systems shall not be used.

d. PCM shall be used for the instruction class of command system, and the Goddard PCM telemetry standards are applicable.

e. Satellites with instruction command requirements should use either the OGO or the OAO type of command system.

f. Twenty-two tones ranging from 1025 to 6177 cycles per second are to be used for the address-execute tone system. The nine tones in the first octave and the six tones in the third octave are to be used as unique address tones. The seven tones in the second octave are to be used by each satellite for execute tones.

g. The tone-digital system and the instruction command system shall use tones in the 7,000 to 11,024 cycles per second band.

h. The tone frequencies, the carrier frequency, and the address tone or word shall be assigned by the Goddard Frequency Control Officer.

3. STADAN COMMAND STANDARDS

Detailed standards for both the Address-Execute Tone System and the Tone-Digital System are given in Reference M-2. Significant aspects of these standards which are not mentioned in other sections of this appendix have been abstracted for this section.

3.1 TONE COMMAND STANDARDS

The following parameters describe the tone sequence:

Tone Duration
> 0.5, 1.0, 1.5, 2.0, 2.5, 3.0, 3.5 seconds
> (duration constant throughout sequence)

Interval between tones
> 0.5 seconds

Tone Frequencies

1-7 kilocycles

Tone Sequence

Address tone plus one, two, or three execute tones.

Seven tones in the band have been allocated to the execution function, and fifteen tones to the address function. The spacecraft project may select the execute tones, the sequence of these tones, and the tone duration. The tone duration must be constant throughout the sequence. The execute tones must be registered with the GSFC Frequency Manager, who is responsible for the assignment of the RF carrier frequency and the address tone frequency.

3.2 TONE-DIGITAL COMMAND STANDARDS

This system has the capacity for 70, 8-bit execute codes and 56, 8-bit address codes. Coded pulse duration modulation (PDM) of the subcarrier is used, with 25, 50, 75 and 100 percent PDM. The subcarrier (tone) is selected from eight GSFC standard tones in the band from 7,000 to 11,024 cycles per second, and it is amplitude modulated 100 percent by the coded PDM signal. The RF carrier (148 to 150 megacycles) is then amplitude modulated 75 percent by the subcarrier. Thus the modulation format may be designated "Coded PDM/AM/AM."

A PDM pulse period is defined as 72 cycles of the encoder clock frequency. The assigned subcarrier frequency is normally used as the clock frequency. The start and end of the tone coincides with the start and end of the pulse. There are four pulse states, as follows:

Blank: Off for 1 pulse period, $72 \ T_c$

Sync: On for 3/4 pulse period, $54 \ T_c$

One: On for 1/2 pulse period, $36 \ T_c$

Zero: On for 1/4 pulse period, $18 \ T_c$

PULSE PERIOD 54 T$_c$

36 T$_c$

18 T$_c$

72 T$_c$

BLANK   Sync   1   0   0   1   1   1   0   0   1   1   0

|←— ONE WORD = 10 PULSE PERIODS = 720 T$_c$ —→|
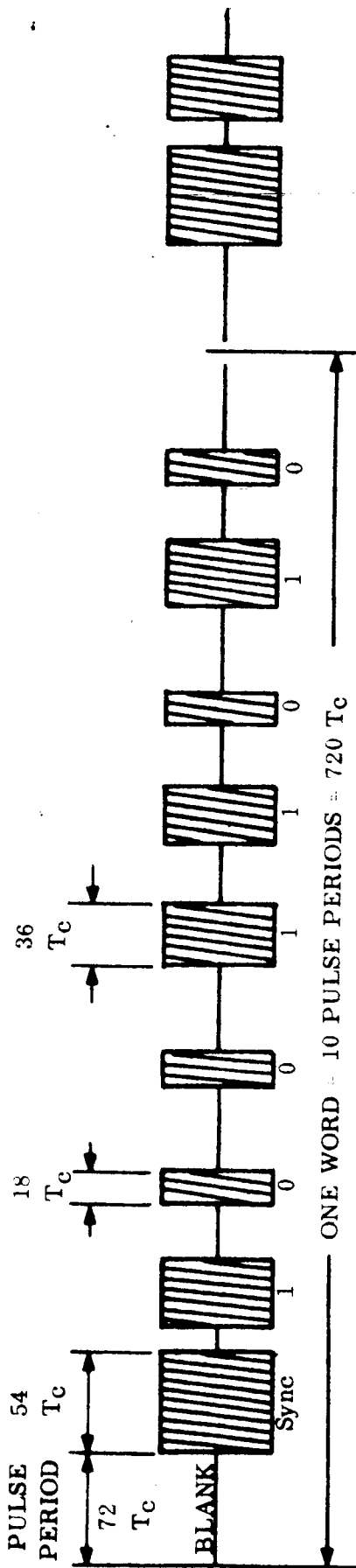
T$_c$ = PERIOD OF ENCODER CLOCK = PERIOD OF SUBCARRIER (TONE)

Figure M-1. Command Word Structure

BS 1110011	BS 1110011	BS 1001010	BS 1001010	BS 1001010	BS
6x2 ADDRESS	6x2 ADDRESS REPEATED	4x4 EXECUTE	4x4 EXECUTE REPEATED	4x4 EXECUTE REPEATED AGAIN	

|←——————— ONE FRAME = 5 WORDS + SYNC = 3744 T$_c$ ———————→|
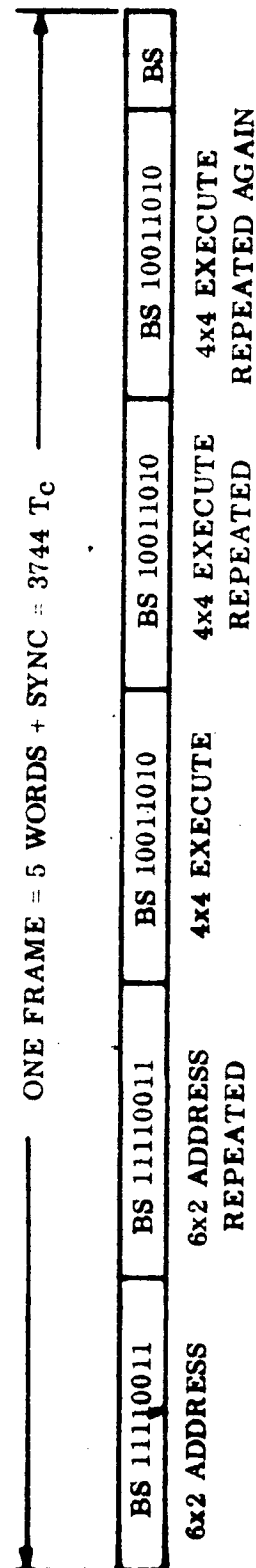
Figure M-2. Command Frame Format

A word sync pulse is inserted into each word transmitted. It will always follow a blank period (space), as shown in Figures M-1 and M-2.

Unless otherwise specified, the pulse error rate shall be less than 2×10^{-4} for a subcarrier signal-to-noise ratio of zero db. For test purposes, the noise is white (0 to 20 kilocycles) gaussian in volts rms and the subcarrier is measured in volts rms at the input to the decoder bandpass filter.

4. DESCRIPTION OF GROUND STATION TRANSMITTING EQUIPMENT

4.1 COLLINS 242G-2 VHF TRANSMITTER

The 242G transmitter is used for interrogation purposes at the ground stations. In many locations an identical unit is provided as a back-up system. The transmitter is crystal controlled and amplitude modulated, providing an output power of 200 watts over the frequency range from 108 to 152 megacycles. Special external coders are used to supply the modulating signal necessary to actuate the proper satellite command functions.

The commands are coded as explained in Section 3.2 of this appendix and are used either to modulate the transmitter carrier to produce the PDM/AM/AM mode or to key the transmitter pulses directly to produce the PDM/AM mode.

4.2 COMMAND ANTENNAS

A recent addition to the stations has been the installation of the 123 and 148 megacycle command antennas. These consist of seven-element, crossed-Yagi antennas with linear as well as left and right-hand circular polarizations available on either frequency. Polarization selection is made by insertion of precision sections of feed line (phase shifters) into the appropriate antenna feed line at the output of the hybrid. This antenna replaces the old 123-megacycle antenna which was a part of the 136-megacycle telemetry array. The gain is approximately 13 db, and the transmission line loss from the transmitter to the antenna is less than 2.5 db.

4.3 HIGH-POWER COMMAND TRANSMITTER

The high-power command transmitter system employs dual-channel, five-kilowatt General Electric Model 4BT91A1 transmitters. One transmitter operates into the antenna while the "hot standby" operates into a dummy load. Should a fault occur in the operating transmitter, the standby can be immediately placed in operation. The transmitter operates at 123 megacycles and over the band 147 to 157 megacycles, with a stability of 10^{-5} per day.

4.4 ANTENNA FOR HIGH-POWER TRANSMITTER

The high-power command antenna consists of an array of nine disk-on-rod structures composed of 14 disks each above a crossed-dipole driver. The array is mounted on a slightly modified STADAN antenna pedestal. The antenna has a gain of 22.5 db, is capable of transmitting five kilowatts of average power, and can operate over the frequency band of 120 to 155 megacycles.

5. REFERENCES

M-1.   NASA-GSFC, "Satellite Command System Recommendations for Goddard Space Flight Center", No. I-560-62-49, May, 1962.

M-2.   NASA-GSFC, "Aerospace Data Systems Standards":

   Part II, Section 1, "Tone Command Standard", 4/4/63
   Part II, Section 2, "Tone Digital Command Standard", 1/15/63.

M-12

APPENDIX N

MINITRACK TELEMETRY SYSTEM

APPENDIX N

MINITRACK TELEMETRY SYSTEM

1. INTRODUCTION

The NASA Satellite Tracking and Data Acquisition Network (STADAN) consists of three major functional systems (Reference N-1). The first, Minitrack, has been used to track all U.S. satellites containing suitable beacons (and some USSR satellites) since the beginning of the space programs in 1957 and 1958. In addition to its tracking functions, the Minitrack system has the facilities for receiving telemetry data in the 136 to 137-megacycle and 400 to 401-megacycle bands and has a planned capability for limited reception in other assigned space bands.

The second major functional system comprises the Data Acquisition Facilities (DAF). This system is equipped with multifrequency, high-gain antennas and its capability of handling large quantities of data at high rates exceeds that of the standard Minitrack telemetry systems currently in use. The first station in this network (ULASKA) has been constructed and is in operation near Fairbanks, Alaska. The second station (ROSMAN I) near Rosman, North Carolina, has been constructed and is in operation. A third station (GILMOR) near Fairbanks, Alaska, is rapidly approaching an operational status, a fourth (ROSMAN II) – an addition to the Rosman, North Carolina, site – is under construction, and a fifth station is now under construction near Canberra, Australia. Since such a wideband capability is not required for the solar thermionic mission, the DAF will not be discussed further. .

The third major system is the transportable Range and Range-Rate tracking system which complements the tracking capability of the Minitrack network by providing improved tracking data for space probes, launch vehicles, and satellites in highly elliptical orbits.

2. BRIEF DESCRIPTION OF THE MINITRACK TELEMETRY SYSTEM

Minitrack comprises an organization of fixed ground stations, located throughout the world, which provides a means of precision tracking, command, and telemetry reception

or satellites and space probes, together with a communications system to transmit this information to a computing and data processing facility. The station locations are given in Table 10-1 of this report.

A large number of the original stations were located along the 75th meridian to intercept satellite orbits with inclinations of less than 45 degrees. New stations have been located at higher latitudes to cope with more nearly polar orbits. Furthermore, the stations have been supplemented with additional antennas aligned specifically for polar orbits.

Telemetry receiving systems at 136 megacycles are available at all STADAN ground stations. In addition to this, 400-megacycle receiving systems are available at those stations having 40-foot antennas and at the DAF stations having 85-foot antennas. * Due to the limited availability of the 400-megacycle facilities, the emphasis here will be on the use of the 136-megacycle equipment.

The Minitrack Mod I Telemetry Receiver System is tunable over a frequency range of 136 to 137 megacycles. Five IF predetection bandwidths are available ranging from 10 kilocycles to 1 megacycle. Demodulation circuits are provided for AM and FM signals.

Preamplifiers having nominal 3.5 db noise figures are available at all stations. Some stations have tracking filters phase-lock demodulators, and diversity combiners.

All stations have nine-Yagi array antennas, providing a gain of about 19 db. Three stations (Johannesburg, Santiago, and Quito) have sixteen-Yagi array antennas, providing a gain of about 22 db.

*The installation of 40-foot parabolic antennas has been completed at three Minitrack stations in the southern hemisphere (Johannesburg, Santiago, and Quito).

3. DESCRIPTION OF GROUND STATION EQUIPMENT

3.1 TELEMETRY RECEIVERS

3.1.1 Minitrack Mod I Receiver

The Minitrack Mod I Telemetry Receiver System is tunable over a frequency range of 136 to 137 megacycles in one-kilocycle steps. It was designed to provide maximum accessibility and flexibility of operation. Each receiver is backed up by a duplicate.

The telemetry receiver is a triple conversion receiver with IF outputs brought out after each conversion stage. As shown in Figure N-1, the second and third IF stages each provide two selectable bandwidths, making a total of five predetection bandwidths available to permit suitable bandwidths matching the sideband construction of various signals. The predetection bandwidths are: 10, 30, 100, 300 kilocycles, and 1 megacycle. Each IF amplifier provides AM and FM detection, an IF test point, converted outputs (IF converted to a low frequency) and AGC voltage. Phase demodulation is obtainable through the use of phase-locked tracking filters in conjunction with the system, which are fed by the converted output signals.

The receiver characteristics are summarized in Table N-1.

3.1.2 Diversity Telemetry Receiver System

This solid-state receiving system is a recent addition to the STADAN and is designed to provide polarization diversity reception of satellite telemetry signals. Tunable in one-kilocycle steps, the basic receiver is capable of reception in the region from 130 to 140 megacycles simultaneously on both channels. When operated in conjunction with fixed-tuned converters, it is capable of reception in the 400 and 1700-megacycle bands as well. To permit matching to signal sideband content, six predetection bandwidths between ten kilocycles and three megacycles are selectable. The system features AM and FM
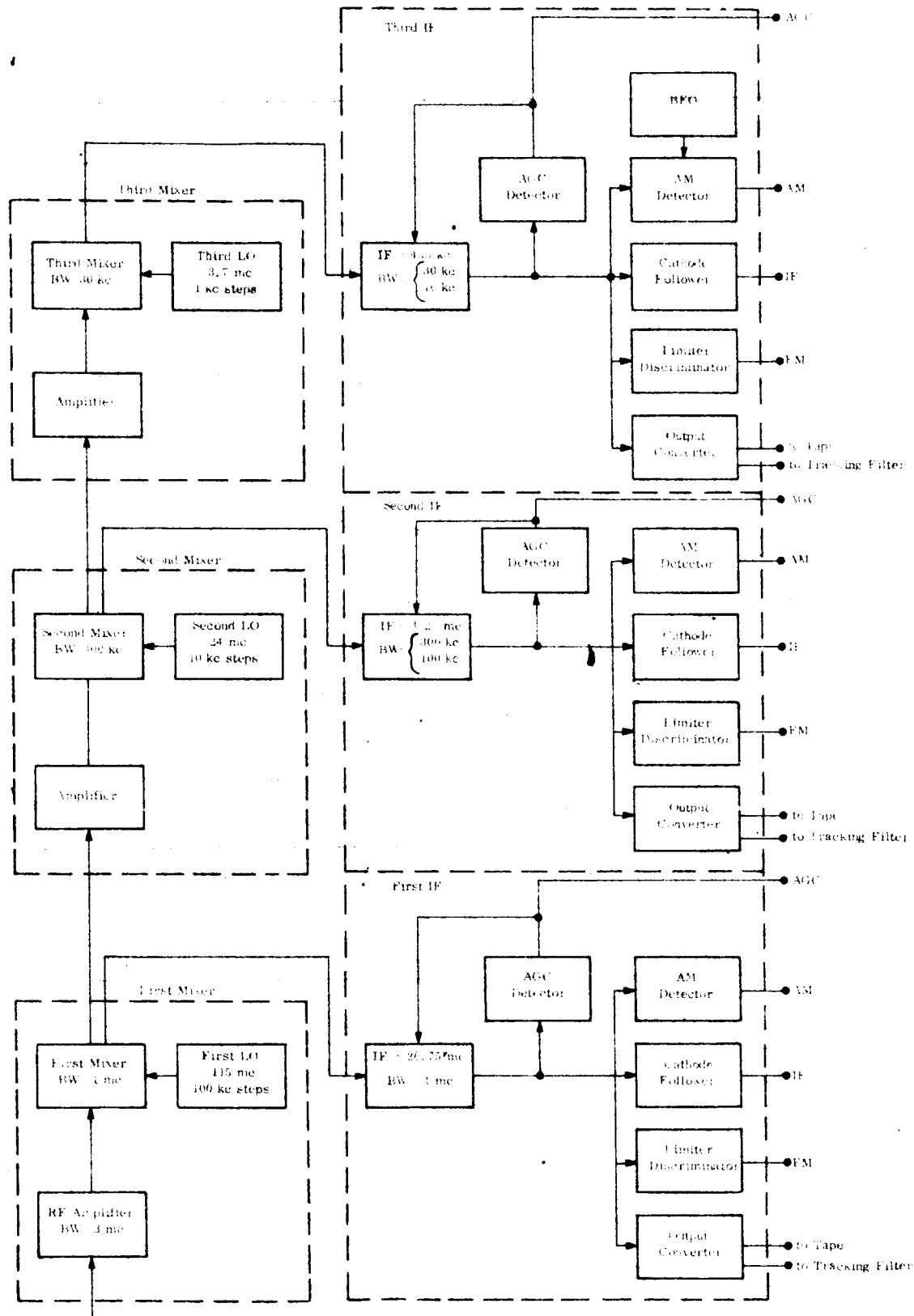
Figure N-1. Minitrack Mod 1 Telemetry Receiver

Table N-1. Minitrack Mod. I Receiver Characteristics

Receiver	Triple conversion super-heterodyne
Local oscillators	Crystal controlled
Tuning range	136-137 mc (± 740 cps)
Noise figure	Less than 3 db
Image frequency	At least 60 db
IF frequencies	Predetection bandwidths
1st 20.75 mc	1 mc
2nd 3.25 mc	300 kc or 100 kc
3rd 455.00 kc	30 kc or 10 kc
Converted signal	Bandwidth in use
555 kc	1 mc
162 kc	300 kc
62 kc	100 kc
22 kc	30 kc
12 kc	10 kc
FM detection	Limiter and Foster Seeley discriminator (all bandwidths)
AM detection	Unbalanced diode with post-detection filtering (all bandwidths)
AGC response speed	Three, 10, and 30 cps, "A" pulse (slow response): "B" pulse (fast response); manual gain control
BFO	± 30 kc
Calibration Oscillator	455 kc ± 10 cps
Calibrator attenuator	-60 dbm to -150 dbm in 5-db steps

demodulation, post-detection diversity combining, predetection output capabilities. and a visual presentation of the signal spectrum.

Table N-2 lists the characteristics of this system.

Table N-2. Diversity Solid-State Receiver System Characteristics

Tuning range	130,000 to 139.999 mc
Bandwidths	10, 30, 100, 300, kc; 1 mc, 3 mc
Noise figure	6 db (maximum)
Input impedance	50 ohms
AGC modes	Manual, automatic, combined AGC
AGS speeds	3, 30, 300 ms; 3 sec
AGC control	Output level within 1 db over dynamic range
Interchannel isolation	Greater than 70 db
Dynamic range	Thermal noise - to -25 dbm
Video outputs	1.0 v p-p at 90% AM
	1.0 v p-p at maximum FM deviation

3.2 PREAMPLIFIERS

Both vertical and horizontal polarization outputs from the data acquisition antenna are fed through notch filters into a low-noise. dual-channel preamplifier mounted at the base of the antenna tower. The purpose of the notch filters is to reject the command frequency, thereby protecting the preamplifiers from the radiated power of the satellite command transmitter. The preamplifier is encased in a pressurized box to protect it against moisture. This unit establishes the system noise figure at about 2.5 to 3.5 db. provides sufficient gain to overcome losses in the transmission lines and associated components. and provides part of the

filtering necessary for image rejection. The preamplifier characteristics are listed in Table N-3.

Table N-3. Preamplifier Characteristics

Noise Figure	3.5 db nominal
Gain	35 db
Center Frequency	136.5 mc
Bandwidth	4.3 mc ± 0.5 mc
Output Impedance	50 ohms

The horizontal and vertical outputs of the preamplifier are brought into the operations building on coaxial cables and into a polarization differentiation unit which allows simultaneous selection of four modes of polarization: horizontal, vertical, and right and left circular.

3.3 ANTENNA SYSTEM

3.3.1 Nine-Yagi Antenna - 136 Megacycles

These antennas are located at all tracking facilities. Each individual Yagi is made up of a folded half-wavelength driver above a reflector element, plus six directors to collimate the energy. The entire structure is mounted on a remotely controlled azimuth and elevation rotator system atop a 13.5-foot tower. Eight of the Yagis are used for data acquisition, and a centrally located Yagi is used to transmit command signals to the satellites. A separate feed system is used for the command antenna, and the vertical and horizontal linearly-polarized outputs of the receiving array are brought out separately. Circular polarization is accomplished by means of a polarization unit containing two cable hybrid dividers, a 90-degree phase shifter, and a hybrid adder. This unit provides two linear (horizontal and vertical) and two circular (right and left) polarization modes. Its characteristics are summarized in Table N-4.

Table N-4. Nine-Yagi Antenna Characteristics

Center frequency	136.5 mc
Frequency range	135 to 138 mc
Gain	19.2 db above isotropic
Polarization	Horizontal, vertical, right and left circular
"E" - and "H" - plane pattern	19.5 degrees at the half-power points
Sidelobes	Down 12 db or better
VSWR	Under 1.1 at 136.5 mc
	Under 2.0 at 135-139 mc
Nominal impedance	50 ohms

NOTE

The average measured gain in the linear mode is approximately 19 db.

3.3.2 Sixteen-Yagi Array - 136 Megacycles

This antenna is an array of sixteen eight-element, crossed Yagi antennas mounted 4 by 4 and a 17th Yagi centrally located which serves as a command antenna. The structure is mounted on an elevation-on-azimuth rotator atop a 15-foot tower. These systems are to be found at three of the network stations - all in the southern hemisphere (Johannesburg, Santiago, and Quito).

Circular polarization is obtained by properly combining the two complete linear feed networks. The command Yagi is identical to that used in the nine-Yagi array. Table N-5 lists the characteristics of the antenna.

Table N-5. Sixteen-Yagi Antenna Characteristics

Center frequency	136.5 mc
Frequency range	135 to 138 mc
Gain	22.4 db above isotropic
Polarization	Horizontal, vertical, right and left circular
"E" and "H" plane pattern	13 degrees
VSWR	Under 1.1 at 136.5 mc
	Under 1.5 from 135-138 mc

NOTE:

The average measured gain in the linear mode is approximately 21 db.

3.4 TRACKING FILTERS AND PHASE-LOCK DEMODULATORS

3.4.1 Interstate Mod VIII Tracking Filter

The purpose of this unit is to reduce the noise bandwidth of a noisy Doppler signal. It is essentially a bandpass filter whose center frequency is made to track the Doppler frequency automatically, supplying a virtually noise-free output signal equal in frequency to its input. Phase-lock techniques are used. The input signal is converted to a frequency of approximately 262 kilocycles by a voltage controlled oscillator (VCO), This signal is then compared in a phase detector to a crystal-controlled local oscillator having a frequency of 262 kilocycles. A d-c error signal resulting from deviations from quadrature phase relationship between the two inputs to the phase detector is filtered and fed to the VCO. This error signal serves to control the VCO frequency so that the IF is exactly equal to the

62-kilocycle local oscillator frequency. An output mixer then translates the VCO frequency back to the input signal frequency, using the reference oscillator.

Two synchronous demodulators are provided to detect amplitude and phase modulation of the Doppler signal. After detection. the AM and PM signals are fed to low-pass filters with adjustable cutoff frequencies to attenuate undesired sidebands generated in the input mixer. Table N-6 lists the characteristics of the tracking filter.

Table N-6. Tracking Filter Characteristics

Input frequency	100 cps to 120 kc (0.5 volt rms approximately)
Tracking or information bandwidth	2.5. 5. 1.0, 25, 50. and 100 cps
VCO frequency	262 to 382 kc
Doppler output	100 cps to 120 kc (1 volt rms minimum)
AM correlated detector output	0 to 2 volts rms for 30% modulation
PM correlated detector output	0.2 volts rms for 0.3 radian modulation
AM and PM detector bandwidths	1, 3. 10. 30 and 60 kc
Analog output	0 to 40 volts for 0 to 120 kc
AGC output (input signal level)	0 to -10 volts approximately

3.4.2 Electrac Model 215 Predetection, Phase-Lock Demodulator

The Electrac phase-lock demodulator provides the capability to track a space vehicle automatically and demodulate the AM and PM telemetry signals subject to Doppler shift. The input signal to the demodulator is supplied by the IF of the instrumentation receiver (3.25 mc $\pm$ 50 kc), with a signal-to-noise ratio as low as -50 db. The phase-lock loop

incorporates a third-order loop filter, coherent automatic gain control (AGC), and telemetry bandwidths up to 150 kilocycles (300-kilocycle predetection). Acquisition of the input signal can be obtained either automatically or manually.

In the automatic mode of operation, the phase-lock demodulator controls are preset to the desired parameters of AGC, demodulation bandwidth, tracking bandwidth, center frequency, and loop control. The equipment then automatically searches around the preset center frequency until a signal is acquired at which time it "locks" on and tracks the transmitter carrier. When required, the operator may manually sweep the center frequency in the automatic mode of operation.

The equipment contains a memory circuit that remembers the last known signal frequency in the event of an input signal loss. Should signal loss occur, the search phase is again inititated using the "memory" frequency as the center of frequency sweep.

The 3.25-megacycle input signal from the instrumentation receiver is fed to the input mixer, amplifier, and to two voltage-controlled attenuators. When locked, the signal heterodynes with the VCO signal to produce a 500-kilocycle IF signal. This IF signal after being attenuated, amplified, and filtered is compared with a 500-kilocycle reference signal in a phase-detector circuit. The output of the phase detector controls the VCO phase and frequency via an equalizer network. The VCO output is fed back to the input mixer completing the closed-loop circuit.

A correlated AGC voltage is generated by the correlation detector (loop-locked) having the same input signals as the loop-phase detector except that the reference signals are shifted by 90 degrees. This AGC voltage is compared with a fixed d-c reference voltage and the difference amplified and filtered. The amplified AGC signal controls the gain of the two previously mentioned voltage-controlled attenuators such that a constant level IF signal is maintained in the IF amplifiers and at the input to the phase detector. The phase-lock dynamics are thus made independent of input signal level over the operating range of the AGC system.

Wideband predetected signals from the IF driver-amplifier are made available for use by the Electrac 215C diversity combiner. This signal is also fed to the amplitude and phase demodulators. The detected AM and PM signals are then filtered and amplified for external use.

Table N-7 lists the performance characteristics of the predetection phase-lock demodulator and Table N-8 lists the available outputs.

Table N-7. Performance Characteristics of Electrac PL Demodulator

Input signal frequency range	3.25 mc $\pm$ 50 kc
Noise Bandwidth	300 kc
Signal level, including noise	70 millivolts, rms
Input impedance	50 ohms

*Bandwidth (cycles)	**Nominal Signal-to-Noise Threshold (db)	Sweep Period Automatic (seconds)	Sweep Range (cycles)
3	-41	10	100
10	-36	3	300
30	-31	1	1,000
100	-26	0.3	3,000
300	-21	0.1	10,000

Notes

*Tracking bandwidth held constant over 50-db range of input signal variations
**Signal-to-noise ratio in 300-kilocycle bandwidth for 20-degree rms maximum tracking error

Table N-8. Outputs of Electrac PL Demodulator

Doppler Frequency	3.25 mc ± 50 kc
Level	1 volt rms
Impedance	100-ohm source; load with greater than 200 ohms
Frequency Analog	D-C voltage proportional to instantaneous value of Doppler frequency output
Level	± 10 volts for ± 50 kc
Linearity	± 2 percent
Output Load	Not less than 1,000 ohms
Correlation Output	
When Locked	+ 10 volts
When Unlocked	Error beat signal (from correlation detector)
Impedance	1,000 ohms
Demodulator Output	Selectable AM or PM
Level	2.5 volts/radian for PM 5 volts p-p for 95 percent AM
Impedance	1,000 ohms
Bandwidth	Fixed lower cutoff at 3 cycles. Upper cutoff adjustable to 1.5 kc, 5 kc, 15 kc, 50 kc, or 150 kc.
Output Signal-to-Noise Ratio	Greater than 40 db for noise-free input signal
Auxiliary Outputs	Voltage controlled oscillator (250 kc to 350 kc)
	1 volt rms, 1,000 ohms Reference oscillator, 1 volt rms, 1,000 ohms AGC 5 db/volt, low impedance output
	Phone jack, low impedance output

3.5   DIVERSITY COMBINERS

3.5.1   Electrac Model 215C Diversity Combiner

The addition of the Electrac diversity combiner with two phase-lock demodulators comprises an optimum radio, predetection, polarization diversity combiner system. This overall system provides for the 500-kilocycle coherent predetection signals of the two phase-lock demodulators to be weighed and summed in the diversity combiner to produce an optimized detected signal at the demodulator output of the diversity combiner. The output signal will always be equal to or better than the stronger of the two phase-lock demodulator signals, and can be better than either signal by as much as 3 db.

Four inputs to the weighing amplifier in the diversity combiner are provided by the two telemetry receivers and the phase-lock demodulators. Each receiver supplies an AGC input which is a measure of the attenuation required (within the receiver) to maintain a constant level of signal-plus-noise to the phase-noise to the phase-lock demodulator input. Each phase-lock demodulator supplies a coherent AGC voltage which is a measure of the attenuation required to maintain a constant level of coherent 100-kilocycle carrier signal to the diversity combiner. The four AGC voltages provide the information to the weighing amplifier needed to determine the signal-to-noise ratios in each input channel.

Two voltage-controlled attenuators provide an optimum signal-to-noise ratio as well as a constant signal level to the diversity combiner IF amplifier. The signal is coherent with the diversity combiner reference oscillator and allows AM and PM demodulation by the same technique utilized in the phase-lock demodulator.

The demodulated signal at the combiner output has a signal-to-noise ratio equal to or better than the better of the two phase-lock demodulator signals. The signal components in this output are a constant for any combination of input signal-to-noise ratios within the dynamic range of the system. By summing each demodulator AGC voltage with its respective receiver AGC voltage, the difference of these summed voltages is thereby made an accurate

measure (in db) of the relative signal-to-noise ratios for the two channels under all conditions. The characteristics of the diversity combiner are listed in Table N-9.

Table N-9. Characteristics of Electrac 215C Diversity Combiner

Demodulated Output Signal	AM or PM
Signal level	2.5 volts/radian or 5 volts p-p for 95% AM (level independent of input signal-to-noise ratio)
Bandwidth	Fixed lower cutoff at 3 cps Upper cutoff adjustable to 1.5 kc, 5 kc, 15 kc, 50 kc, or 150 kc
Impedance	92 ohms
Output signal-to-noise ratio	Greater than 40 db for noise-free input signal
Auxiliary outputs	Differential AGC voltage Reference oscillator Demodulator monitors

3.5.2 TDC-1A Diversity Combiner

This unit is designed to add the video signals from two telemetry receivers, producing one video output with a signal-to-noise ratio equal to or better than the signal-to-noise ratio of the better of the two video outputs. Near optimum combining is attained through the use of a new basic circuit using beam-deflection tubes as a combiner element. This tube has the property of providing output currents that are the products of two input signal voltages. The tube contains a single cathode, control grid, screen grid, a pair of deflecting electrodes, and two plates arranged so that a voltage differential impressed across the deflection electrodes causes the beam current to be unequally divided between the two plates and proportional to the deflecting potential difference.

This circuit configuration automatically results in ratio-squared combining to realize maximum improvements in the signal-to-noise ratio of the output signal. The AGC voltages of the receivers supplying the video input signals are used to determine the proper combining ratio. The combining technique is effective when used either in conventional communications systems or in telemetry systems using any type of standard IRIG modulation. In addition, the combiner is capable of handling very rapid fading rates such as are obtained from signals originating from a tumbling, spinning spacecraft traveling at several times the speed of sound. The rapid combining rate and excellent frequency response result from the use of beam-deflection tubes as combiner elements.

3.6 PCM SIGNAL CONDITIONING CONSOLE

The PCM signal conditioning console is used to achieve bit synchronization and signal re-construction of serial PCM signals as detected by a receiver or played back from a tape recorder. The data and clock outputs from the signal conditioner may then be recorded or used for real-time display of significant spacecraft measurements by peripheral equipment. The console also contains a signal simulator and comparator for checkout and performance analysis of the signal conditioner by the operator prior to a pass. To completely close the loop on performance evaluation, the console has a single channel decommutator and error counter to enable the operator to observe any one data channel during the pass and also count the number of errors occurring in the frame sync pattern. In this manner a "figure of merit" for the received data may be obtained. Sixteen word-selection pulses are also available for peripheral equipment as well as the buffered outputs of all stages of the bit counter for external decommutation.

The characteristics of the console are listed in Table N-10.

Table N-10. Characteristics of PCM Signal Conditioning Console

Code Format	NRZ-C
	NRZ-M
	Split Phase
	RZ
Bit Rates	10 bits-per-second to 640,000 bits-per-second for RZ and NRZ
	5 bits-per-second to 320,000 bits-per-second for split phase
Input Amplitude	± 0.5 volts to ± 15 volts peak-to-peak into 1,000 ohms
Output Amplitude	12 volts peak-to-peak into 1,000 ohms
Decommutation and Display	One channel selectable by a digi-switch and displayed by a D/A converter and meter and ten binary lights
Channels	Sixteen channels selectable by a patchboard and displayed on peripheral equipment.

4. TELEMETRY STANDARDS (Reference N-3)

4.1 PULSE CODE MODULATION TELEMETRY STANDARDS

4.1.1 Code Format

A serial binary code shall be used. The following types of coding are acceptable:
(Refer to Figure N-2)

<u>Preferred</u>

NRZ   Type C
NRZ   Type M
Split Phase (Manchester code)

<u>Alternate</u>

RZ

4.1.2 <u>Bit Rate</u>

4.1.2.1 <u>Range</u> - The permissible range of bit rates is from 1 bit per second to 200,000 bits per second.

4.1.2.2 <u>Stability</u>

Long Term (one year)	$\pm$ 5 percent
Short Term (30 minutes)	$\pm$ 1/2 percent
Instantaneous (flutter)	3 percent peak to peak

Sufficient transitions must be provided to enable bit synchronization under the worst case conditions.
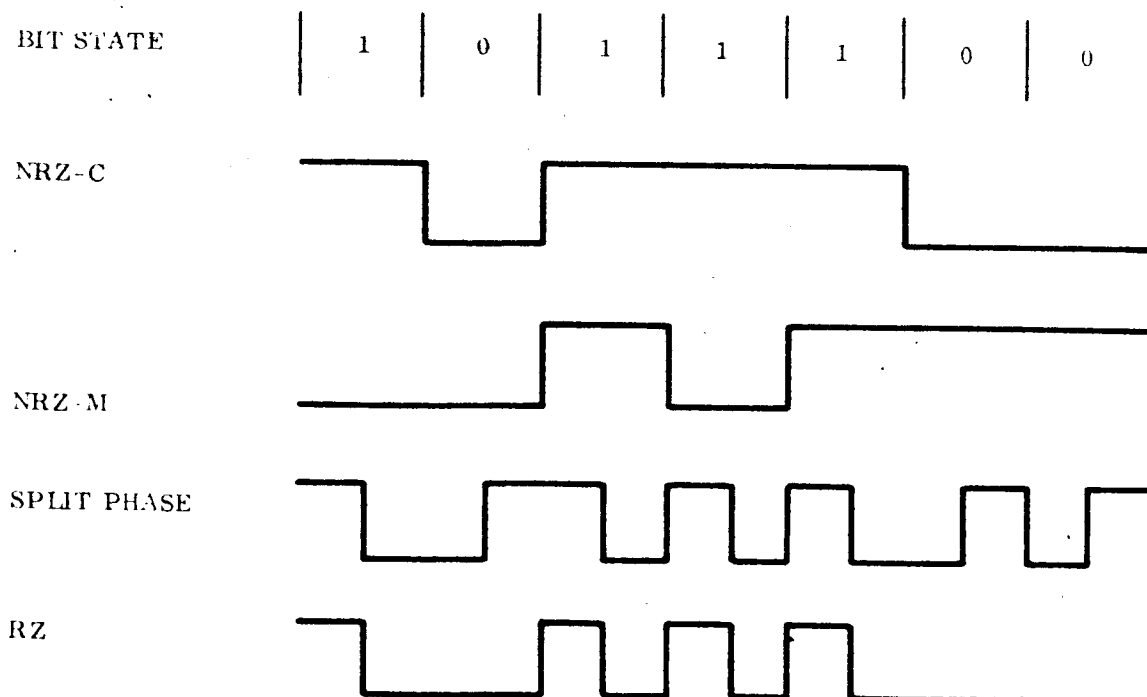
Figure N-2. PCM Waveforms

4.1.2.3 <u>Receiver Bandwidth Consideration</u> - The ratio of bit rate (in bits per second) to IF bandwidth (in cps) must not exceed 2/3. In those systems using synchronous detection, the IF bandwidth must be sufficiently large as to not cause significant lose in detection efficiency due to waveform distortion but must not be so large that the signal is difficult for the operator to detect.

4.1.2.4 <u>Changes in Bit Rates</u> - Bit rate changes during real-time transmission are permissible only by command from a ground station. Identification of the bit rate in use must be included as part of the telemetered data.

4.1.3 <u>Format</u>

4.1.3.1 <u>Frame Length</u> - The frame length shall not exceed 4096 bits.

4.1.3.2 <u>Word Length</u> - The word length shall not exceed 32 bits and shall be of constant length for any particular mission. This does not preclude different word structures as defined in the next section.

4.1.3.3 <u>Word Structure</u> - Word synchronization may consist of 0, 1, 2, or 3 bits per word and shall be the first bit or bits within the word when used.

Data bits shall occur next and may be composed of any number of syllables; however, the structure of any particular word shall remain constant. In those cases when the syllable represents a single measurand, the most significant shall occur first.

Parity shall be optional. If used, it shall be the last bit in a syllable or a word: Error correction and other redundant coding techniques may be used to enhance detection efficiency.

Reversal in the sequence of transmission is permissible if a spacecraft tape recorder is read-out during rewind.

4.1.3.4 <u>Submultiplexing</u> - The use of submultiplexing is acceptable subject to the restric-
tions of Section 4.1.3.3. When two or more submultiplexers are used they must be synchro-
nized and have either an equal number of channels or integral multiples.

4.1.3.5 <u>Supermultiplexing</u> - The use of supermultiplexing is acceptable. If possible, the
resultant sampling rate should be a harmonic of the frame rate.

4.1.3.6 <u>Variable Formats</u> - Variations in data channel assignments are permissible; how-
ever, when variable formats are used each frame must contain positive identification of the
format. The frame and word length must remain constant as well as the synchronization.
pattern.

4.1.4 <u>Synchronization</u>

4.1.4.1 <u>Bit Synchronization</u> - Bit synchronization is the first step in acquiring system
synchronization and sufficient changes-of-state must be provided for rapid, reliable syn-
chronization. All operating conditions shall be considered, such as primary power being
turned off to many of the experiments which could result in data without transitions. Where
similar conditions could exist, techniques such as restricting the dynamic range of the data,
odd parity or word synchronization should be used to insure bit transitions. The maximum
number of bits between transitions must not exceed 64.

4.1.4.2 <u>Frame Synchronization</u> - The PREFERRED method of frame synchronization is
to use a pseudo-random code with a length of 16 to 32 bits. This code pattern must occur
once per frame. Studies are now underway to determine codes for inclusion in these standards.
With this technique of synchronization, it is not necessary to devote bits in each word for
synchronization purposes.

An alternate method of synchronization is to use one or more bits at the start of each word
to establish bit phasing and one-word per frame with a unique code that cannot occur in the
data.

4.1.4.3 Submultiplexer Synchronization - A syllable in each main frame shall be used to indicate the subchannel number for the submultiplexer in that frame (e.g., 7 bits for 128 channels).

As an alternate, the main frame sync pattern may be completed once per longest submultiplexer frame. The two methods may be used together if desired and the complement of the frame pattern may be used to prevent the ground station from remaining locked to a false frame sync pattern.

4.2 PULSE FREQUENCY MODULATION TELEMETRY STANDARDS

4.2.1 Subcarrier Bands

Since the use of only one subcarrier band is permitted for this type of system, Table N-11 gives a set of recommended subcarrier bands along with the center frequency, sync frequency and sample rate. Table N-12 gives a set of recommended digital frequency levels for 8-level and 16-level systems.

Table N-11. PFM Analog Subcarrier Frequency Bands

Sync (S) Frequency (cps)	Data Subcarrier Frequency (cps)			Total Bursts per second (1/2T)
	Minimum	Center	Maximum	
4500 x 8	40,000	80,000	120,000	400
4500 x 4	20,000	40,000	60,000	200
4500 x 2	10,000	20,000	30,000	100
4500	5,000	10,000	15,000	50
4500/2	2,500	5,000	7,500	25
4500/4	1,250	2,500	3,750	12.5
TENTATIVE ALLOCATION				
4500/8	625	1,250	1,875	6.25
4500/16	312.5	625	937.5	3.125

Table N-12. PFM Digital Subcarrier Frequency Levels

8-Level System			Center Frequency KC/S	16-Level System		
Level Designation		Frequency Tolerance (± %)		Level Designation		Frequency Tolerance (± %)
Decimal	Binary			Decimal	Binary	
0	000	7.6	5.30	0	0000	3.8
			5.90	1	0001	3.4
1	001	6.2	6.50	2	0010	3.1
			7.10	3	0011	2.8
2	010	5.2	7.70	4	0100	2.6
			8.30	5	0101	2.4
3	011	4.5	8.90	6	0110	2.2
			9.50	7	0111	2.1
4	100	4.0	10.10	8	1000	2.0
			10.70	9	1001	1.9
5	101	3.6	11.30	10	1010	1.8
			11.90	11	1011	1.7
6	110	3.2	12.50	12	1100	1.6
			13.10	13	1101	1.5
7	111	2.9	13.70	14	1110	1.5
			14.30	15	1111	1.4

A ratio of 2:1 is set between systems using adjacent bands. This allows the processing of data with existing fixed-frequency, decoding ground station system by changing the tape speed on playback.

The data subcarrier oscillator minimum and maximum frequency deviations in Table N-11 are based upon a quantization of the dynamic range of a channel into one-hundred parts. A percentage reduction in the deviation will cause a corresponding percentage reduction in the accuracy.

The range of the subcarrier oscillator shall be clamped so that the upper frequency limit of the data band is not exceeded by more than two percent and the low limit not exceeded by more than five percent.

4.2.2 Frame Synchronization

Frame synchronization is effected in two ways: by transmitting a sync burst periodically at a unique frequency, and by increasing the duration of this burst.

The frequency of the synchronization burst shall be ten percent lower than the prescribed lower frequency edge of the data subcarrier band. The long-term stability of the sync subcarrier oscillator shall be better than one percent.

A synchronization burst shall be transmitted every sixteen data bursts. When the telemetry sequence is made up of more than one frame, alternate sync bursts shall be stepped in frequency to provide frame location information. This stepped frequency shall indicate from one to eight positions with the frequencies being the same as the frequency levels of the eight-level digital oscillators. For telemetry sequences from two to sixteen frames in length, the number of frames shall be divisible by two. Figure N-3 characterizes a 16-frame sequence.

The synchronization burst shall be 50 percent ± 10 percent longer in time duration than the normal burst duration. The reference burst preceding the sync burst shall be 50 percent ± 10 percent shorter than the normal burst duration.

The channel rate clock shall not vary more than plus or minus 1/2 percent from nominal. It is desirable to maintain the short term stability to one part in 100,000 so that channel synchronization can be predicted during extreme fades. The stability should be such that frame identification can be maintained for a four-hour period.

4.2.3 Format

PFM is a frequency shift system in which data bursts alternate with reference bursts. A frame shall be composed of one sync burst and fifteen data bursts separated by reference bursts. The signal may be generated in real time or played back from a previously recorded magnetic tape.
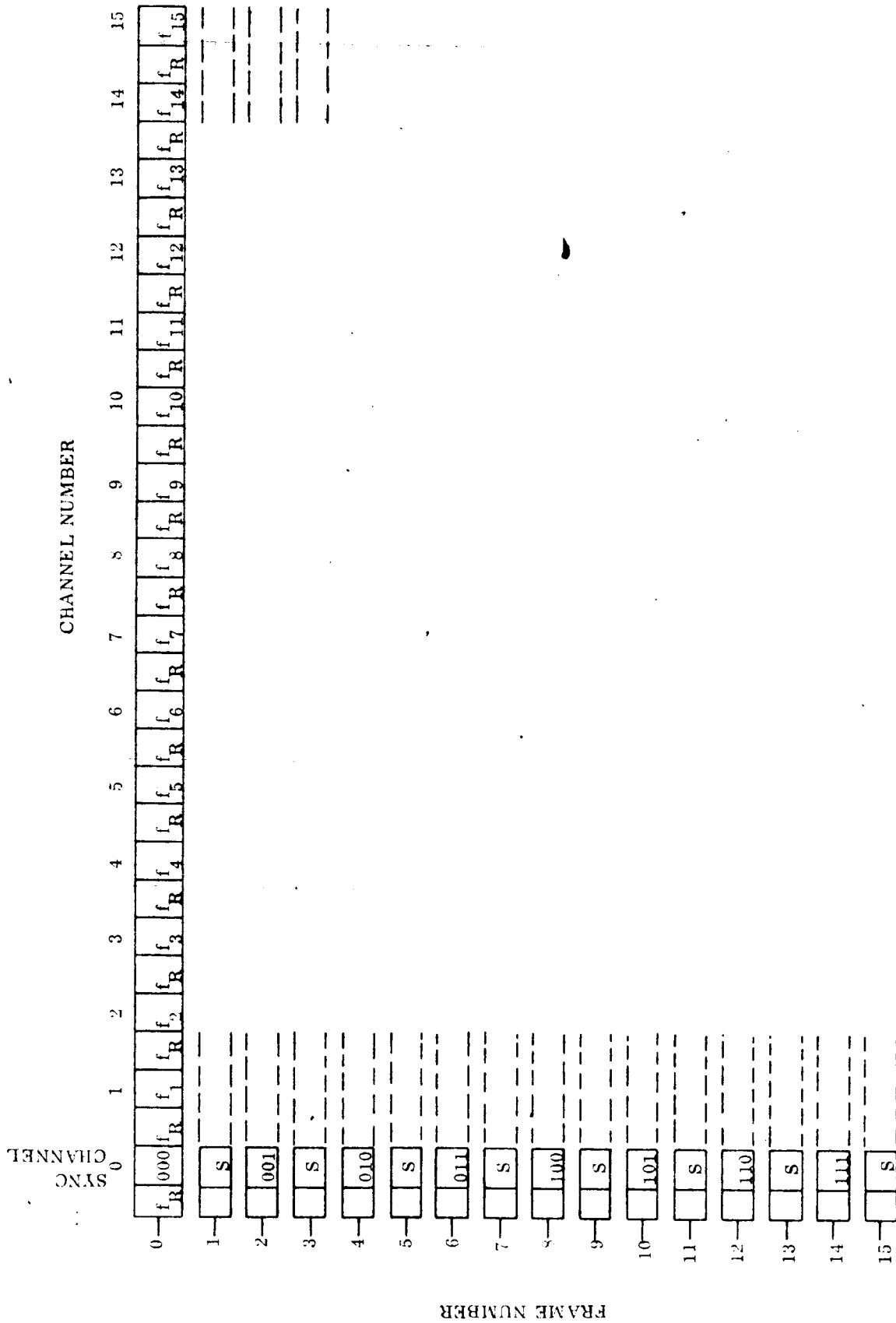
Figure N-3. 16-Frame PFM Telemetry Sequence

4.2.4 Reference Frequencies

To improve the modulation characteristics, reduce the Minitrack tracking error, and to monitor tape recorder speed, reference frequency bursts shall occupy the time between data bursts.

Real-time reference and recorder playback reference frequencies shall lie outside the data subcarrier band, one above the upper limit and one below the sync frequency as indicated in Figure N-4.
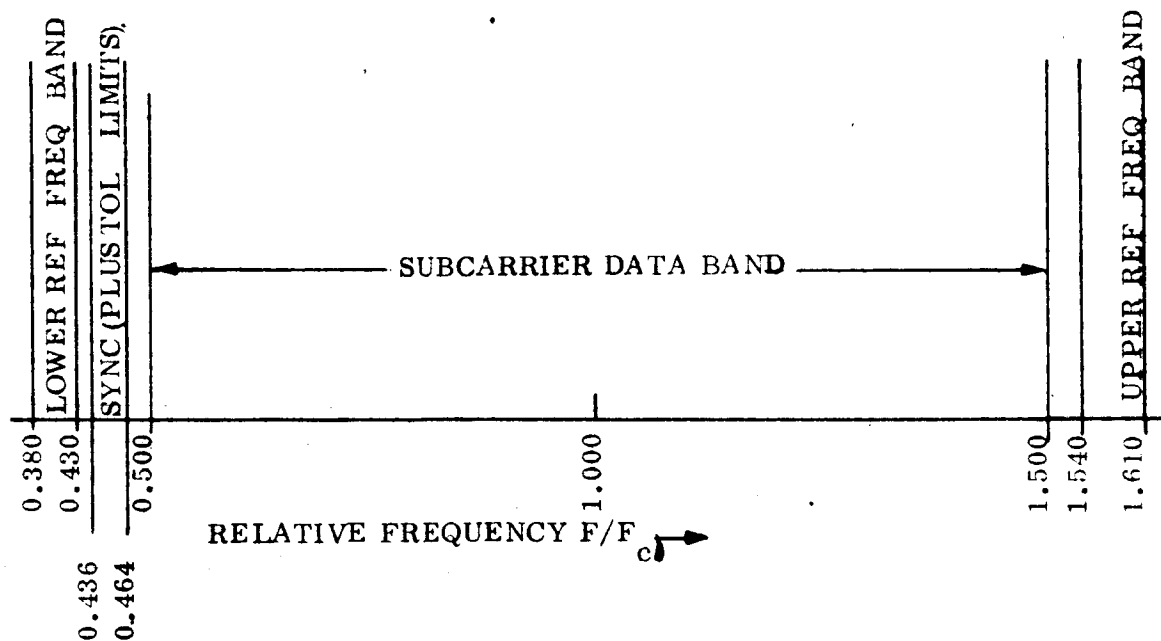
Figure N-4. Normalized (F_C is Data Band Center) Frequency Spectrum Showing Bands Available for Reference Frequencies

Reference frequencies shall be distinct from the command recognition and from the playback command frequencies.

Permissible values of generated reference frequencies are discrete values, each of which is centered within a filter of the contiguous filter bank. For a particular spacecraft, reference frequencies shall be selected from the values given in Table N-1. This selection shall be subject to the concurrence of areas involved in the generation, transmission, acquisition and processing of the reference frequencies.

The long-term stability of reference frequency shall be 0.01 percent.

Coherence shall be maintained in each reference frequency.

Table N-13. Permissible Values of Reference
Frequencies as Generated

Lower Reference Frequency Band (F/F_c)	Upper Reference Frequency Band (F/F_c)
0.38	1.55
0.39	1.56
0.40	1.57
0.41	1.58
0.42	1.59
	1.60
	1.61

5. REFERENCES

N-1   "Satellite Tracking and Data Acquisition Network Facilities Report (STADAN)," Report No. X-539-64-159, Goddard Space Flight Center, Greenbelt, Maryland, June, 1964.

N-2   "Descriptive Specifications and Tabulated Specifications, Minitrack Mod I Telemetry Receiver," Goddard Space Flight Center, Radio Systems Branch, Tracking Systems Division, Rev. June 7, 1960.

N-3   "Aerospace Data Systems Standards," Goddard Space Flight Center, Greenbelt, Maryland:

Part I, Section 1, "Pulse Code Modulation Telemetry Standards," 11/1/62.

Part I, Section 2, "Pulse Frequency Modulation Telemetry Standards," 11/1/62.

APPENDIX O

DEEP SPACE INSTRUMENTATION FACILITY TRACKING SYSTEM

APPENDIX O

DEEP SPACE INSTRUMENTATION FACILITY TRACKING SYSTEM

1. INTRODUCTION*

The Deep Space Instrumentation Facility (DSIF) has been established to satisfy the require-
ments in the lunar and planetary programs for a precision tracking and communications
systems capable of providing command, telemetry, and positional tracking of the space
vehicle. The DSIF is primarily intended for spacecraft tracking and communications at
cislunar distances and beyond and therefore is not designed for near-earth satellite track-
ing. The characteristics given in this appendix have been taken from Reference O-1.

The DSIF is presently comprised of three Deep Space Stations (DSS) and a mobile station,
and the intersite communication links providing for transfer of data and for administration
of operations by JPL. Two more stations are under construction. The DSS's are presently
equipped with 85-foot parabolic antennas and can track at angular rates up to one degree
per second. The mobile station is equipped with a 10-foot parabolic antenna and can track
at angular rates from 10 to 20 degrees per second, depending upon tracking accuracy. The
mobile station is used mainly for tracking and communication from injection to about
10,000 miles altitude.

The design philosophy of the DSIF is to provide a precision radio tracking system which
measures two angles, range, and range rate; and to utilize this system to send two-way
communications in an efficient and reliable manner. It is scheduled to undergo long-term
improvement and modernization consistent with the state of the art and spacecraft requirements.

The National Aeronautics and Space Administration is the cognizant agency responsible for
the DSIF. The Jet Propulsion Laboratory is under contract to NASA for the research, de-
velopment, and fabrication of the DSS's and mobile stations and for the technical coordination
and liaison necessary to establish and operate the DSIF throughout the world.

---

*This brief study of the DSIF tracking capabilities was undertaken before the solar probe
 orbit was eliminated. It has been included only for completeness.

Operational and computational support is provided the DSIF by the Space Flight Operations Facility (SFOF), located at the Jet Propulsion Laboratory in Pasadena, California. In addition to providing the capability for the real and non-real time reduction of tracking and telemetry data, the SFOF houses the DSIF Control Center from which operational control of the DSIF is exercised during space flight operations.

2. STATION LOCATIONS

DSIF stations are presently located at the following sites:

> Johannesburg, South Africa
> Goldstone, California, USA
> Woomera, Australia.

Additional stations are under construction at:

> Madrid, Spain
> Canberra, Australia.

The mobile station will, in most cases, be located so as to cover the injection point and the immediate post-injection trajectory of the spacecraft, which tend at the present time to be centered in the Southern Hemisphere.

The DSIF presently has 210-foot parabolic antennas under construction and plans to locate one of these antennas at each DSS site. The present schedule indicates that the first large antenna will be installed at Goldstone in 1967, the next at Johannesburg in 1968, and the third at Woomera in 1969. These antennas will employ altazimuth mounts (AZ-El coordinates). and have approximately 7 1/2-degree elevation limits.

3. TRACKING CAPABILITY

3.1 ANGLE TRACKING CAPABILITY

The automatic angle tracking systems used in the DSIF are of the simultaneous-lobing type. During the periods in which angle tracking accuracy is most significant (e.g., when data for an initial ephemeris calculation are required), the strong signal levels available result in an rms angle tracking error from 0.01 to 0.02 degree. The rms tracking error at receiver threshold increases to approximately 0.05 degree. Bias errors lie in the range of -0.1 to +0.1 degree. However, optical calibration techniques such as star tracking have led to the accurate determination of the bias error as a function of angle. The bias error is removed from the observed data at the computational facility.

The angle tracking design goals of the 210-foot DSIF antennas are a maximum angular rate of 0.5 degree per second and a pointing accuracy of 0.02 degree.

3.2 DOPPLER TRACKING CAPABILITY

All the DSIF stations have one-way and two-way Doppler capabilities. The distance at which the DSIF stations can obtain Doppler data is, of course, dependent on the sensitivity of the spacecraft receiver and the power output of the spacecraft transponder; if the carrier can be locked, Doppler can be made available.

The accuracy of one-way Doppler data is limited primarily by the unknown spacecraft oscillator drift. The accuracy is quoted as approximately 30 meters per second. In the two-way Doppler system, the frequency control is maintained by the ground transmitter exciter and is known precisely. Figure O-1 (Reference O-2, pp. 1-173 to 1-182) shows the major source of rms range rate error as a function of the smoothing time and the coherence time of the oscillator, which is defined by:

$$T_c = \frac{1}{(2\pi f)^2 s^2 \tau} \tag{1}$$

where   f = frequency of the oscillator

   s = specified oscillator instability

   τ = time interval over which the value of s is determined.

The transmitter master oscillator at the DSIF is slaved to a rubidium frequency standard providing a short-term stability of at least one part in 10^{11} over a ten-minute interval (Reference O-3). Using these values and a transmitter frequency of 2113 megacycles, the above equation indicates a coherence time of approximately 0.1 second. Therefore, the T_c = 0.1 second line in Figure O-1 should indicate the approximate capability of the DSIF for Doppler tracking.

3.3 PRECISION RANGING CAPABILITY

The DSIF Precision Ranging System measures the time difference between two identical, separately generated, pseudo-random noise codes (one generated at the transmitter for modulation and the other at the receiver for correlation detection) to represent range. The spacecraft transponder may or may not utilize the same correlation technique to reconstruct the code sequence before transmission to Earth. Reconstruction is needed for ranges comparable to planetary distances, but for lunar distances a simple "turn-around" transponder can be employed which transfers the modulation from the spacecraft receiver to its transmitter. Unambiguous ranging interplanetary distances is planned, with a round-trip propagation time measurement accuracy of 0.1μ seconds (i.e., ±50 feet, plus the error due to the uncertainty in the propagation velocity).

The general mode of operation for the ranging system is to initiate range modulation, establish range lock, and then remove range modulation and count carrier Doppler cycles to maintain the range tally. The need to provide these precision range measurements at planetary distances has not been established, since Doppler tracking over the extremely long smoothing times available appears to be satisfactory. However, the establishment of early direct range measurements (in cislunar space) for deep-space shots facilitates the early establishment of the trajectory parameters.

3.4 DSIF ACQUISITION PROCEDURES

The DSIF acquisition requirements can be separated into the following coordinates: two angles, frequency, range code, and telemetry subcarriers. Each coordinate acquisition has certain minimum time requirements which establish the shortest time in which it is possible to make a complete DSIF acquisition of the spacecraft.

Pointing information is usually provided for a tracking station; however, it is still necessary to search the area in which the spacecraft position is predicted. Supplied ephemeris data are usually accurate to within one degree, and the search time to acquire a usable signal is less than one minute once the spacecraft appears above the station's horizon.

After angle acquisition, radio-frequency lock to the spacecraft fixed-frequency signal is achieved in one to two minutes. A prior information as to the expected received frequency considerably reduces the time required to lock to the carrier.

In the two-way Doppler mode, the spacecraft transmitter is switched from the fixed-frequency exciter to a coherent variable-frequency exciter whose output is an exact multiple

of the signal received from the ground transmitter. Two-way, radio-frequency lock is not attempted until one-way lock has been achieved and requires an additional one to three minutes when the round-trip transmission time is short. At greater ranges the round-trip transmission time becomes the controlling factor.

Precision range signal lock is dependent upon prior establishment of two-way Doppler lock.

4. MARGIN CALCULATIONS

Sample margin calucations for DSIF Doppler tracking at a range of one astronomical unit are shown in Tables O-1 and O-2 for the earth-to-spacecraft and spacecraft-to-earth links, respectively. These tables are in the style preferred by JPL for DSIF margin calculations. The minimum performance margin required is equal to the sum of the negative tolerances on the individual gains/losses.

Table O-1 indicates that even with an unmodulated carrier on the earth-to-spacecraft link, somewhat more than 2.1 db of spacecraft receiving antenna gain will be necessary for two-way Doppler tracking at a range of one astronomical unit (unless the 100-kilowatt "emergency mode" ground transmitter is employed).

Table O-2 indicates that 100 watts of "effective radiated carrier power" (transmitter power times antenna gain) will allow one-way Doppler tracking at a range of one astronomical unit, but about twice as much radiated power will be required for two-way Doppler tracking.

Although these estimates provide helpful bench marks from which to initiate a system design, they are slightly optimistic as presented here. The carriers are usually modulated, and tolerances must be included for the carrier suppression factors, as well as the fact that pointing losses and tolerances must be included with the spacecraft antenna gains when they are inserted in the calculations. The result will be a requirement for a performance margin probably in excess of 6 db (for the tracking mode). These changes can be included as the system configuration becomes better defined.

O-6

Table O-1. Telecommunication Design Control Table

Project: Solar Thermionic Flight Experiment

Link: Earth-to-Spacecraft

Mode: Doppler Tracking

Notes: (Sample calculation only)
Isotropic spacecraft antenna with linear polarization
85-foot dish with 10-kilowatt transmitter at DSS
Based on Range of 1 AU (93 x 10^6 statute miles)
Tolerances based on Mariner '64 specifications (MC-4-310-A)

Item	Parameter	Value	Tolerance	Source
1.	C A L C U L A T I O N O F T O T A L R E C E I V E D P O W E R			
1.1	Total Transmitter Power (10 kw)	+ 40.0 dbw	±0.5 db 0.0	JPL
1.2	Transmitting Circuit Loss	- 0.4 db	±0.1 db	JPL
1.3	Transmitting Antenna Gain (85-ft dish)	+ 51.0 db	±1.0 db 0.5	JPL
1.4	Transmitting Antenna Pointing Loss	------ db	±--- db	(Included in 1.3)
1.5	Space Loss (2115 mc, 93 x 10^6 st mi)	-262.5 db	±--- db	(Calculated)
1.6	Polarization Loss	- 3.0 db	±--- db	D. Hagen
1.7	Receiving Antenna Gain	+ 0.0 db	±--- db	D. Hagen
1.8	Receiving Antenna Pointing Loss	- ---- db	±--- db	(Included in 1.7)
1.9	Receiving Circuit Loss	- 1.6 db	±0.4 db	JPL
1.10	Net Circuit Loss	-216.5 db	±1.5 db 1.0	(Sum of 1.2 through 1.9)
1.11	TOTAL RECEIVED POWER	-176.5 dbw	±2.0 db 1.0	(1.1 plus 1.10)

Table O-1. Telecommunication Design Control Table (Cont)

Item	Parameter	Value	Tolerance	Source
2.	C A L C U L A T I O N O F R E C E I V E R N O I S E			
	Noise Figure = 10 db +2 db $\qquad$ -1 db Ant Temp = _____ ^{o}K Sys Noise Temp = 2700 ^{o}K $\begin{array}{l}+1700^{o}\\-610^{o}\end{array}$			JPL
2.1	Noise Spectral Density (N/B)	-194.3 dbw/ cps	+2.1 db 1.1	(Calculated)
3.	C A R R I E R P E R F O R M A N C E		(GENERAL)	
3.1	Total Received Power	-176.5 dbw	+2.0 db 1.0	(From 1.11)
3.2	Carrier Suppression Factor $\quad$ Mod. Indices: $\qquad M_1 = $ _____ (Data) $\qquad M_2 = $ _____ (Sync)	- 0.0 db	+--- db	(Based on un- modulated carrier)
3.3	RECEIVED CARRIER POWER	-176.5 dbw	+2.0 db 1.0	(3.1 + 3.2)
3.4	Carrier Phase-lock Loop Noise $\quad$ Bandwidth ($2B_{LO}$ = 20 cps)	+ 13.0 db (cps)	+--- db	(Tolerance included in uncertainty of 2.1)
3.5	Loop Noise Power	-181.3 dbw	+2.1 db 1.1	(2.1 + 3.4)
4.	C A R R I E R P E R F O R M A N C E (ONE-WAY TRACKING) (Not Applicable)			
4.1	Threshold S/N in $2B_{LO}$	+ db	± db	
4.2	PERFORMANCE MARGIN	+ db	± db	(3.3 - 3.5 - 4.1) NET: +_____db
5.	C A R R I E R P E R F O R M A N C E (TWO-WAY TRACKING)			
5.1	Threshold S/N in $2B_{LO}$	+ 3.8 db	+--- db	JPL
5.2	PERFORMANCE MARGIN	+ 1.0 db	+3.1 db	(3.3 - 3.5 - 5.1) NET: -2.1 db

Table O-2. Telecommunication Design Control Table

Project: Solar Thermionic Flight Experiment

Link: Spacecraft-to-Earth

Mode: Doppler Tracking

Notes: (Sample calculation only)
Isotropic spacecraft antenna with linear polarization
85-foot dish with master preamplifier at DSS
Based on range of 1 AU (93 x 10^6 statue miles)
Tolerances based on Mariner '64 specifications (MC-4-310-A)

Item	Parameter	Value	Tolerance	Source
1.	C A L C U L A T I O N O F T O T A L R E C E I V E D P O W E R			
1.1	Total Transmitter Power (100 watts ERP)	+ 20.0 dbw	±1.0 db	D. Hagen
1.2	Transmitting Circuit Loss	- 1.5 db	±0.4 db	D. Hagen
1.3	Transmitting Antenna Gain	+ 0.0 db	±--- db	D. Hagen
1.4	Transmitting Antenna Pointing Loss	- ---- db	±--- db	(Included in 1.3)
1.5	Space Loss (2295 mc, 93 x 10^6 st mi)	-263.2 db	±--- db	(Calculated)
1.6	Polarization Loss	- 3.0 db	±--- db	D. Hagen
1.7	Receiving Antenna Gain (85-ft dish)	+ 53.0 db	±1.0 db 0.5	JPL
1.8	Receiving Antenna Pointing Loss	- ---- db	±--- db	(Included in 1.7)
1.9	Receiving Circuit Loss	- 0.2 db	±0.1 db	JPL
1.10	Net Circuit Loss	-214.9 db	±1.5 db 1.0	(Sum of 1.2 through 1.9)
1.11	TOTAL RECEIVED POWER	-194.9 dbw	±2.5 db 2.0	(1.1 plus 1.10)

Table O-2. Telecommunication Design Control Table (Cont)

Item	Parameter	Value	Tolerance	Source
2.	C A L C U L A T I O N O F R E C E I V E R N O I S E			
	Noise Figure = _____ db			
	Ant Temp = _____ ^{o}K			
	Sys Noise Temp = 55°K			JPL
	$\pm 10^{o}$K			
2.1	Noise Spectral Density (N/B)	-211.2 dbw/ cps	± 0.7 db 0.9	(Calculated)
3.	C A R R I E R P E R F O R M A N C E		(GENERAL)	
3.1	Total Received Power	-194.9 dbw	± 2.5 db 2.0	(From 1.11)
3.2	Carrier Suppression Factor Mod. Indices: M_1 = _____ (Data M_2 = _____ (Sync)	- 0.0 db	$\pm$--- db	(Based on un-modulated carrier)
3.3	RECEIVED CARRIER POWER	-194.9 dbw	± 2.5 db 2.0	(3.1 + 3.2)
3.4	Carrier Phase-lock Loop Noise Bandwidth (cps) ($2B_{LO}$ = 12 cps)	+ 10.8 db	± 0.0 db 0.5	JPL
3.5	Loop Noise Power	-200.4 dbw	± 3.0 db	(2.1 + 3.4)
4.	C A R R I E R P E R F O R M A N C E		(ONE-WAY TRACKING)	
4.1	Threshold S/N in $2B_{LO}$	+ 0.0 db	$\pm$--- db	JPL
4.2	PERFORMANCE MARGIN	+ 5.5 db	± 5.5 db 5.0	(3.3 - 3.5 - 4.1) NET: + 0.5 db
5.	C A R R I E R P E R F O R M A N C E		(TWO-WAY TRACKING)	
5.1	Threshold S/N in $2B_{LO}$	+ 2.0 db	± 1.0 db	JPL
5.2	PERFORMANCE MARGIN	+ 3.5 db	± 6.5 db 6.0	(3.3 - 3.5 - 5.1) NET: - 2.5 db

5. SPACECRAFT TRANSPONDER (Reference O-2, pp. 1-214 to 1-217)

5.1 GENERAL

The S-Band transponder normally receives a phase-modulated signal from earth; phase locks to the carrier; demodulates command signals and provides a modulated, coherent carrier to a power amplifier for subsequent transmission to earth. The transponder consists of two subassemblies: a phase-lock receiver, and a transmitter. Suitable equipments are available from several sources. Table O-3 summarizes the characteristics of transponders developed or actively being developed.

Table O-3. Characteristics Of Available Transponders

Characteristic	Hazeltine	STL	Motorola
Size	480 in.^3	184 in.^3	204 in.^3
Weight	18 lb	5.4 lb	12.5 lb
Power	35 watts	2 watts	9.6 watts
Noise Figure	13 db	10 db	10 db
Sensitivity (threshold lock)	--	-154 dbm	-154 dbm
Loop Bandwidth	--	10 cps	10 cps
S-Band Power Output	1 watt	0.5 watts	0.03 watts
MTBF (Hours)	--	38,900 hrs	15,200 to 20,100 hrs

The STL reliability numbers were received as 0.903 probability of success for six months for the receiver portion and 0.989 probability of success for six months for the transmitter portion. These numbers were converted to an MTBF of 38,900 hours in order to compare with Motorola's numbers. Both the Motorola and STL units are constructed from high reliability parts. Motorola's figure of 20,100 hours is based on substitution of new, more reliable parts into the existing transponder. The Hazeltine and Motorola receivers are double-conversion units, while the STL receiver is triple conversion. Motorola and STL

have units with similar functional requirements which Have successful flight histories in the 960 and 400-megacycle frequency bands, respectively. Based on superior performance, reliability, size, and weight, the STL unit appears the most desirable at this time.

6. <u>REFERENCES</u>

0-1. "System Capabilities and Development Schedule of the Deep Space Instrumentation Facility 1963-1967", JPL Technical Memorandum No. 33-83.

0-2. "Voyager Design Study", Part I, Vol. III, (Contract No. NASW-696), General Electric Company, Missile and Space Division, Oct. 15, 1963. pp. 1-173 to 1-182.

0-3. "Deep-Space Instrumentation Facility", Space Programs Summary No. 37-16, Vol. III, p. 40, JPL, Pasadena, California, July 31, 1962.

APPENDIX P

EVALUATION OF GENERATOR MISALIGNMENT
AND ORIENTATION ERROR SENSING
METHODS FOR SOLAR THERMIONIC SYSTEMS

APPENDIX P

EVALUATION OF GENERATOR MISALIGNMENT
AND ORIENTATION ERROR SENSING
METHODS FOR SOLAR THERMIONIC SYSTEMS

1. INTRODUCTION

This appendix deals with two areas which have not received very close scrutiny in the analysis of solar thermionic power systems. These are; (1) the effect of generator-concentrator misalignment, and (2) orientation error sensing methods.

The analysis presented here was not performed as part of this contract but is included here because of its pertinence to this study. The analysis was conducted by Leonard Dutram of the General Electric Spacecraft Department on Department Funds. The concentrator performance was computed using a IBM 7094 computer program developed by Dr. George Schrenk of the University of Pennsylvania. Dr. Schrenk consulted on the overall problem and prepared the input sheets for the concentrator performance computations. Al Lowi of the Aerospace Corporation made the computer runs. Dr. Schrenk and Mr. Lowi's work was performed at no charge to the General Electric Company.

The first area, generator-concentrator misalignment, is illustrated in Figure P-1. This corresponds to the situation where the generator has been moved from the focal point of the concentrator due to some perturbation (shock, thermal distortions, etc.) while the aperture remains in the focal plane. Misalignments which cause the generator aperture to move out of the focal plane have not been considered due to insufficient concentrator data. The amount of energy passing through the generator aperture as the amount of misalignment, x, varies is determined.

The second area to be considered involves the evaluation of two methods of sensing orientation of the concentrator to the sun. This evaluation is carried out for two types of sensors, under various conditions of generator misalignment and concentrator misorientation. The two types of sensors considered, are shown conceptually in Figure P-2.

INCIDENT SOLAR FLUX

THERMIONIC GENERATOR

CONCENTRATOR OPTIC AXIS

SOLAR CONCENTRATOR
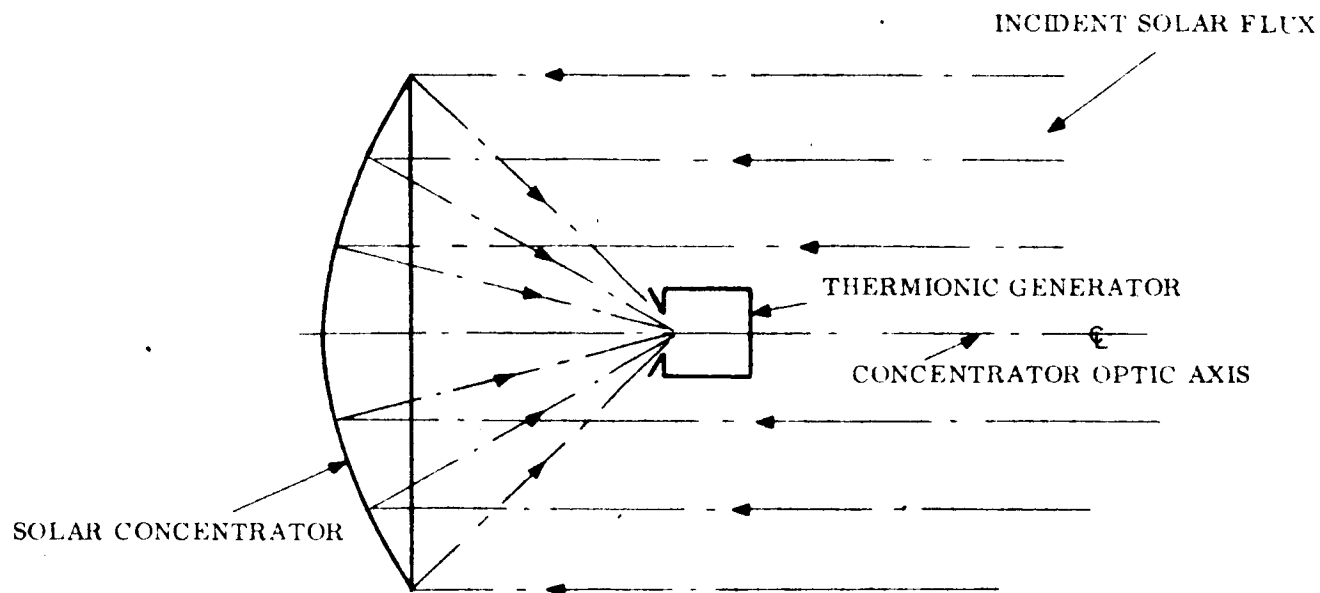
(a) GENERATOR ALIGNED TO CONCENTRATOR

X - GENERATOR MISALIGNMENT
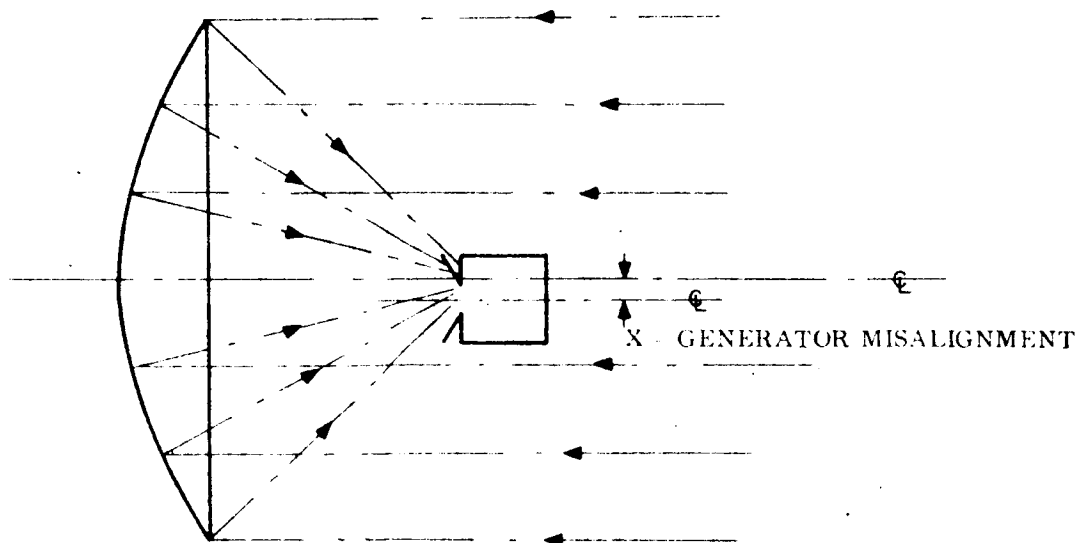
(b) GENERATOR MISALIGNED

Figure P-1. Illustration of Generator Misalignment

Figure P-2a illustrates a solar thermionic system using a boresight sensor. The sensor is contained at the base of a tube shown mounted on the rim of the concentrator. The sensor senses the sun's image and provides a signal to the orientation system. The separate and combined effect of sensor misorientation and generator misalignment is analyzed to determine the energy entering the generator aperture.

Figure P-2b indicates a sensing method whereby sensors mounted about the generator aperture, sense the concentrated solar flux. These sensors then provide a signal which tends to equalize the flux incident on diametrically opposite sensors. In this manner the orientation of the power system can be adjusted to provide the proper flux distribution in the focal plane and thus maintain orientation of the system. In addition, it is felt that this method would significantly reduce the effect of generator misalignment by providing a sensor which is sensitive to changes in flux distrubution produced by either misalignment or misorientation.

The analysis included does not consider how accurately a solar thermionic system could be oriented by the flux sensor system. This depends on more specific design considerations than are investigated here.

2. NOMENCLATURE

The symbols employed in this analysis are defined below:

A_c	=	Projected area of solar concentrator
E	=	Energy entering the generator aperture
Q_{net}	=	Energy entering the generator aperture minus the energy radiated from the cavity
	=	Energy available to the generator for conversion
Q_{rerad}	=	Energy reradiated from the cavity
R_c	=	Radius of the concentrator
R_s	=	Radius of circle on which flux sensors are mounted.

Boresight Tube

Thermionic Generator

$\mathbb{C}_1$ Parallel to $\mathbb{C}_2$

Solar Concentrator
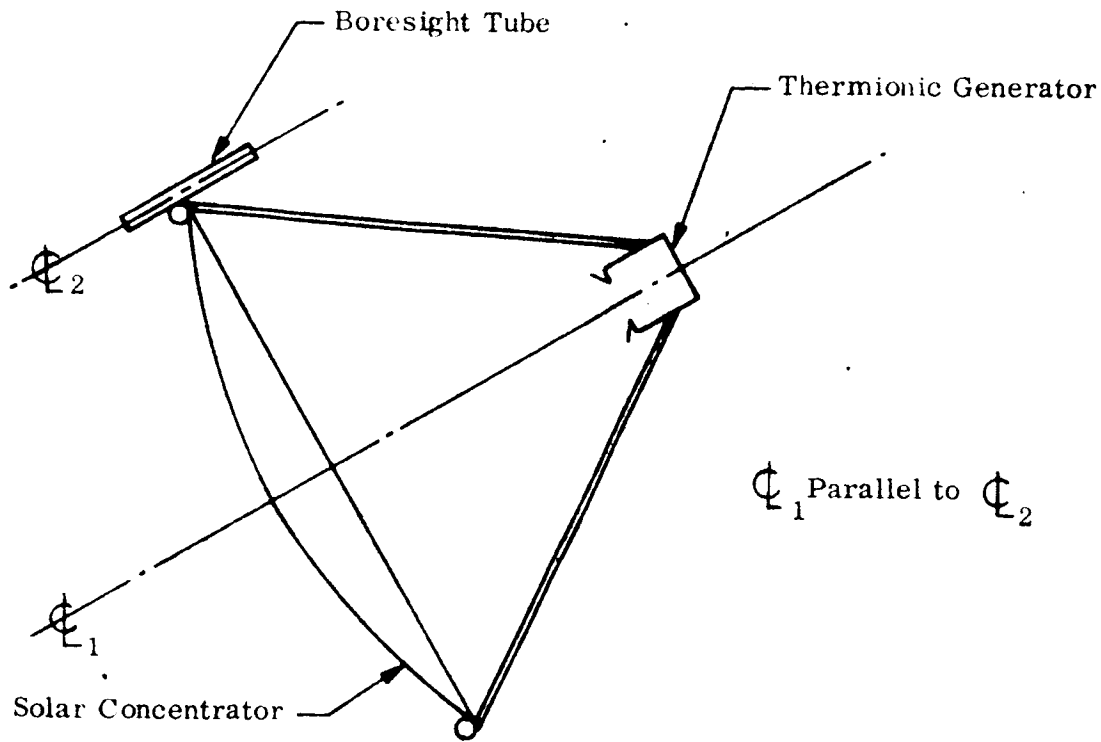
(a) Boresight Sensor Method

Thermionic Generator

Incident Flux

Aperture
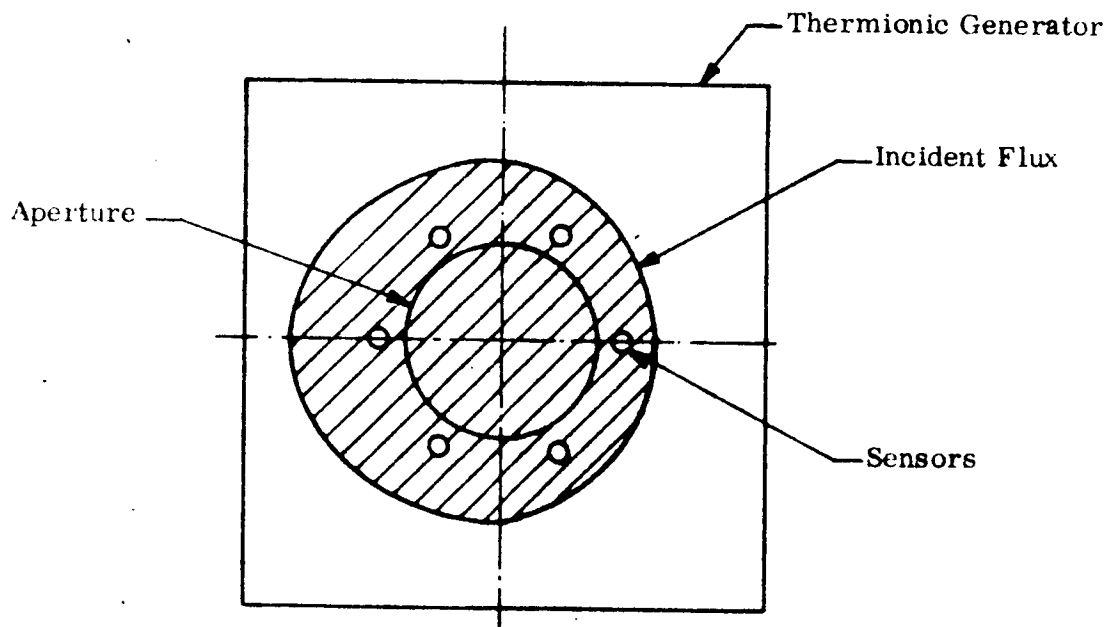
Sensors

(b) Concentrated Flux Sensing Method

Figure P-2. Illustration of Sensing Methods

R_{so} = Sensor circle radius that produces a misorientation of β_o which is optimum for X_{ao}

R_s^* = Sensor circle radius that produces nearly optimum concentrator misorientation for a range of generator misalignment

r = Radius of generator aperture

T_c = Cavity temperature

I_s = Solar intensity incident on concentrator

x = Distance from concentrator optic axis to center of generator aperture = Generator Misalignment

X_a = That amount of misalignment, which causes the concentrator to be misoriented through an angle β_o, for a given sensor radius, R_s

X_{ao} = That amount of misalignment, which causes the concentrator to be misoriented through an angle β_o, which is optimum for that particular amount of misalignment. (See Figure P-17)

β_o = Orientation (misorientation angle) = Angle between concentrator optic axis and concentrator-sun line

ρ = Reflectivity of concentrator surface.

3. SUMMARY AND RESULTS

3.1 GENERATOR MISALIGNMENT

For the purpose of this study, generator misalignment has been defined as a movement of the generator, off of the optic axis of the concentrator with the generator remaining in the focal plane. Limiting misalignment to the focal plane was necessary because concentrator data was available only for the focal plane case.

Figure P-3 (same as P-16) shows the variation in energy entering the generator aperture as the generator is misaligned from the optic axis of the concentrator. This is shown for a generator aperture which has been optimized for a cavity temperature of $2000^\circ K$ (See
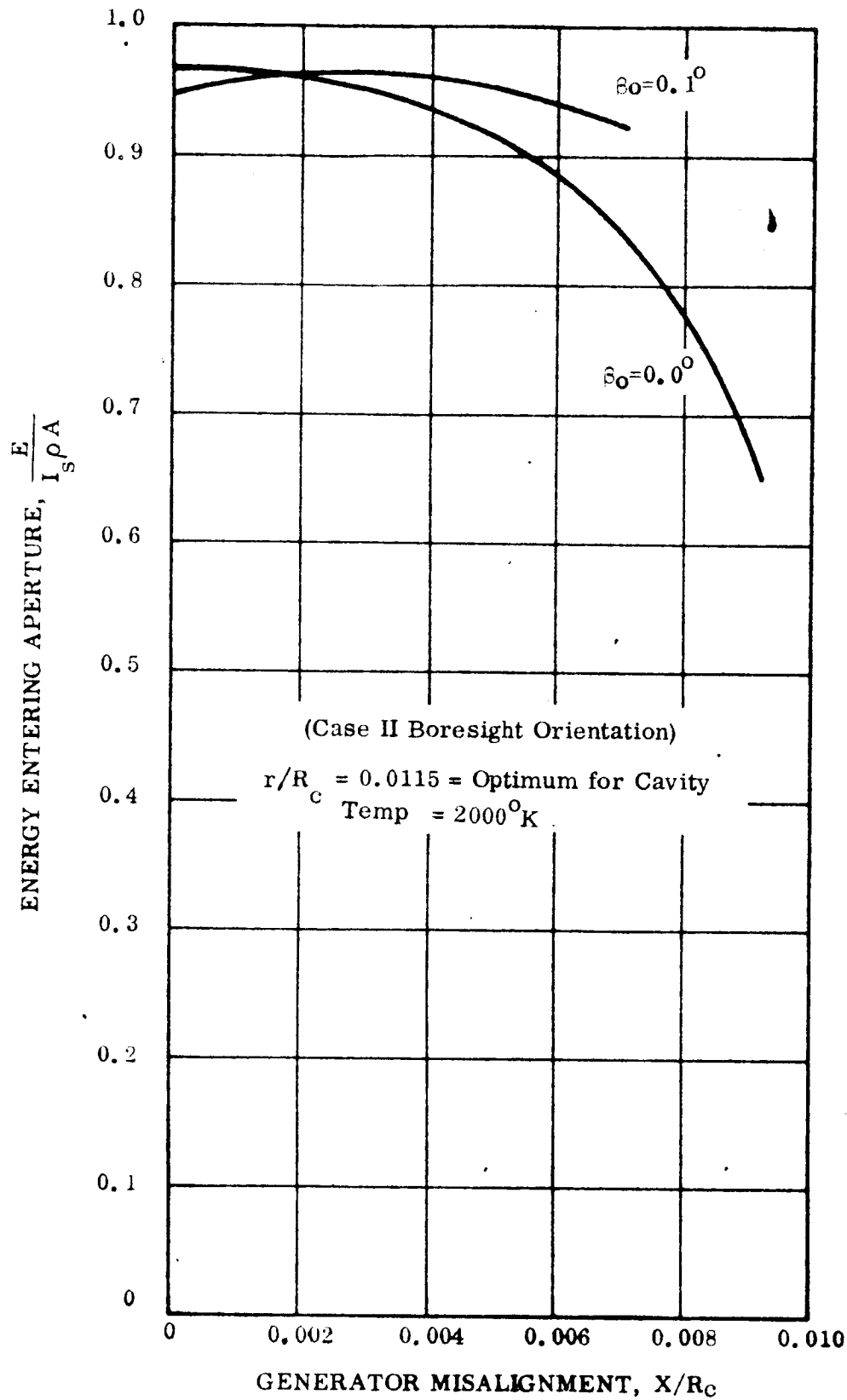
Figure P-3. Energy Entering Aperture vs. Generator Misalignment

Section 4.2). Since a variation of ± 0.1 degree is expected in the orientation system accuracy, the plot has been made for flux distributions corresponding to orientation errors of 0.0 and 0.1 degrees. For a given generator misalignment x/R_c, the energy entering the aperture will vary between the two curves shown in Figure P-3 as the orientation error varies between 0.0 and 0.1 degrees.

3.2 EVALUATION OF ERROR SENSING METHODS

Two types of sensor systems are considered. The first sensing method considered is known as boresight orientation. This method has been used successfully in ground solar testing of thermionic generator systems and is considered applicable for space missions. The second system to be considered is based upon sensing the concentrated solar flux in the focal plane and thereby orienting the concentrator so as to maximize the energy entering the aperture. The reason for considering this second method of orientation was to determine whether a system such as this could minimize the effect of any generator misalignment.

The results of this evaluation are presented in Figure P-4. It is shown in Section 5.2.3 that if the radius of the circle, on which the sensors are mounted, is properly selected, the flux sensing orientation system will always orient the concentrator to deliver nearly maximum energy to the generator for any generator misalignment. For the sensor circle radius selected, $R_s^*/R_c = 0.0126$, the energy entering the aperture is truly maximized up to a misalignment of $x/R_c = 0.0222$ and very nearly maximized up to $x/R_c = 0.040$. The boresight system on the other hand does not perform as well except in the case where the boresight tube is coincidentally misoriented by the proper angle to shift the energy into the misaligned generator.

3.3 SUMMARY

The results presented here do not attempt to predict the limits within which a flux sensing orientation system will orient a concentrator to the sun. These limits will be fixed by the specific design and components used. The results do indicate that if such a system could
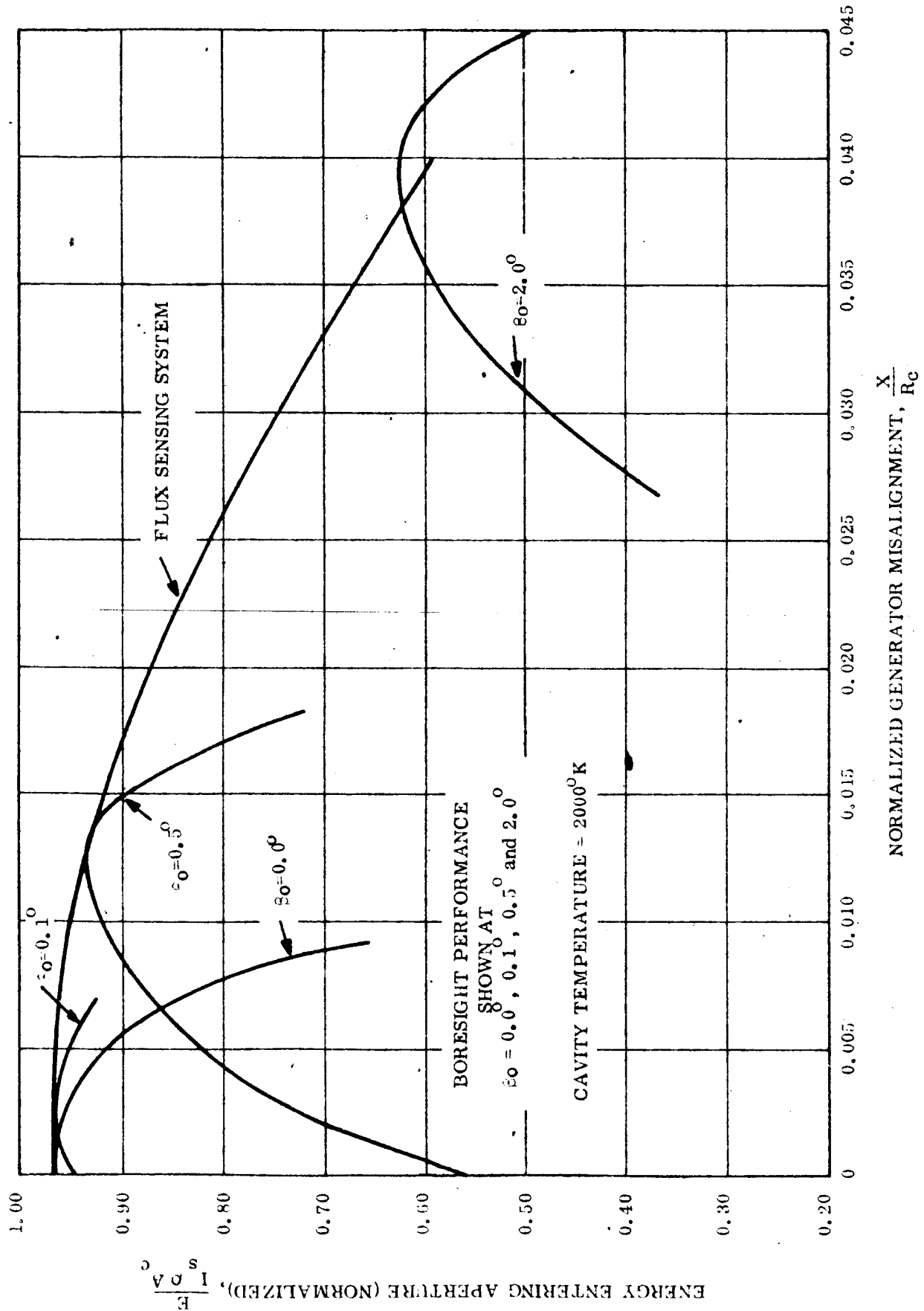
Figure P-4. Sensor Performance Comparison for $r/R_c = 0.0155$

be practically devised, the importance of generator-concentrator misalignment produced by shock, launch loading, thermal distortion, etc. would be greatly minimized.

For example, a 50-inch diameter, 60-degree rim angle concentrator could experience a generator-concentrator misalignment of 0.278 inches and still receive as much energy as normally reaches a perfectly aligned generator at 0.1-degree concentrator misorientation.

The results presented have been normalized to the radius of the concentrator to improve their applicability. The results are limited to the following types of concentrators:

a. Concentrator Rim Angle = 60 degrees

b. Concentrator diameter must be such that the assumption that the concentrator geometric error distribution has a 3σ value of 12 minutes, is applicable.

c. The curves indicating performance with misalignment have been calculated based on an aperture radius of $r/R_c = 0.0115$. This diameter is optimum for a cavity temperature of $2000^{\circ}K$.

Should these results be required at a different cavity temperature, Figures P-9 through P-12 could be used to generate the performance data at the appropriate aperture radius.

4. SOLAR CONCENTRATOR PERFORMANCE

4.1 BASIC CONCENTRATOR DATA

Solar concentrator data for this analysis was obtained from Dr. G. Schrenk of the University of Pennsylvania. The computer analysis which generates this data is described in Reference P-1. The computer runs were performed by A. Lowi of the Aerospace Corporation at the request of Dr. Schrenk. The solar concentrator parameters used for these computer runs were as follows:

Concentrator Diameter	=	44 inches
Sun's Image Angle	=	32 minutes of arc
Concentrator Geometric Errors		
Radial Error Mean Deviation, σ	=	4 minutes of arc
Circumferential Error Mean Deviation, σ	=	0 minutes of arc
Misorientation Errors	=	0°, 0.1^{o}, 0.5^{o}, and 2.0^{o}
Concentrator Rim Angle	=	60°

The radial geometric error was selected as being representative of concentrators of the diameter considered. The circumferential error was neglected due to the fact that its effect is not as important as the radial error and because its omission significantly reduces computation time. The misorientation errors were selected on the basis of covering the range of misorientation of interest. In particular, 0.1 degrees misorientation error was selected since it is felt that an orientation system which can control within $\beta_{o} = \pm 0.1$ degrees is required. The orientation error is defined as the angle between the sun concentrator line and the optic axis of the concentrator (see Figure P-5a).

The following basic data was generated by the computer program:*

 a. The flux distribution in the focal plane of the concentrator
  for each of the misorientation errors considered

---

*The computer program used for these calculations was not the same one used in Section 4 (Volume II) to estimate the thermionic system performance. As a result, the performance estimates from the two programs differ even for the same input conditions. The program used to obtain the performance estimates presented in the appendix predicts significantly higher concentrator performance than does the one used in Section 4.

Concentrator-Sun Line

Focal Plane

βo — Orientation Error

Concentrator Optic Axis

Solar Concentrator
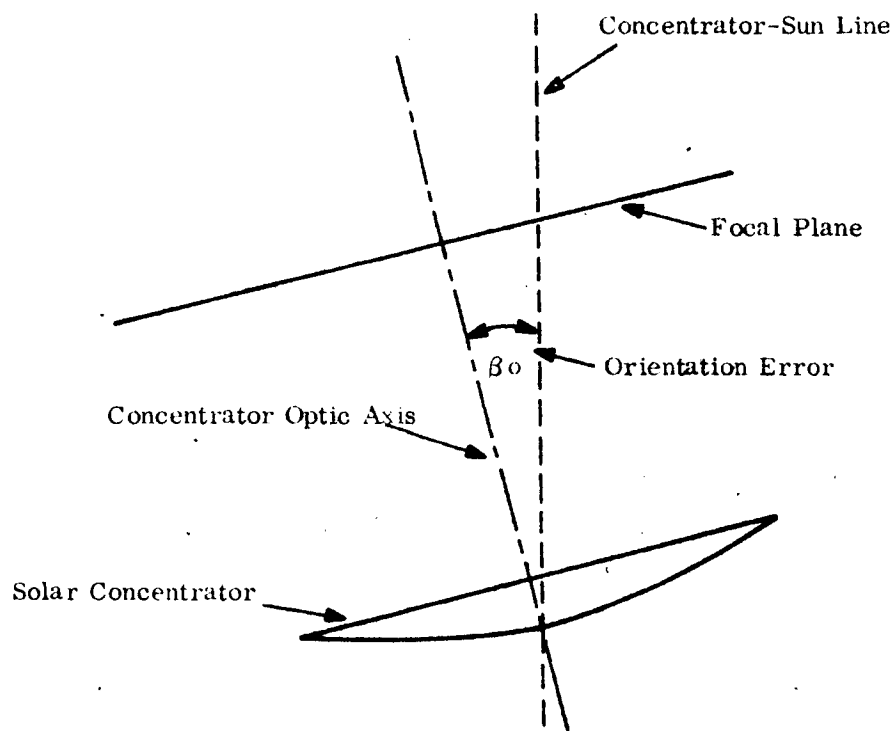
(a) Solar Concentrator Misorientation Detail

Distorted Spot in Focal
Plane due to Misorientation

y

$\theta = \pi$

$\theta = 0$

x

θ_1

θ_N

θ_{N-1}

θ_2

θ_1

θ_3

$(x=0, y=0)$ — Intersection of Concentrator
Optic Axis With Focal Plane.
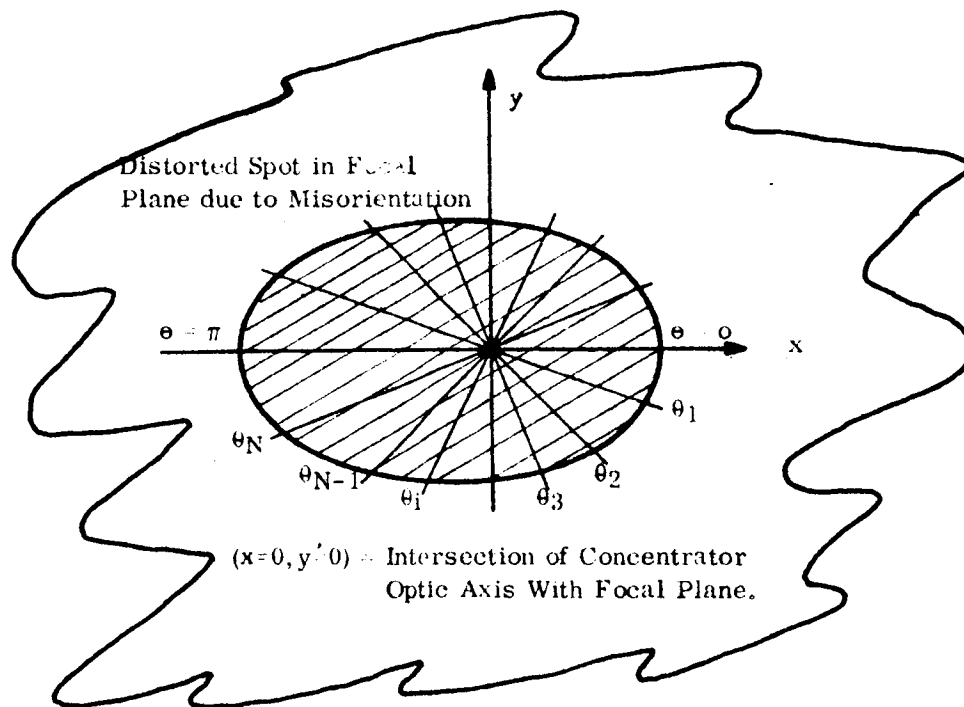
(b) Concentrator Focal Plane Detail

Figure P-5. Definitions of Misorientation Nomenclature

b. The fraction of the total energy indicent on the concentrator which passes through apertures of various sizes (the center of these apertures is located on the optic axis of the concentrator and in the focal plane.)

Figure P-5b illustrates the skewed spot in the focal plane which results from misorientation of the concentrator. The flux density is computed along the lines θ_i. Since the distribution is symmetric about the 0-π line, only half the disbribution is calculated. The number of θ_i increments used in the computation varies with misorientation error for the sake of accuracy. The flux distribution is then integrated about the point X = 0, Y = 0 to yield the fraction of the total energy passing through various size apertures which have their center at X = 0, Y = 0.

For the sake of generality, the data has been normalized. This has been carried out by normalizing all distances in the focal plane, to the radius of the concentrator. This makes the data applicable to a range of concentrator diameters with a 60-degree rim angle where a comparable geometric accuracy can be achieved.

Figure P-6 shows a plot of the flux distribution, at various misorientation angles, along the x-axis (0 - π plane) of Figure P-5b. Similar distributions are calculated for other angular increments as discussed above. Figure P-7 shows the calculated energy entering apertures located on the concentrator optic axis and in the focal plane, as a function of aperture radius.

4.2 APERTURE SIZE SELECTION

Since an orientation system accuracy of 0.1-degree is expected, the concentrator aperture system is sized at β_o = 0.1-degree in order to insure that sufficient energy is available to the generator during the orientation system swings. The design generator cavity temperature is $2000^{\circ}K$.

$\beta o=0.5^{o}$

$\beta o=2.0^{o} \rightarrow$

0.07   0.06   0.05   0.04   0.03   0.02

GENERATOR MISALIGNM[
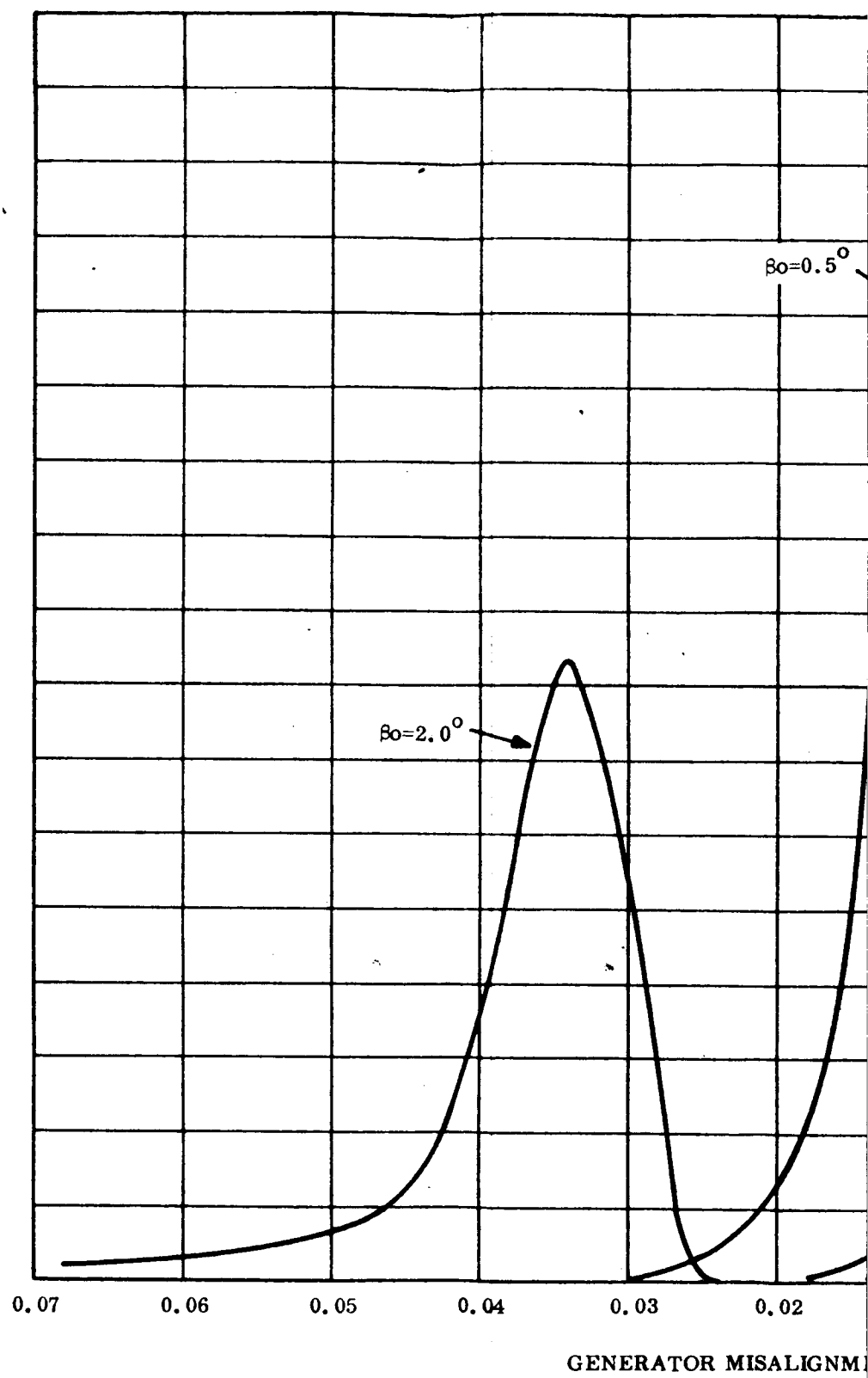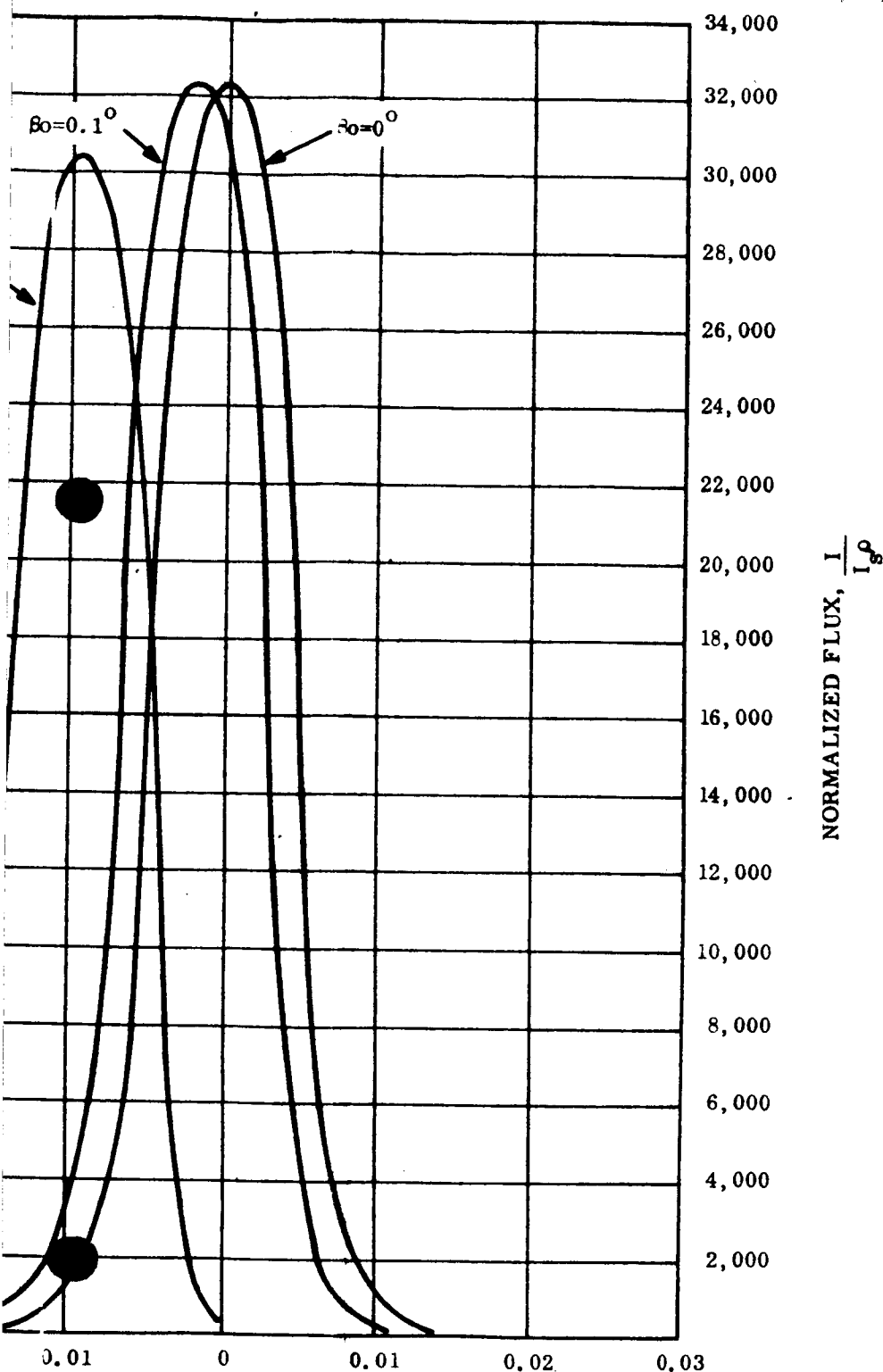
Figure P-6. Flux Distribution in $(0 - \pi)$ Plane
for Various Misorientation Errors
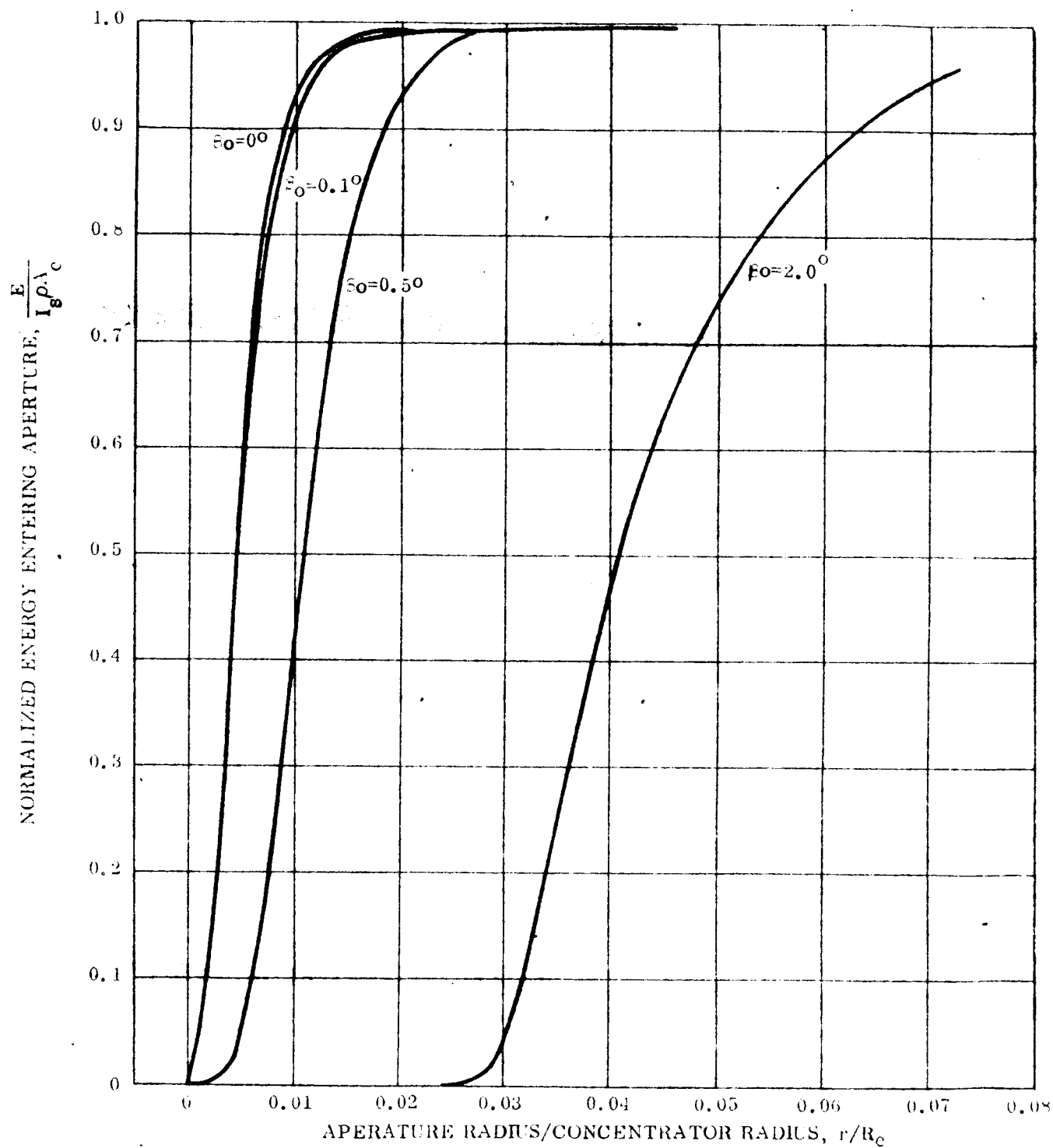
Figure P-7. Energy Entering Aperture at Various Misorientation Errors for
Aperture Located on Concentrator Optic Axis

The net energy into the cavity is defined as the energy entering the aperture less the black-body reradiation loss:

$$Q_{NET} = E - Q_{rerad} = E - \sigma(\pi r^2) T_c^4.$$ (1)

Dividing through by the total solar energy leaving the concentractor, E_T, where

$$E_T = I_s \rho A_c + =. I_s \rho \pi (R_c)^2$$ (2)

Equation 1 becomes

$$\frac{Q_{NET}}{I_s \rho \pi R_c^2} = \frac{E}{I_s \rho \pi R_c^2} - \frac{\sigma}{I_s \rho}\left(\frac{r}{R_c}\right)^2 T_c^4$$ (3)

Equation 3 may be optimized to determine the value of r/R_c which makes the maximum energy available to the generator.

The quantity $\dfrac{E}{I_s \rho A_c}$ is available from Figure P-7, where $\beta_0 = 0.1$ degrees. The blackbody radiation may be computed for various values of r/R_c. The resulting net energy optimization is shown in Figure P-8. This results in an optimum radius ratio of

$$r/R_c = .0115$$ (4)

. 4.3 GENERATION OF MISALIGNMENT DATA

The concentrator focal plane data described heretofore, considers only apertures located at the intersection of the concentrator optic axis and the focal plane. In order to evaluate off-axis generator misalignments, it is necessary to know the energy entering apertures located in the focal plane but not on the optic axis of the concentrator. In order to generate data of this type, it is necessary to integrate the flux distribution, described previously, about other centers. An IBM 7094 computer program, designated IOLI, was written to

perform this integration. The program performs an integration over the area of the aperture using Simpson's rule. The routine allows computation of the energy entering an aperture located anywhere in the focal plane, knowing the flux distribution. A more detailed description of this routine is presented in Reference P-2. Input and input format required for the IOLI program is described in Reference P-3.

The data that has been generated is in the form of energy entering apertures of various sizes located at several points on the x-axis (see Figure P-5b) and at various misorientation angles, β_o. This data is shown in Figures P-9 through P-13. Figures P-9 through P-12 show the energy entering an aperture at various misaligned positions and as a function of aperture radius for various misorientation errors. Figure P-13 shows the variation in total energy entering the optimum aperture size calculated in Section 4.2. This corresponds to the energy entering the cavity of a generator which is misaligned to varying degrees, as the orientation system error varies.

5. ORIENTATION SENSOR PERFORMANCE

5.1 BORESIGHT SENSOR

The boresight orientation system consists of a sensor mounted on the rim of the concentrator. This sensor is aligned so that its axis is parallel with the optic axis of the concentrator, (see Figure P-20). A coarse control orients the concentrator to the general sun direction with the boresight system providing fine control.

In addition to the limiting orientation accuracy of the system, ($\beta_o = \pm 0.1$ degrees is expected) the following orientation and generator alignment errors may be encountered.

    a. Case I – The boresight tube may be misoriented (due to shock, thermal distortion, etc.) so that the centerline of the tube is no longer parallel with the optic axis of the concentrator (See Figure P-14).

APERTURE RADIUS/CONCERTRATOR RADIUS, r/R_c

$$\frac{Q_{net}}{I_s \rho A_c}$$

Q_N

FRACTION OF NET ENERGY TO GENERATOR, Q_N.
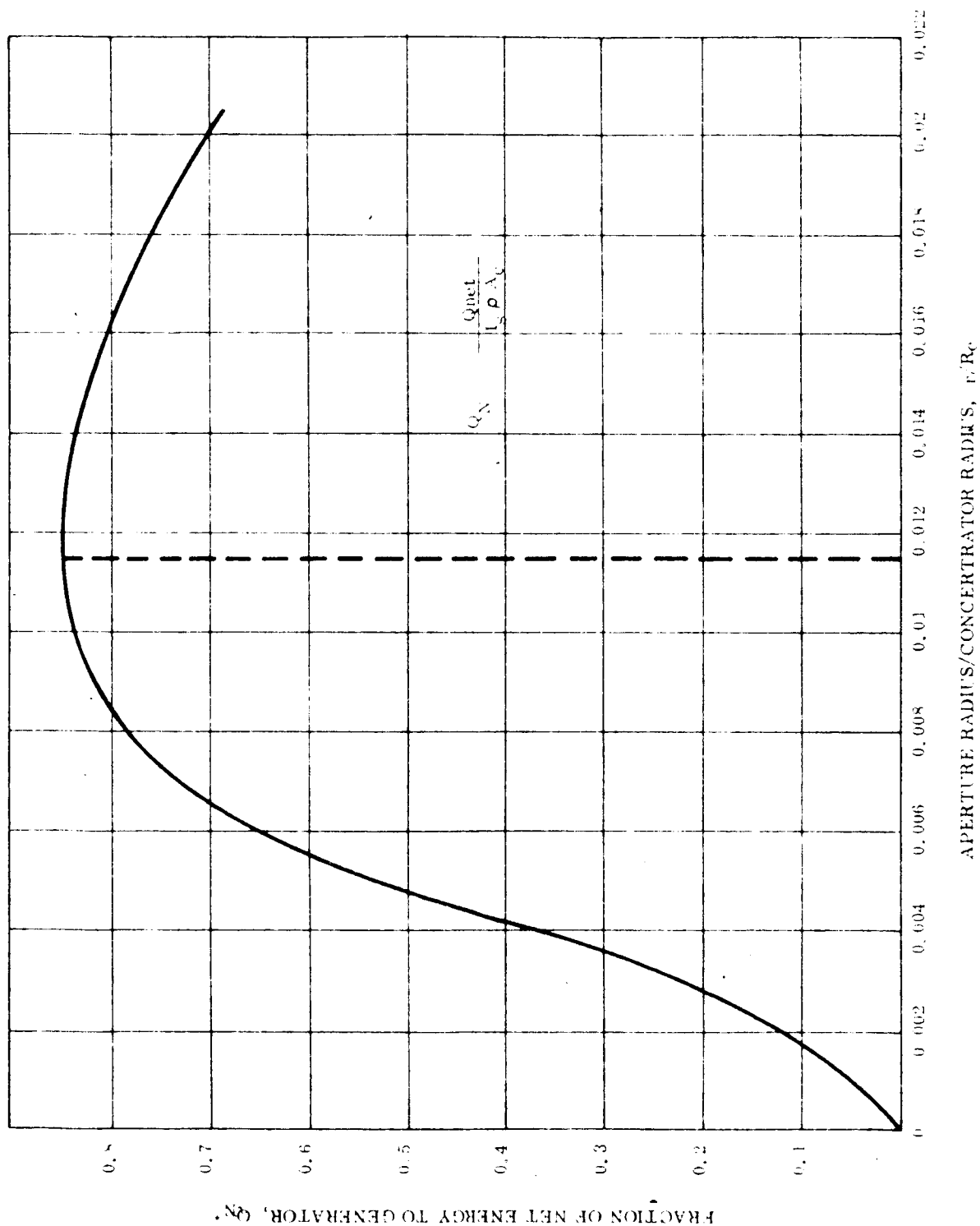
Figure P-8. Determination of Optimum Aperture Diameter for a Cavity Temperature of $2000^\circ K$
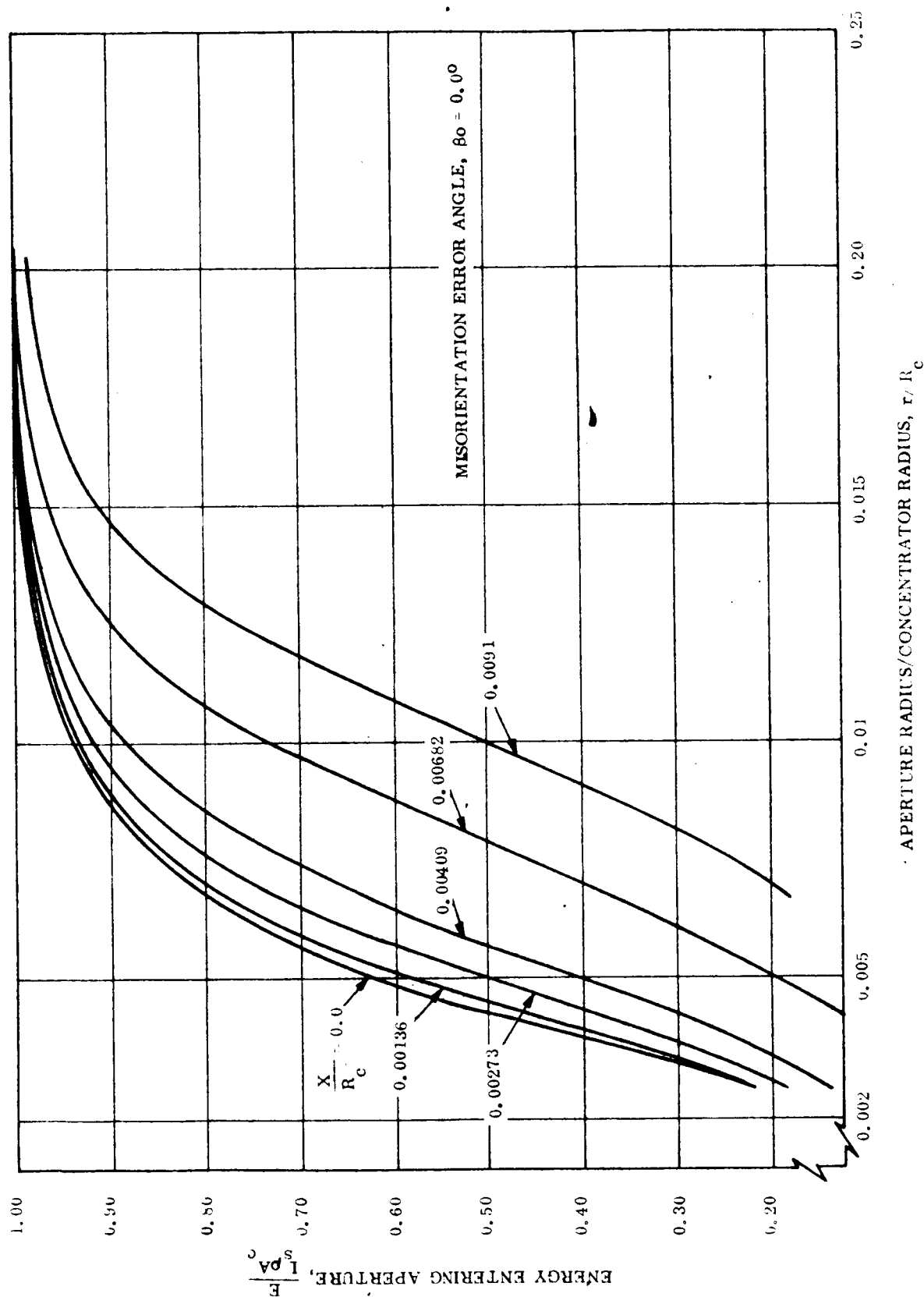
Figure P-9. Normalized Energy Entering Aperture vs. Normalized Aperture Radius for Various Misaligned Positions
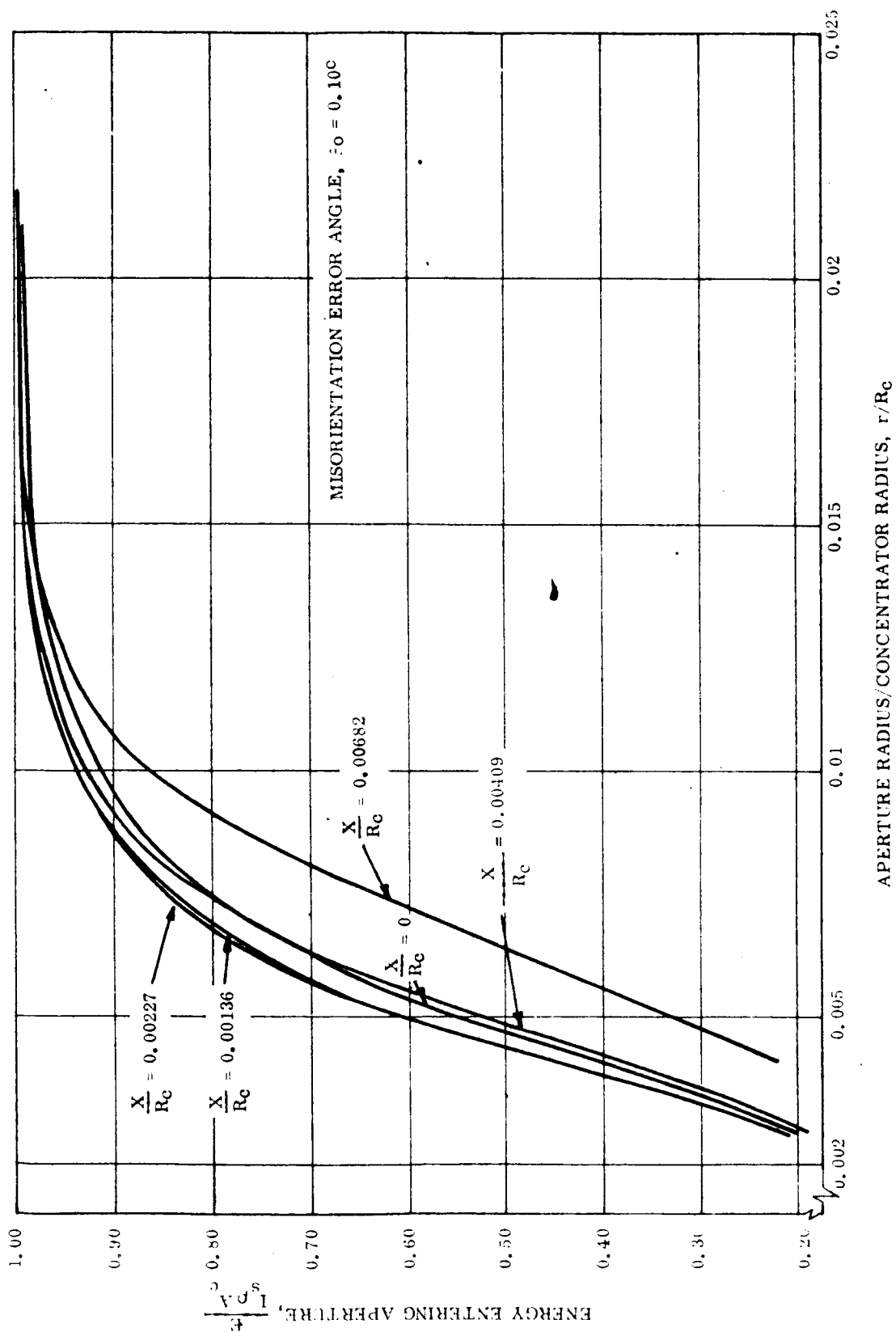
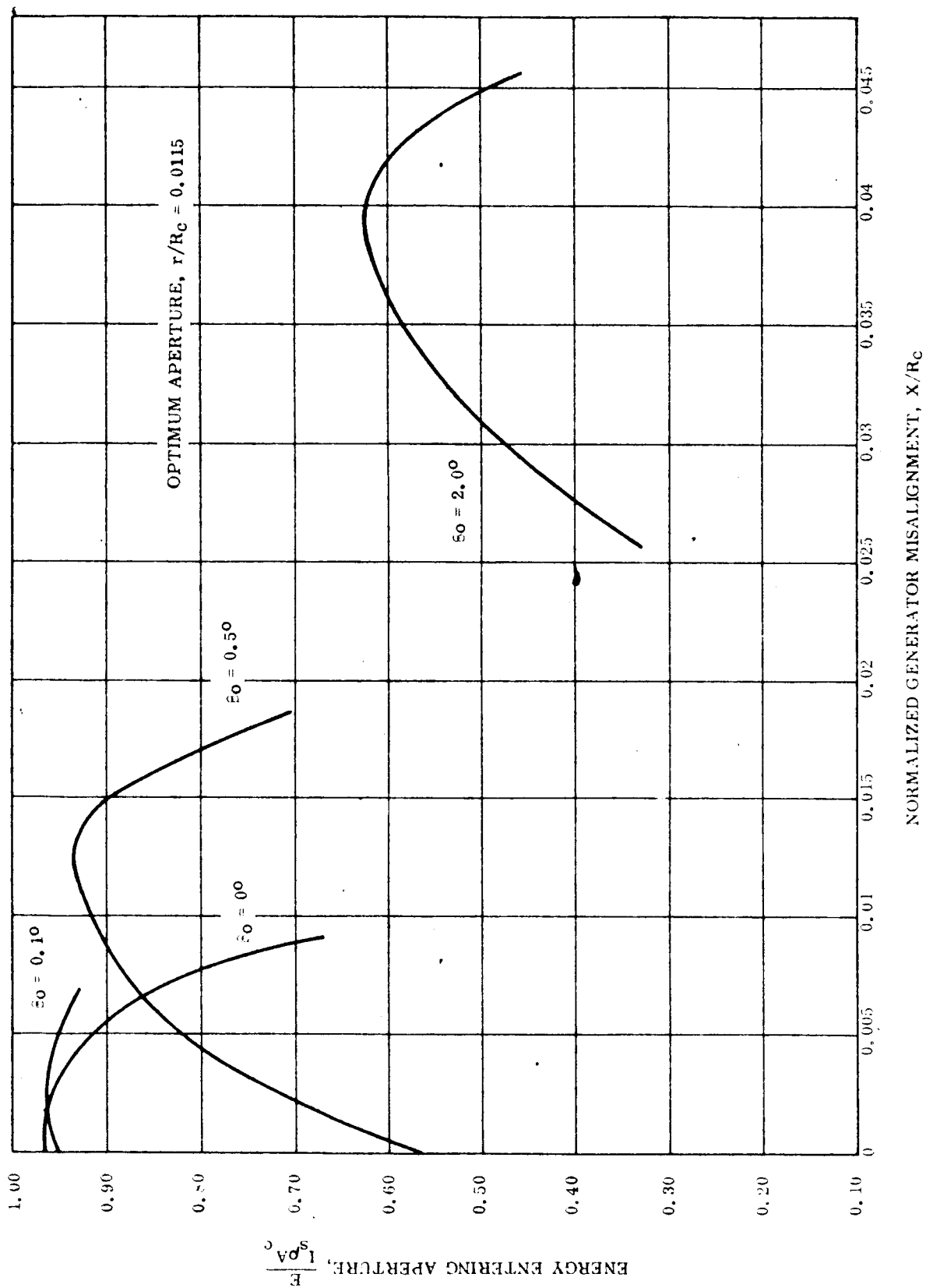Figure P-10. Normalized Energy Entering Aperture vs. Normalized Aperture Radius for Various Misaligned Positions
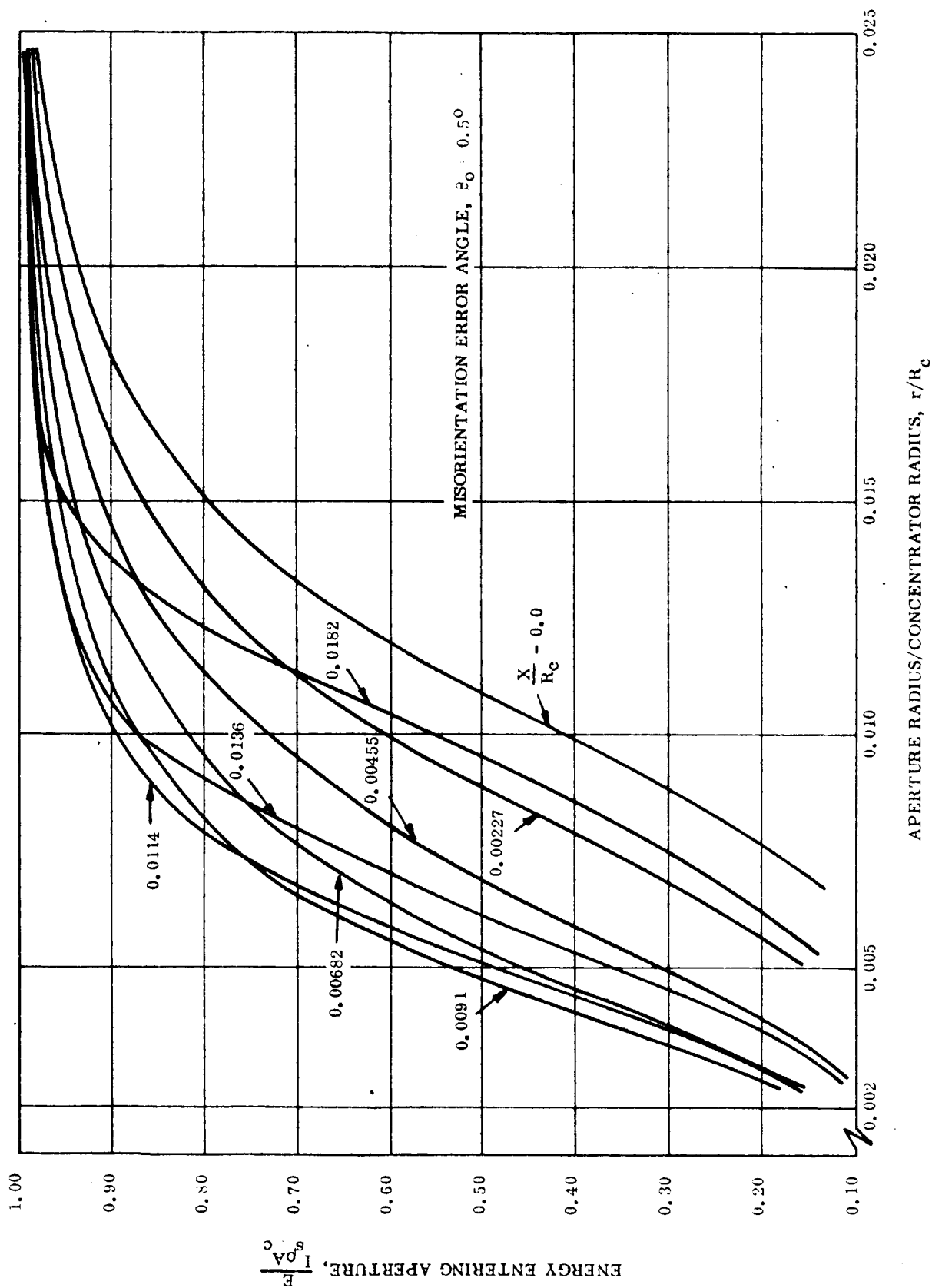
Figure P-11   Normalized Energy Entering Aperture vs. Normalized Aperture Radius for Various Misaligned Positions
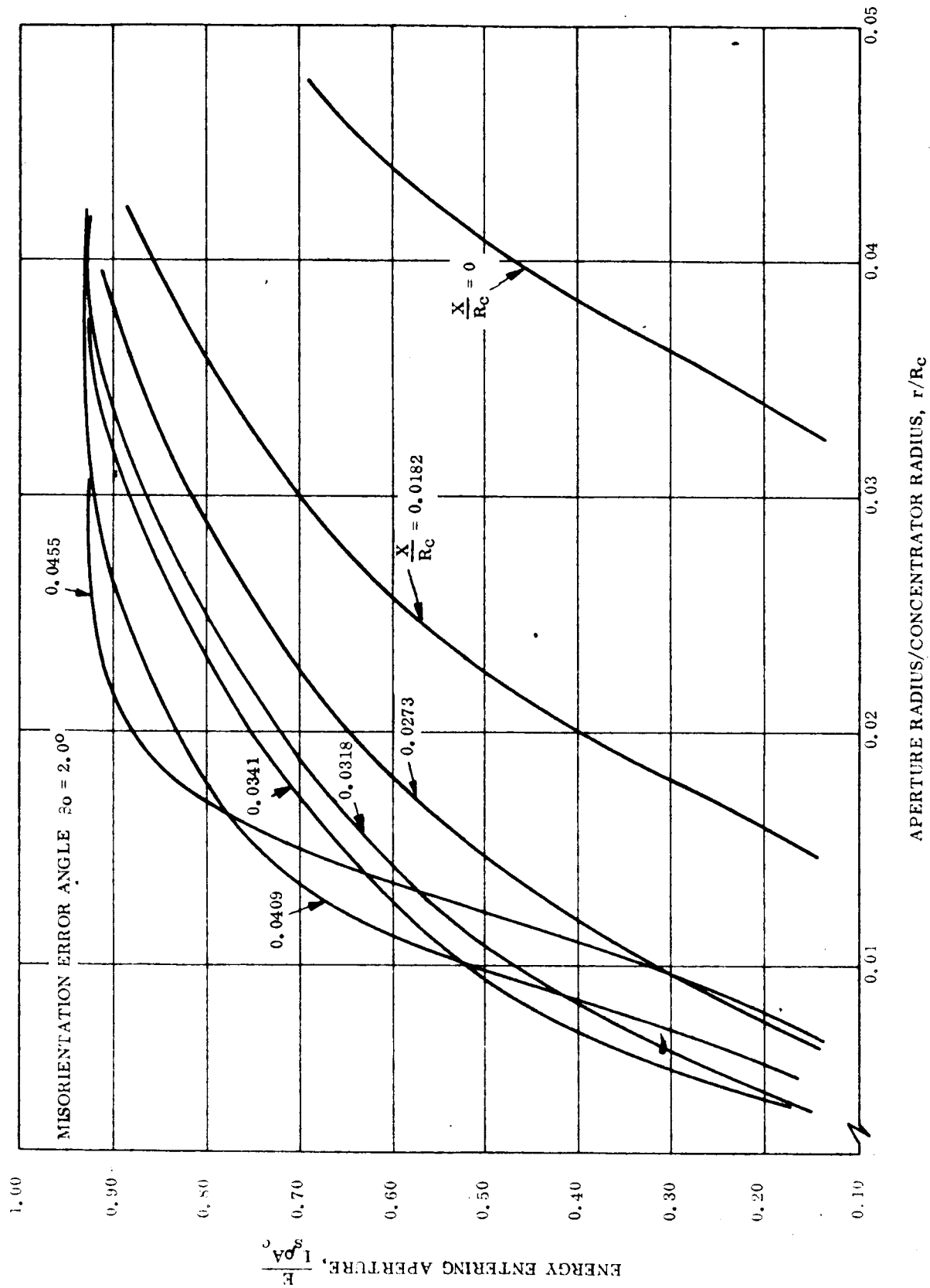
Figure P-12. Normalized Energy Entering Aperture vs. Normalized Aperture Radius for Various Misaligned Positions

OPTIMUM APERTURE, $r/R_C = 0.0115$

$\varepsilon_o = 2.0^\circ$

$\varepsilon_o = 0.5^\circ$

$\varepsilon_o = 0^\circ$

$\varepsilon_o = 0.10^\circ$

NORMALIZED GENERATOR MISALIGNMENT, X/R_C

ENERGY ENTERING APERTURE, $\frac{E}{I_s \rho A_c}$

Figure P-13. Normalized Energy Entering Aperture vs. Misaligned Position for Various Misorientation Errors

b. Case II – The generator may be misaligned so that the aperture is no longer on the optic axis of the concentrator but is displaced in the focal plane by an amount, x. (See Figure P-14).

c. Case III – A combination of Case I and II may exist where both types of error may be present. (See Figure P-14).

The data generated in Section 4.3 are directly applicable to determining the performance of the concentrator-aperture system under the error cases described above. For evaluation of orientation and misalignment errors, only misalignment in the direction of misorientation and on the axis of symmetry of the flux distribution was considered. The limitation is imposed because these conditions correspond to the least severe effects on the system and all other misalignment directions produce more rapid decrease in collected energy with misalignment error.

Figure P-15 shows a plot of energy entering the aperture as a function of boresight misalignment angle, for various aperture sizes, including that aperture which is optimum for a cavity temperature of $2000^{\circ}K$. This corresponds to the boresight performance for Case I described previously.

Figure P-16 shows the variation in energy into the optimum aperture (for $2000^{\circ}K$ cavity temperature) when no boresight misorientation exists but the generator has been misaligned as described in Case II. Since the orientation system does not maintain absolutely zero-degree orientation error plots of energy entering the aperture have been displayed for $\beta_o = 0$ and $\beta_o = 0.1$ degrees. Ideally the energy entering the aperture will be bounded by these two curves.

Case III is a combination of Case I and Case II. The performance of the system under these conditions is adequately described by Figure P-13 and shown again in Figure P-17. Figure P-13 shows the energy entering the optimum generator aperture when both types of error (misoriented boresight and misaligned generator) exist.

P-24
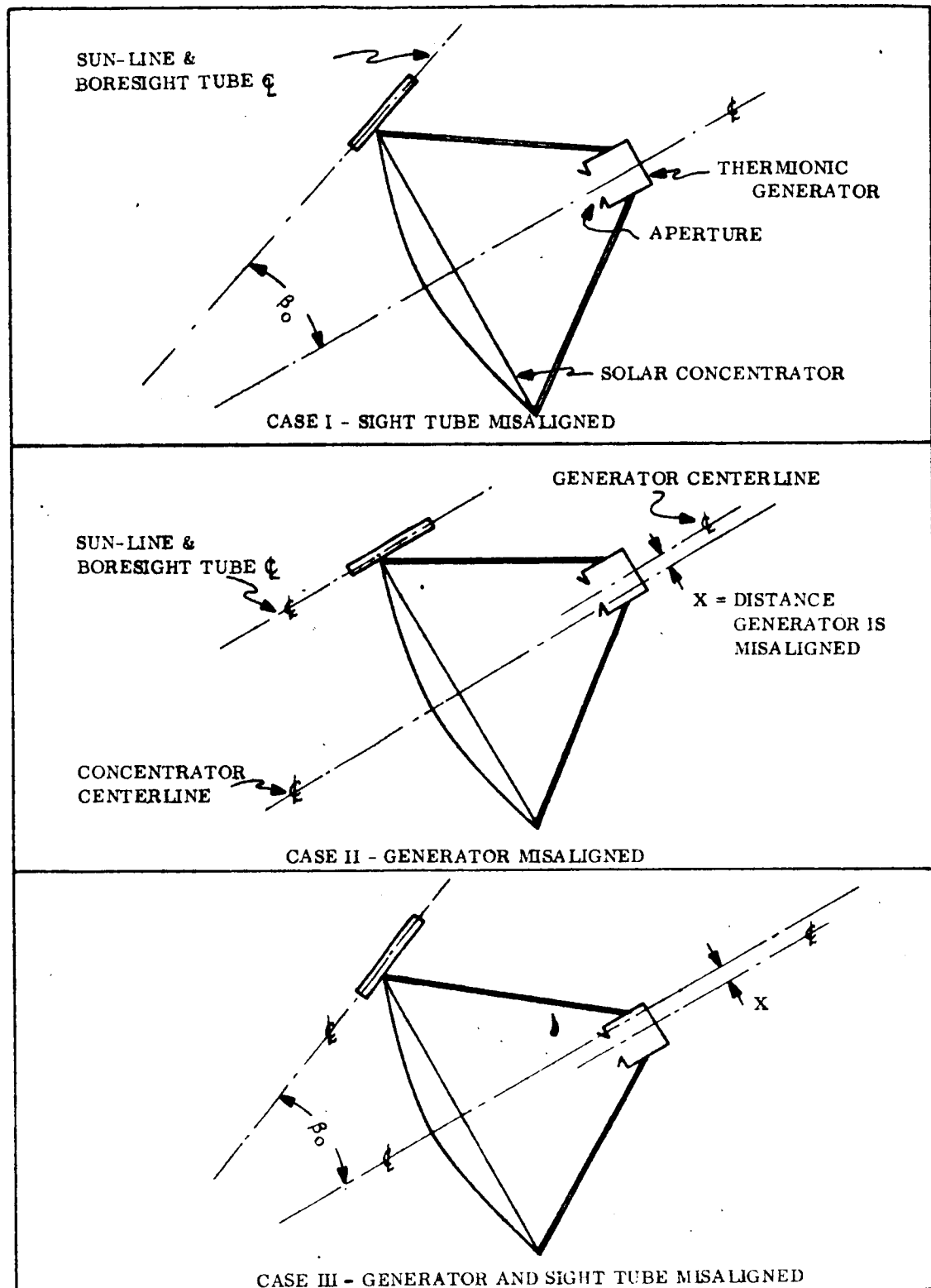
Figure P-14. Definition of Misalignment Case
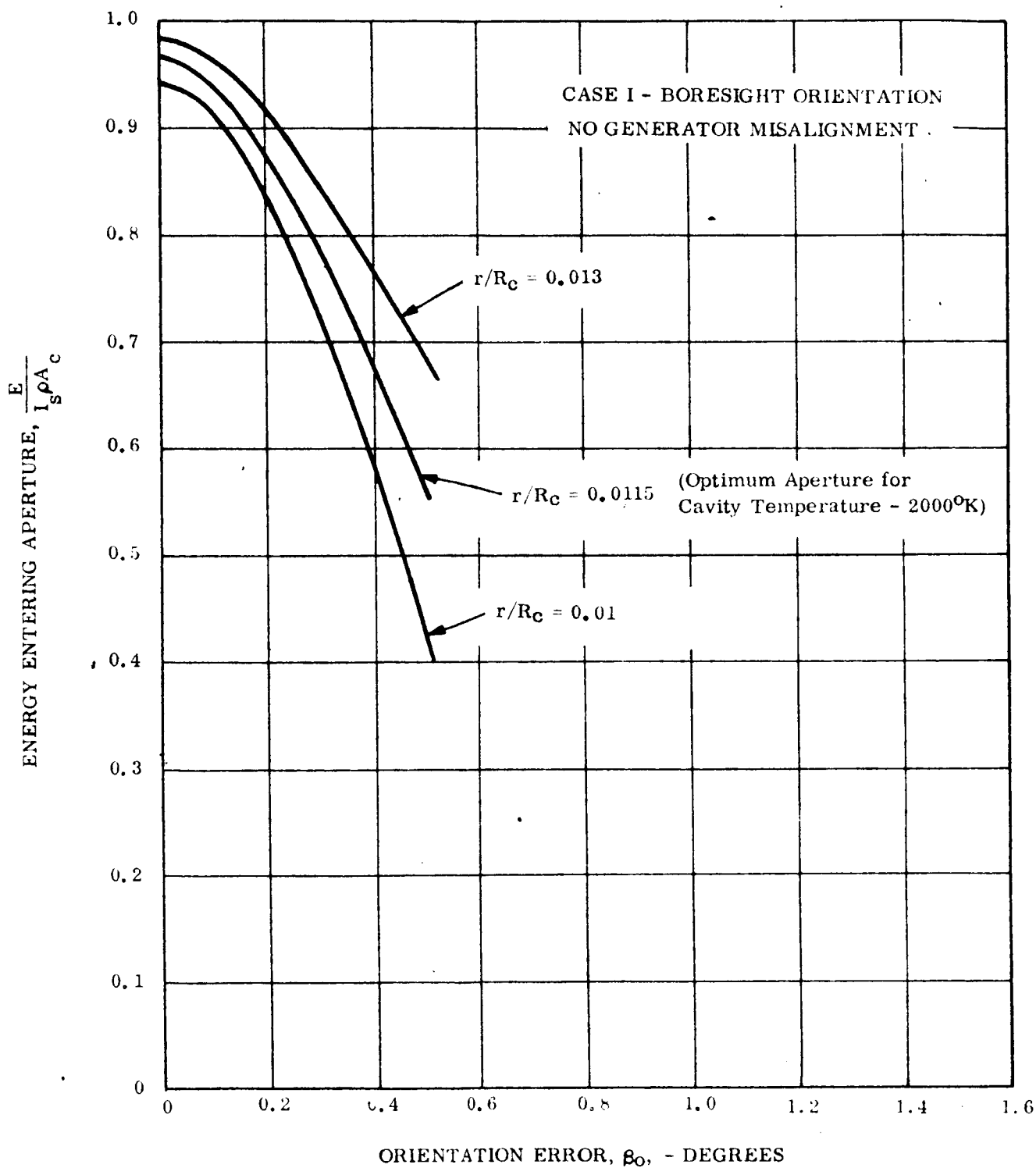
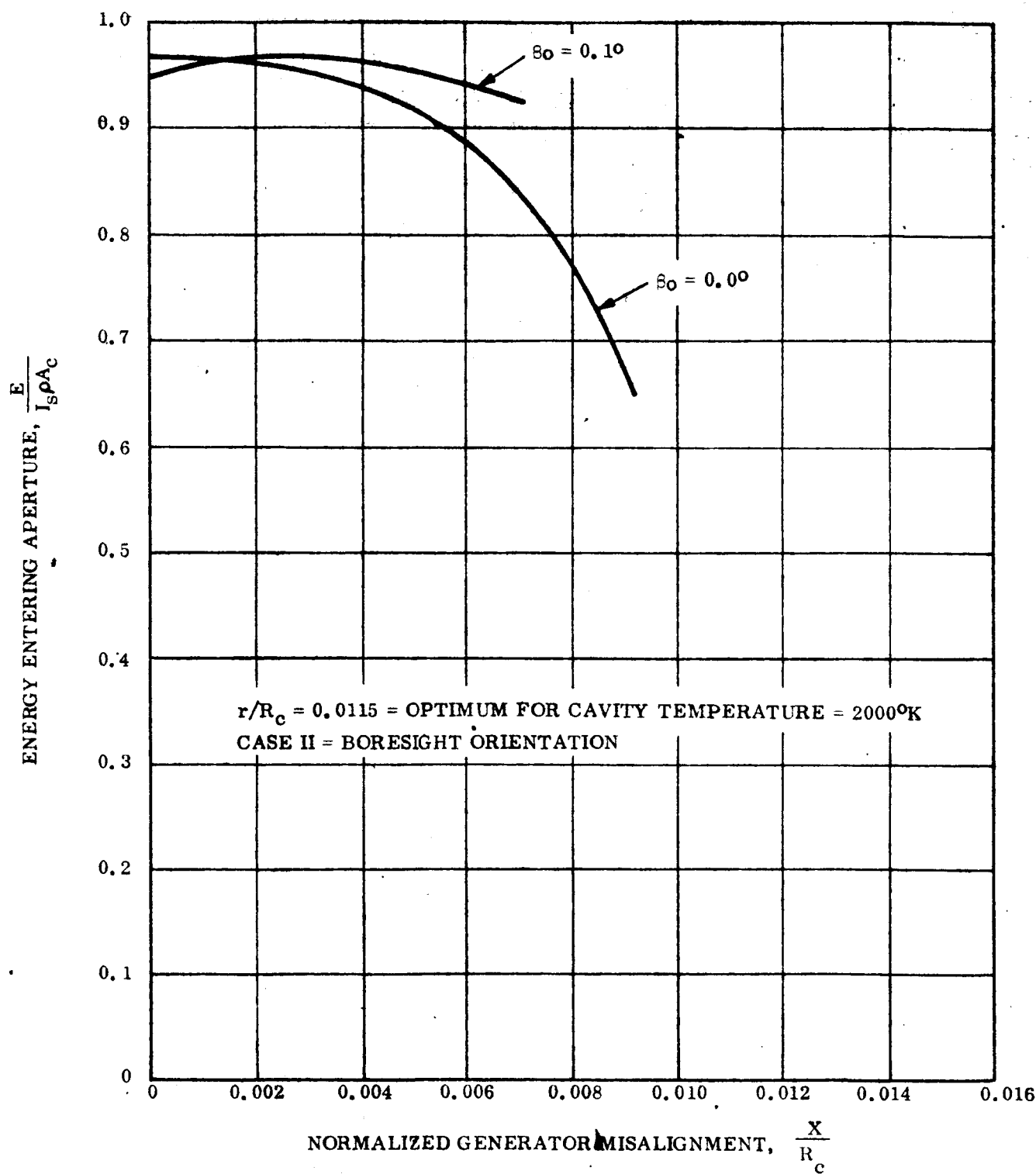Figure P-15. Variation of Energy Entering Aperture vs. Orientation Error for Various Aperture Sizes

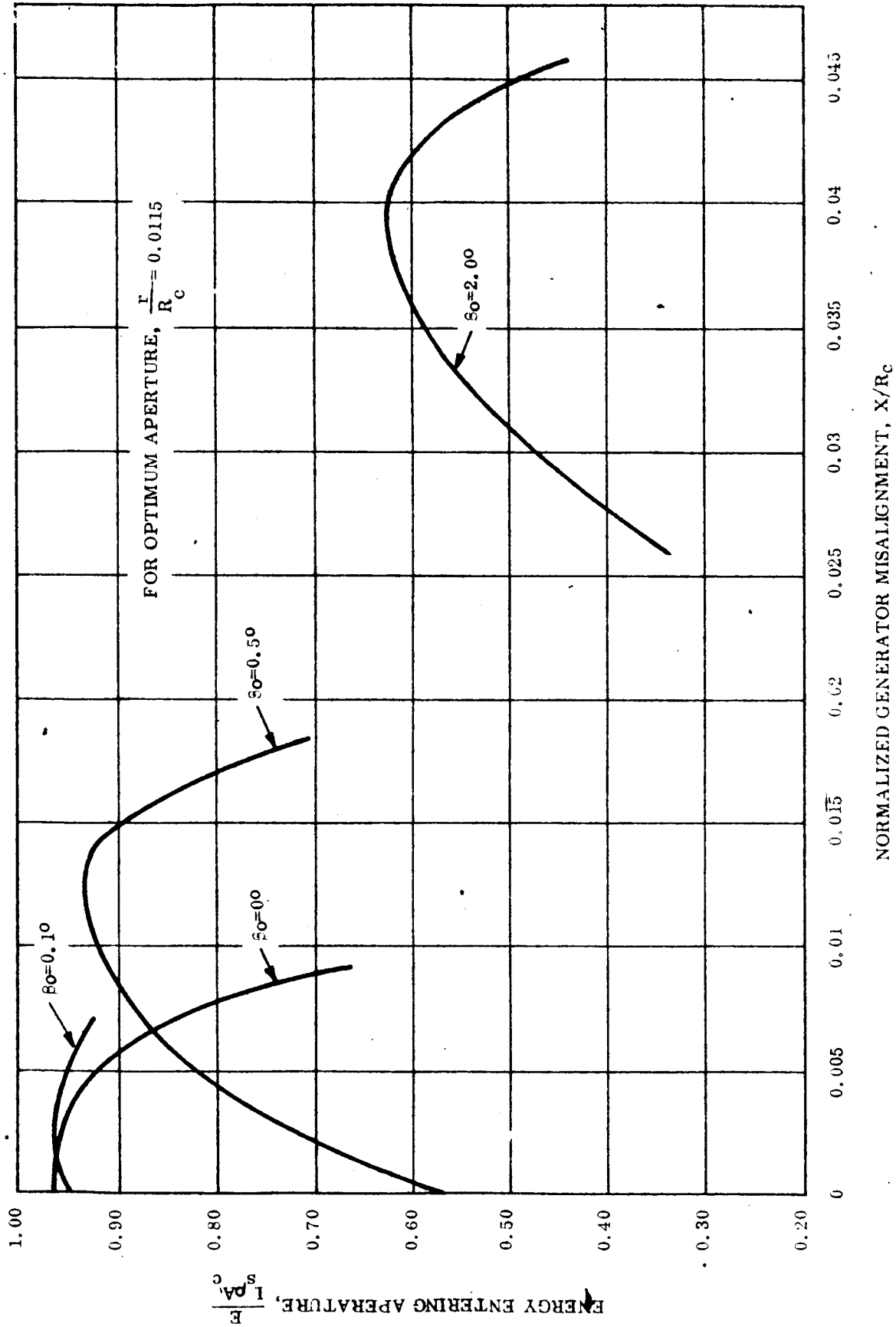Figure P-16. Energy Entering Aperture vs Generator Misalignment

Figure P-17. Normalized Energy Entering Aperture vs. Misaligned Position for Various Misorientation Errors

5.2 FLUX SENSOR

The application of this type of system to orientation of a solar thermionic system is new and has not been explored heretofore. The basic concepts involved and the preliminary reasons for investigating this type of system will be considered here.

5.2.1 Description of Conceptual System

The system under consideration would consist of a group of sensors, mounted concentric with the aperture of the generator. These sensors would sense the incident concentrated flux from the solar concentrator. The signal thus provided would be used to vary the concentrator orientation so that equal flux would fall on diametrically opposite sensors.

5.2.2 Description of Sensor Operation

The concentrated flux in the focal plane exhibits a peak in the distribution (see Figure P-6). This peak shifts as the solar concentrator is misoriented from the sun. The direction of the shift of this peak is in the direction of the misorientation. The property suggests the following possibility.

If a mechanism can be devised such that the concentrated flux in the focal plane can be sensed, then the generator aperture could always be located about the peak of the flux distribution.

This type of mechanism would accomplish the following:

a. When the generator is not misaligned but located exactly on the optic axis of the concentrator, the flux sensing mechanism would tend to orient the concentrator, (within the accuracy limitations of the mechanism) so that the concentrated spot falls in the generator aperture.

b. If the generator became misaligned to the concentrator (through shock, thermal
    distortion, etc.) so that the generator aperture was no longer on the optic axis
    of the concentrator, the mechanism would tend to misorient the concentrator,
    so that the peak in the flux distribution would still fall in the generator aperture.

Such a system would maximize the energy entering the generator aperture and tend to minimize
the effects of misalignments which might occur. The following sections will analyze the
performance of such a system using the solar concentrator model developed in Section 4
of this appendix.

5.2.3 Analysis of Flux Sensor Performance

This section will concern itself with determing how well a mechanism, such as has
been described, can maximize the energy into the generator aperture as the generator is
misaligned.

Figure P-18 illustrates the quantities of concern that are defined below:

R_s = Radius of the circle on which the sensors are mounted

X_a = Misaligned location of the generator aperture with respect
to the optic axis of the concentrator.

The analysis will be performed for the generator aperture which is optimum for a cavity
temperature of 2000°K.

X_{ao} is defined as:

X_{ao} = That misaligned position of the generator for which the misoriented
flux distribution being considered is optimum.
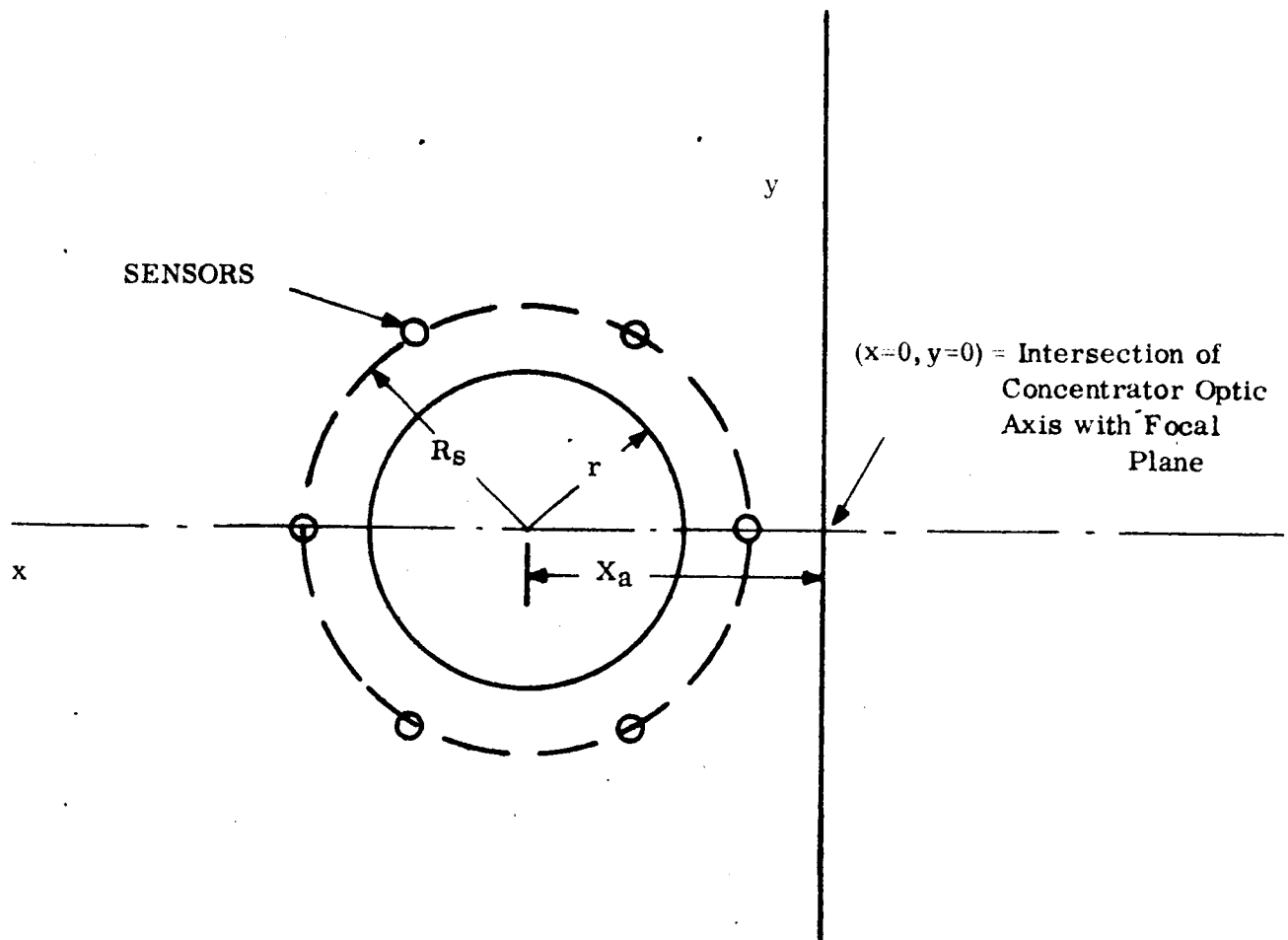
Figure P-18. Definition of Flux Sensor Parameters

The flux distribution in the focal plane is always symmetric about a plane through the optic axis of the concentrator and 90 degrees from the axis of rotation of the solar concentrator. In Figure P-5b, the plane of symmetry is the $0 - \pi$ plane of the x-z plane (where z is an axis perpendicular to the x-y plane). Since the flux is symmetric about this plane, a flux sensing mechanism (such as described previously) would center about this axis and only the flux distribution along the axis of symmetry (x-axis or $0 - \pi$) in the focal plane need be considered to determine where the aperture is located with respect to the skewed distribution. Therefore, the flux distribution in the $0 - \pi$ plane will be considered in the remainder of the analysis. This distribution is shown in Figure P-19.

Figure P-17, determined the variation in energy into the generator aperature as the orientation angle, β_0, and the generator misalignment from the optic axis of the concentrator vary. As can be seen in Figure P-17, for a given misalignment x/R_c, there is a misorientation angle, β_0, which delivers maximum energy to the generator. In terms of the sensing mechanism under consideration, this may be thought of as the orientation angle which is optimum, for a given generator misalignment. In other words, if the generator were misaligned from the optic axis of the concentrator by an amount X_{ao} (corresponding to a peak in Figure P-17) then it would be necessary to misorient the concentrator by the corresponding β_0 in order to get the maximum possible energy into the generator.

Since the flux distribution is skewed in the $0 - \pi$ plane there will exist only one sensor radius, R_s, which will cause the concentrator to misorient by the optimum β_0, for a given generator misalignment. The following quantities in Figure P-18 are defined as:

R_s = Radius of circle on which the sensors are mounted

X_a = That amount of misalignment which causes the concentrator to be misoriented through an angle β_0, for a given sensor radius, R_s
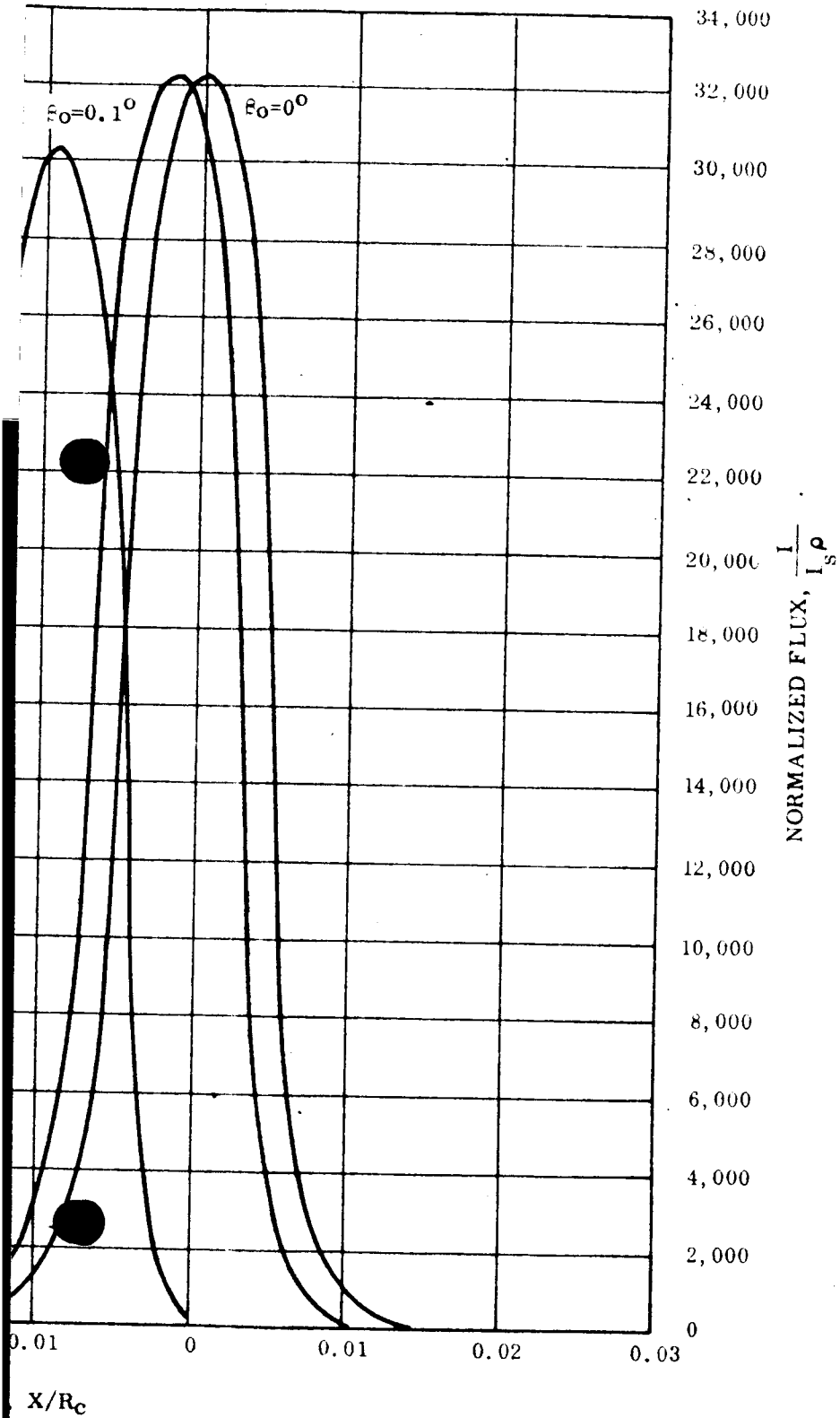
P-32

$\beta_o=0.5^o$

$\beta_o=2.0^o$

0.07   0.06   0.05   0.04   0.03   0.02

GENERATOR MISALIGNMENT
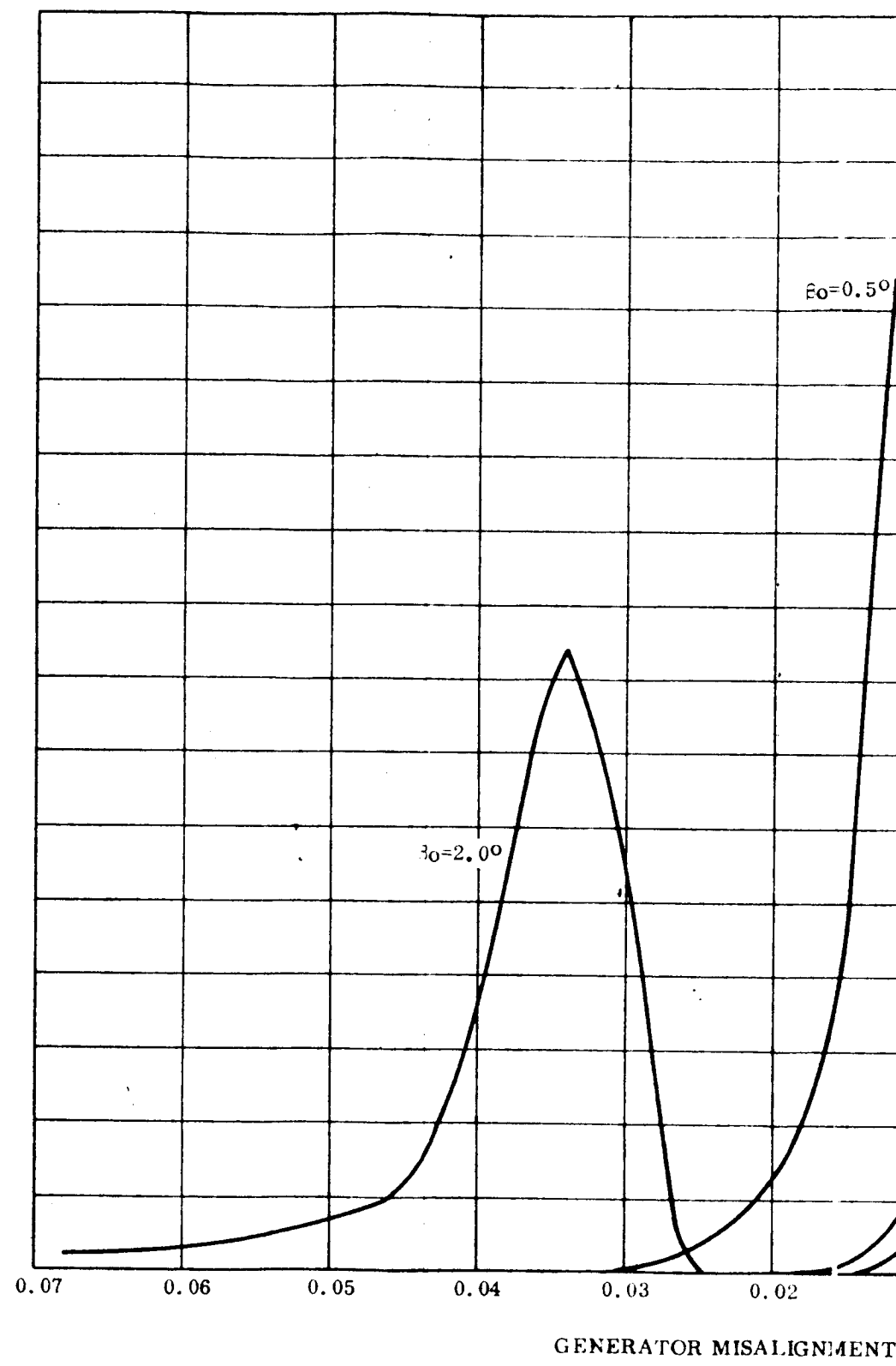
Figure P-19. Flux Distribution in ($0 - \pi$) Plane for Various Misorientation Errors

X_{ao} = That amount of misalignment which causes the concentrator to be misoriented through an angle β_o, which is optimum for that amount of misalignment in Figure P-17

R_{so} = That sensor radius which produces a misorientation of β_o, which is optimum for X_{ao}.

In order to determine if there is a fixed sensor radius R_s^*, which will produce the optimum misorientation of the concentrator for any generator misalignment, the following procedure will be followed. The flux distribution in the $0 - \pi$ plane, is only available at discrete values of misorientation angle, β_o. Therefore, it will be necessary to determine that sensor radius, R_{so}, which would center at X_{ao} when a particular misoriented distribution is considered. This may be clarified by considering Figure P-17 and P-20. For the purpose of this example, the β_o = 2.0-degree curve of Figure P-19 will be used.

In Figure P-17, it is apparent that if a generator misalignment of x/R_c = 0.0395 is present, the concentrator would have to be misoriented by β_o = 2.0-degrees. For any other misalignment at a misorientation of β_o = 2.0-degrees, less energy enters the aperture. Referring to Figure P-20, it can be seen that as the sensor radius, R_s, varies, there is only one value of R_s which causes a misorientation of β_o = 2.0-degrees when X_a/R_c = 0.0395. This value of R_s/R_c is 0.0134. Therefore, for β_o = 2.0-degrees we have

$$\left. \begin{array}{l} \dfrac{X_{ao}}{R_c} = 0.0395 \\[2em] R_{so}/R_c = 0.0134 \end{array} \right\} \quad \beta_o = 2.0^{\circ}.$$

This type of analysis can be performed for the other available distributions, β_o = 0.1, 0.5 degrees, etc. Figure P-21 shows that misalignment X_a/R_c which will produce a given misorientation β_o as a function of sensor circle radius, R_s/R_c. The desired curve X_{ao}/R_c is also plotted. As can be seen in Figure P-21 a value of R_s/R_c = 0.0136 very closely produces the optimum misorientation angle desired, (the curve for R_s/R_c = 0.0136 closely approximates the X_{ao}/R_c curve). Figure P-22 was plotted in order to determine the value
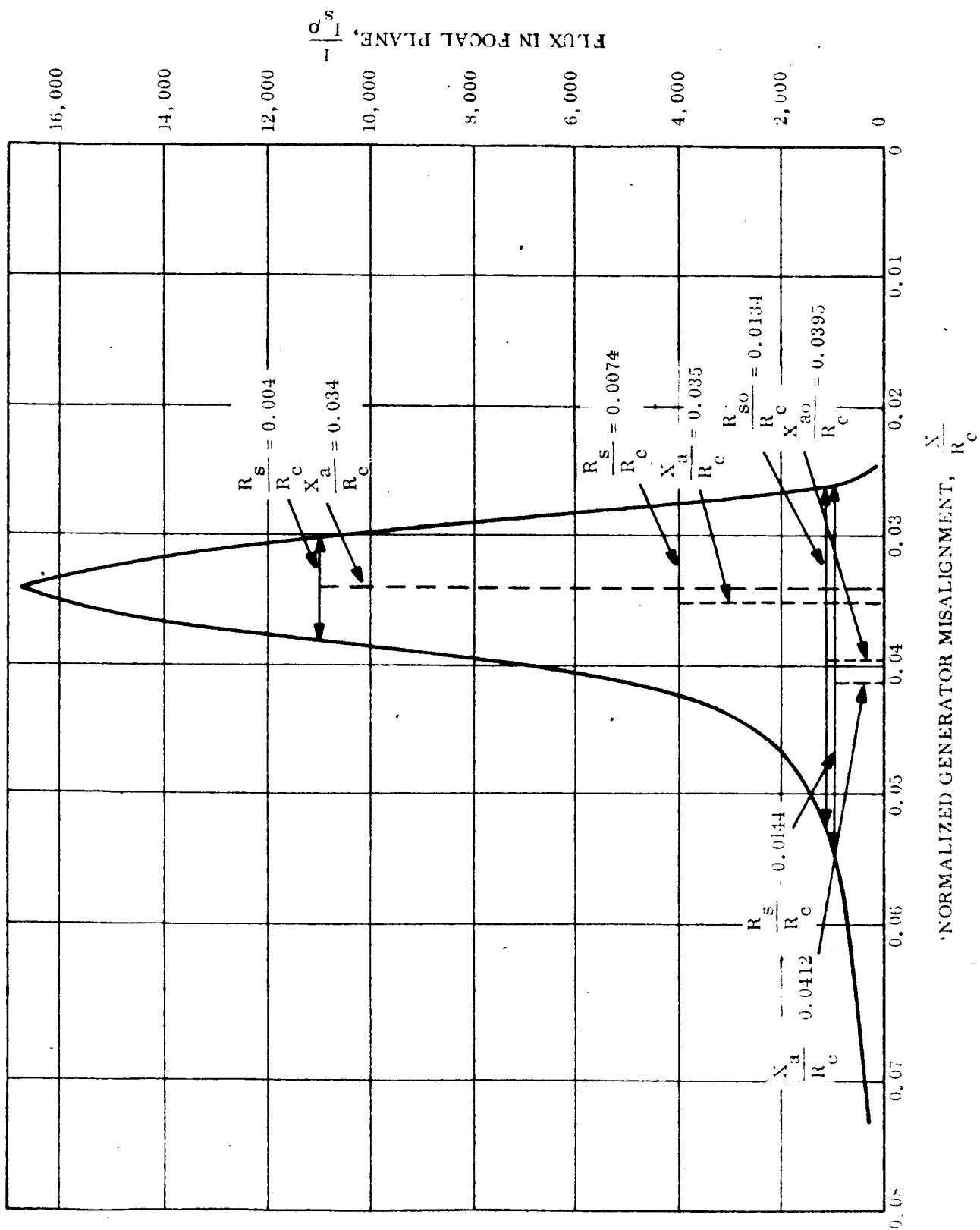
Figure P-20. Influence of Sensor Circle Radius

of R_{so}/R_c corresponding to each misorientation angle and misalignment X_{ao}/R_c. This is a plot of X_a/R_c versus R_s/R_c at constant values of misorientation. The value of X_{ao}/R_c which is optimum for each misorientation angle is also plotted. The intersection of this line with each constant β_o line is the value of R_s/R_c which is optimum for that misalignment and misorientation angle. This quantity is R_{so}/R_c which has previously been defined. The dotted line in Figure P-22 shows the variation in R_{so}/R_c with misorientation angle, β_o. For misorientations between 0.1 and 1.0 degrees, R_{so}/R_c is fairly constant, varying between

$$R_{so}/R_c \Big|_{\beta_o = 0.5^o} = 0.0125$$

$$R_{so}/R_c \Big|_{\beta_o = 0.1^o} = 0.0128.$$

Since the energy entering the generator drops off below 90 percent of the energy leaving the concentrator, for misorientation angles greater than $\beta_o = 1.0$ degrees, it is reasonable to select a value of R_s/R_c which nearly approximates the optimum value at small misorientations. Therefore, for the type of concentrators being considered, a fixed sensor radius R_s^* could be selected such that

$$R_s^*/R_c \simeq 0.0126.$$

This would produce very nearly optimum misorientation for any misalignment, up to a misorientation angle of $\beta_o = 1.0$ degrees.

5.2.4 Results

Having chosen a fixed sensor radius of $R_s^*/R_c = 0.0126$, it is possible to define the operation of the flux sensing system, as generator misalignment varies. This is shown in Figure P-23. The equivalent concentrator misorientation is designated by the hash marks on the curve. Figure P-24 shows a plot of concentrator misorientation as a function
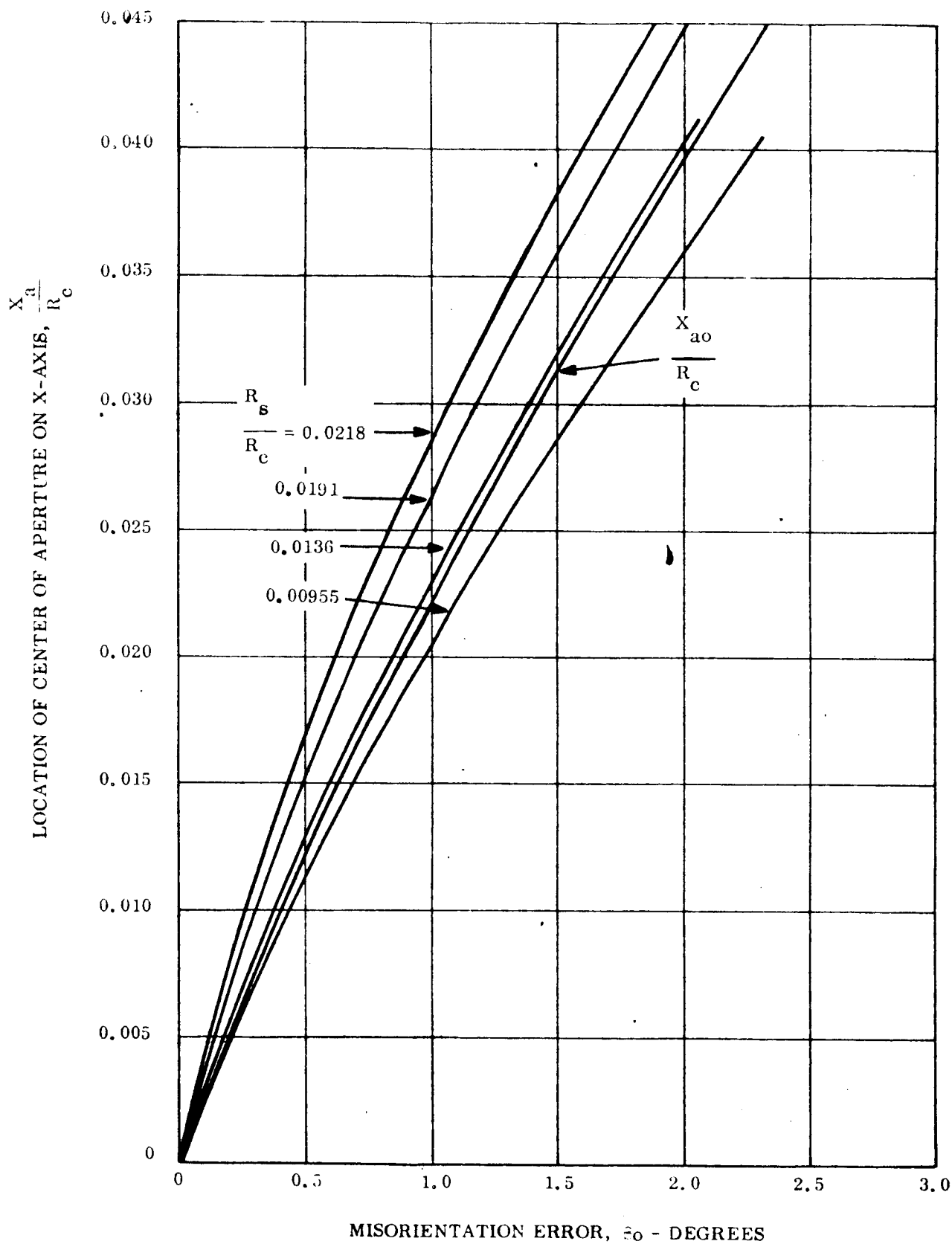
Figure P-21. Location of Aperture Center as a Function of
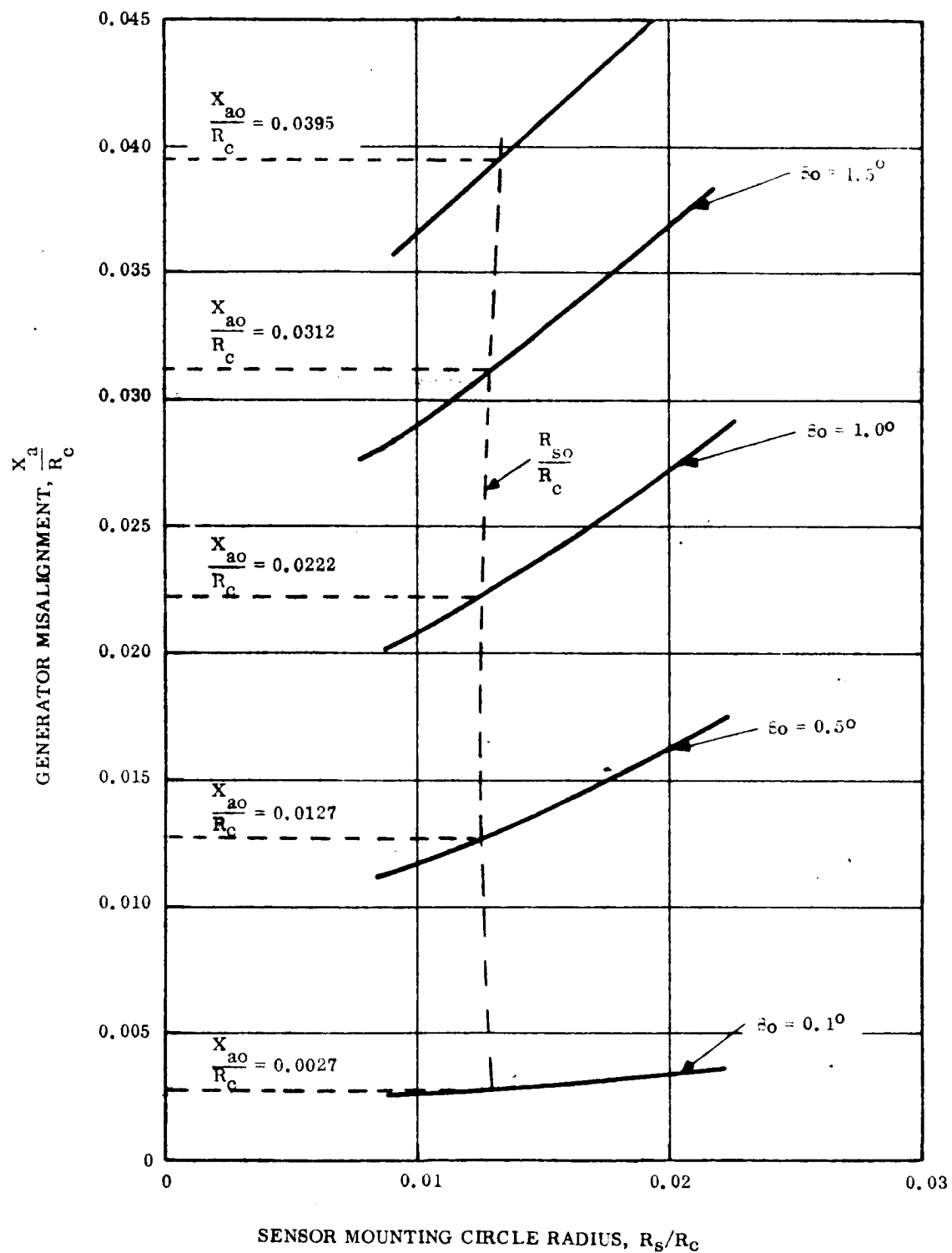Sensor Circle Radius and Equivalent Misorientation

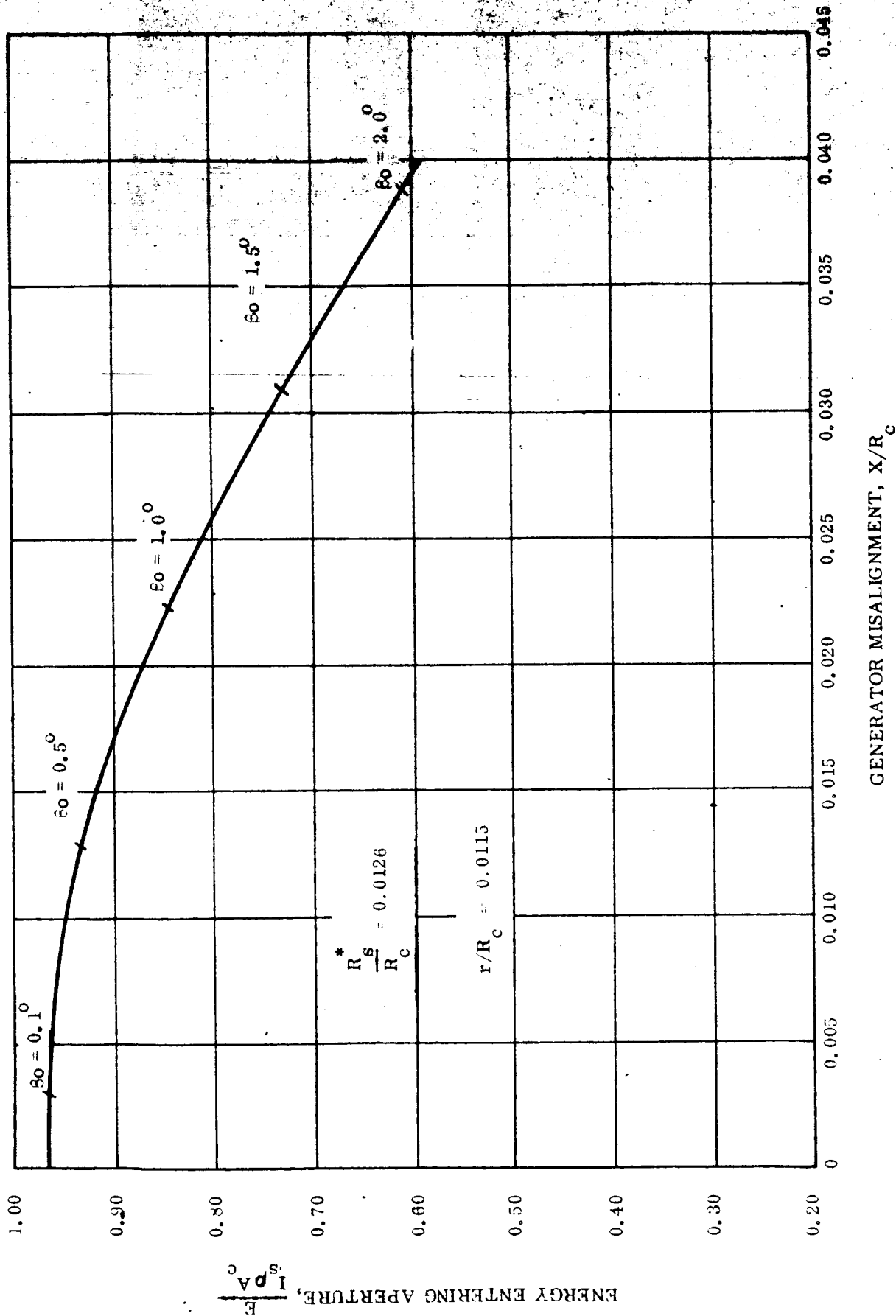Figure P-22. Determination of Optimum Sensor Mounting Circle Radius

GENERATOR MISALIGNMENT, X/R_c

$$\frac{R_s^*}{R_c} = 0.0126$$

$$r/R_c = 0.0115$$

ENERGY ENTERING APERTURE, $\frac{E}{I_{,s} \rho A_c}$

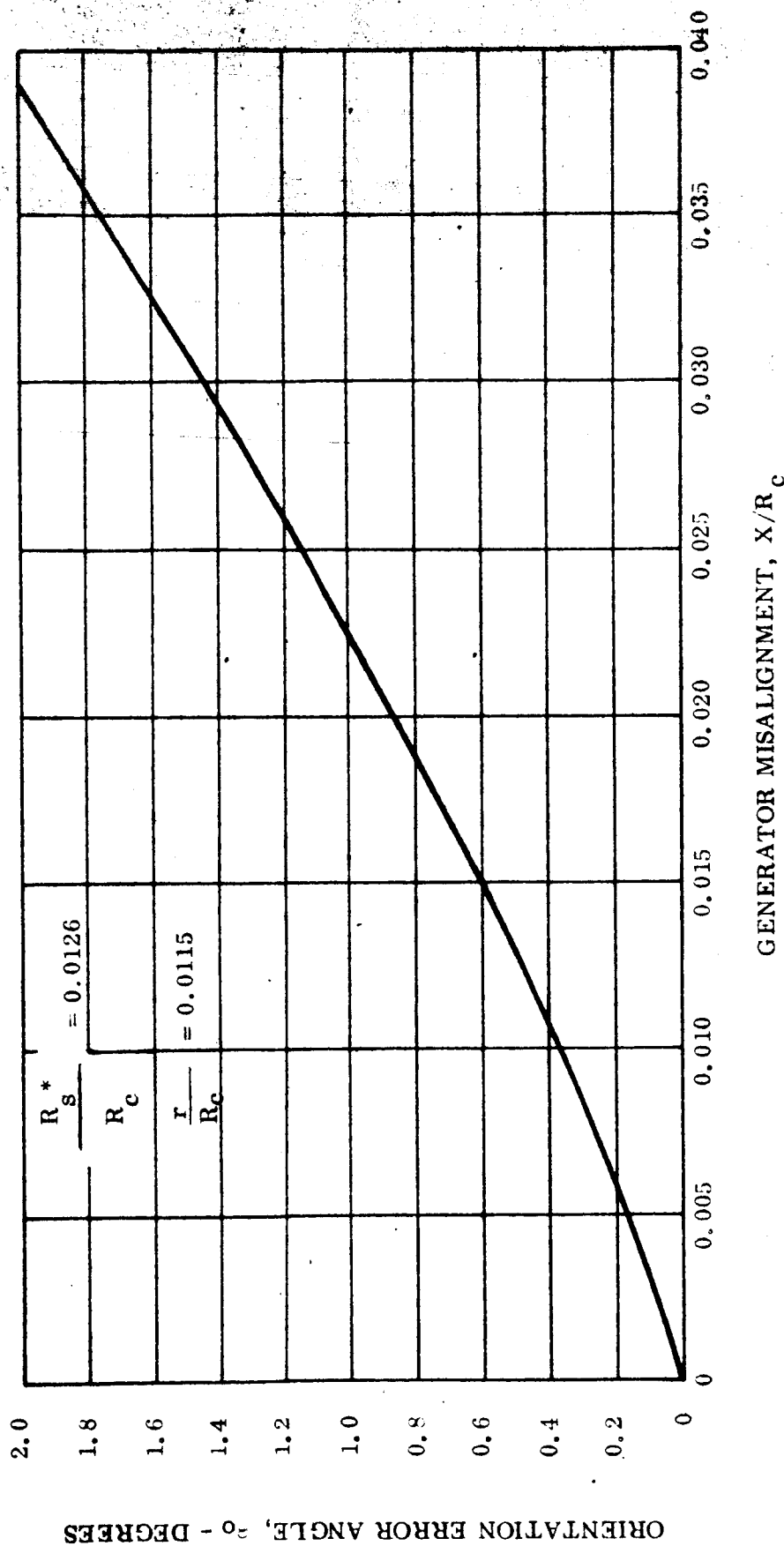Figure P-23. Flux Sensing System Performance With Generator Misalignment

179

Figure P-24. Concentrator Misorientation vs. Generator Misalignment for Flux Sensors

of generator misalignment for a thermionic system equipped with a flux sensing orientation system that has a sensor circle radius of $R_s{}^*/R_c = 0.0126$ and a generator aperture of $r/R_c = 0.0115$.

6. REFERENCES

P-1   G. L. Schrenk, D. G. Gritton, "Analysis of Solar Reflectors",
        EDR 3693, A F04(695)-335 Final Report, December, 1963.

P-2   T. F. Green, "Integration of Light Intensity", Internal General
        Electric Spacecraft Department, Report number PIR 4424-005,
        October 29, 1964.

P-3   J. Royer, "Input Requirements for the Integration of Light Intensity
        Program (IOLI)", Internal General Electric Spacecraft Department
        Report number PIR 1126-162, December 1, 1964.